2008

Experimental investigations on micro-scale thermal fluid phenomena by using advance flow diagnostic techniques

Zheyan Jin
Iowa State University

Experimental investigations on micro-scale thermal fluid phenomena by using advance flow diagnostic techniques

by

Zheyan Jin

A dissertation submitted to the graduate faculty

in partial fulfillment of the requirements for the degree of

DOCTOR OF PHILOSOPHY

Major: Aerospace Engineering

Program of Study Committee:
Hui Hu, Major Professor
Michael G. Olsen
R. Ganesh Rajagopalan
Partha P. Sarkar
Zhijian Wang

Iowa State University

Ames, Iowa

2008

DEDICATION

To my parents for their love and support throughout my life

TABLE OF CONTENTS

LIST OF TABLES

LIST OF FIGURES

CHAPTER 1: INTRODUCTION

1.1. Mixing Enhancement in Y-shaped Microchannels

Microfluidics is one of the most rapidly growing fields in micro-electro-mechanical systems technology due to its applications in medical science, biology, and analytical chemistry [1-4]. Microchannels or capillaries are basic components of all microfluidic devices, and they have the potential of reducing the fabrication costs and consumption of chemicals as well as shortening the time of biochemical analysis. Over the last ten years, capillaries have been mainly used for capillary electrophoretic (CE) methods due to the high separation efficiencies and peak resolution. Microchannels have recently attracted the researchers' attention because they are less expensive, simpler and faster to fabricate complicated networks for "lab-on-a-chip" devices than capillaries.

Two-fluid mixing is an essential process for many microfluidic or "lab-on-a-chip" devices. Various biomedicial and biochemical processes, such as DNA purification, polymerase chain reaction (PCR), enzyme reaction, and protein folding, involve the mixing of two fluids. The performance of such processes depends heavily on the mixing effectiveness and rapidness of the samples and reagents. However, effective mixing of two fluids inside microchannels could be very challenging since turbulence is usually absent due to the nature of low Reynolds numbers of the microflows. Therefore, studies aimed to develop novel techniques and methodologies to enhance diffusion-dominated fluid mixing processes and to increase the interfacial contact surface area between adjacent streams inside microchannels are very

important and necessary to improve the performance of microfluidic or “lab-on-a-chip” devices.

In recent years, extensive studies have been conducted to develop novel techniques and methodologies to enhance fluid mixing inside microchannels. Several innovative concepts of “micro-mixers” have been proposed through those studies. In general, the proposed “micro-mixers” can be categorized into two groups: passive mixers and active mixers [5]. Passive mixers do not require external energy; the enhanced mixing process relies entirely on the augmentation of diffusion or chaotic advection through special geometrical design of microchannels. In contrast, active mixers usually rely on adding external energy to introduce disturbances to enhance fluid mixing; generating external disturbances in terms of temperature [6], pressure [7,8], electrohydrodynamics [9], dielectrophoretics [10], acoustics [11] as well as magnetohydrodynamics [12], several kinds of active micro-mixers have already been proposed to effectively enhance fluid mixing in microchannels. In this thesis, a parametric study was conducted to quantify the effectiveness of achieving fluid mixing control/enhancement inside Y-shaped microchannels using an active control method, electrokinetic instability (EKI).

EKI occurs when two streams with different electric conductivities meet in a microchannel under an applied static electric field as shown schematically in Fig. 1.1. If the strength of the applied static electric field exceeds a certain threshold value, the flow instability of adjacent streams could be observed in a sinuous form along the interface of the mixing streams [13, 14]. The conductivity gradient subject to an external electric field has been suggested as a

source of electrical charges and the Coulombic force acts to generate additional body force [15]. Relevant to the mechanism of electrokinetic instability, Hoberg & Melcher [15] showed that the interface of miscible fluids with conductivity gradient becomes unstable under a normal electric field in an unbounded domain. Baygents & Baldessari [16] suggested that the flow generated in isoelectric focusing devices is a consequence of the free charges generated by the electric field applied normally to the conductivity gradient.

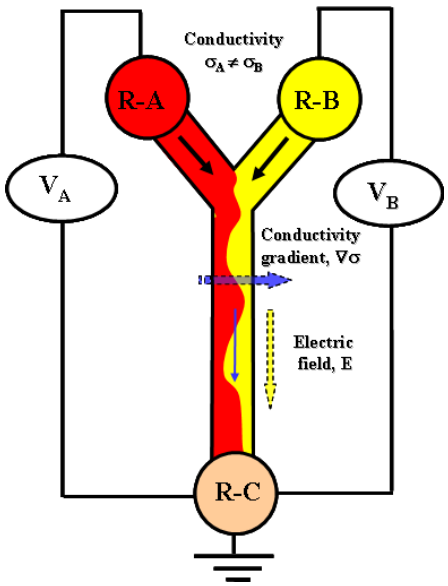

Figure 1.1. The schematic of the EKI

Oddy et al. [17] is the first to use EKI to manipulate fluid mixing process in a microchannel. Chen et al. [14] conducted a pioneer study to elucidate the underlying fundamental physics of EKI and associated flow phenomena in a T-shaped microchannel. They reported that EKI can be observed as convective waves propagating downstream as the strength of the applied static electric field exceeds a threshold value (i.e, the critic strength of the applied electric field called in the present study), which corresponds to the convectively unstable mode of the EKI. When the strength of the applied electric field becomes relatively high, upstream

propagating waves were observed, indicating the mode of absolute instability. Chen et al. [14] also suggested a physical model to capture the coupling between electric and flow fields. More recently, Posner & Santigao [18] studied the behavior of EKI waves in a cross-shaped microchannel under a wide range of the applied static electric fields and conductivity ratios of the center-to-sheath streams. They found that the required critical strength of the applied static electric field depends on both the centre-to-sheath conductivity ratio and the ratio of the static voltages applied to different branches of the cross-shaped microchannel. Shin et al. [19] demonstrated for the first time that adding an alternative perturbation to the applied static electric field could manipulate EKI waves to either enhance or suppress the fluid mixing process in a cross-shaped microchannel depending on the frequency of the alternative perturbation.

Park et al. [20] studied four microchannels which were straight channel, channel with square cavities on one sides, channel with square cavities on both sides and channel with herringbone shape cavities on both sides. They compared the mixing efficiency of these four channels under different static electric fields. Their results show that the mixing efficiency is increase by about 15% for the channel with herringbone-shape cavities as compared with the straight channel. Huang et al. [21] proposed a cross-shaped micromixer featuring a pair barrier within the mixing channel which resulted in higher mixing efficiency than the one without barrier. In addition, Tai et al. [22] studied the mixing enhancement of the T-shaped microchannel with 45º parallelogram barriers (PBs) inside. They found that the microchannel with the PBs of a higher value has better mixing performance.

So far, only Posner & Santigao [18] conducted a parameter study to quantify the critical strength of the applied static electric field as a function of the conductivity ratio of the mixing streams in a cross-shaped microchannel. With consideration of the wide spread applications of two-stream mixing in Y-shaped microchannels, the effects of the differences in the mixing flow arrangement (two-stream mixing vs. three-stream mixing, Y-shaped micro-mixers vs. cross-shaped micro-mixers) on the critic strength of the applied static electric field and the resultant fluid mixing process were explored in chapter 4 of this thesis. The effects of the conductivity ratio of the two mixing streams, the strength of the applied static electric fields, and the frequency and amplitude of the applied alternating perturbations, on the evolution of the EKI waves and resultant fluid mixing process were investigated systematically.

Although Shin et al. [19] demonstrated that adding an alternative perturbation to the applied static electric field could manipulate EKI waves to either enhance or suppress the fluid mixing process in a cross-shaped microchannel depending on the frequency of the alternative perturbation, their conclusions were limited to that particular type of microchannel. In addition, although previous studies [20-22] investigated the effect of geometry of T-shaped or cross-shaped microchannels on the mixing enhancement by using EKI, the EKI waves were generated by using static electric fields only. To the author' best knowledge, no one has ever combined alternative electric and static electric fields to generate EKI waves in different Y-shaped microchannels. Considering that the mixing process could be enhanced by adding alternative perturbations which was concluded during this study, it would be necessary to investigate the effect of geometry of microchannels on the mixing enhancement by adding alternative perturbations. In chapter 5 of this thesis, the effect of geometry of microchannels

on the mixing enhancement was investigated on three microchannels which are termed as channel with cavities, channel with steps, and straight channel. The mixing efficiencies in different depths of the channel with steps were also measured.

1.2. Velocity and Temperature Measurement within Surface Droplets

The second component of present study is to investigate the unsteady flow and heat transfer phenomena inside small surface droplets over a solid substrate at different temperature levels. Droplets have many interesting applications associated with microfluidic problems, e.g., DNA molecule imaging [23, 24], micro-pumps, and ink-jet printing. The details of droplet related phenomena in micro- and nanoscales such as evaporation process, Marangoni effects, contact angles with solid substrates, and electrowetting are not well known. There is a consensus of opinion that the fluid flow inside a droplet may play an important role in the overall transport phenomena. Some of the interesting issues concerning the fluid flow inside a droplet are described below.

Uno *et al* [25] investigated the adsorption characteristics of colloidal suspensions during the evaporation of a droplet on hydrophobic and hydrophilic surfaces. As they pointed out, the particle accumulation phenomena will be closely related to the flow pattern inside a droplet. Together with this, the mechanism of DNA stretching in an evaporating droplet [23, 24] is not completely known.

Another concern is about the contact angle of evaporating sessile droplets placed on a solid substrate. According to Erbil *et al* [26, 27], the behavior of an evaporating sessile droplet is

significantly dependent on the initial contact angle. That is, if the initial contact angle is smaller than 90°, the contact area is almost constant during the overall evaporation stage. On the other hand, if the initial contact angle is greater than 90°, the contact area shrinks, while the contact angle remains almost invariant. As suggested by Rowan *et al* [28] and McHale *et al* [29], this intriguing phenomenon can be closely related to the Marangoni force and Marangoni convection (generated by surface-tension gradient) near the three-phase contact line of air, liquid, and solid.

One effective method for characterizing the electrochemical characteristics of redox active solid is to deposit a small droplet and then obtain the voltammetric curve from measuring the ionic transport. It is reported that convective motion exists inside droplets, which may be generated by the Marangoni effect, the EHD effect, or the evaporation of species [30]. The redox process at the interface is significantly dependent on the convective transport of ionic species [31]. For an accurate assessment of the electrochemical characteristics of surfaces, the flow characteristics and the correlation with the ionic transport should be revealed.

Considering its importance to fluid flows, only a few systematic investigations have been performed in the past towards the understanding of overall transport phenomena inside a droplet. Among the few who have investigated the flow structure inside droplets, Chung and Trinh [32] visualized the flow behavior inside an ultrasonic–electrostatic hybrid levitation system. Zhang and Yang [33] visualized the unstable flow due to Marangoni instability of an evaporating droplet of fluid mixture. Savino and Monti [34] investigated the flow inside sessile and pendant droplets numerically. Kang et al [35, 36] developed a velocity correction

method on the basis of the ray tracing method to overcome image distortion due to the refraction of light at the droplet surface and conducted the velocity measurement inside a droplet by using Particle Image Velocimetry (PIV) technique.

Although Kang et al [35, 36] studied the effect of different concentration of ethanol on the evaporation process of surface droplets, the temperatures of droplets and solid plate were kept at room temperature. Considering that the heat transfer process from a cooling test plate might change the flow fields inside droplets, the effect of plate temperature on velocity distribution inside surface droplets was investigated in chapter 6 of this thesis. In addition, related parameters, such as contact angle and normalized droplet volume were also investigated.

In chapter 7 of this thesis, Molecular Tagging Thermometry (MTT) technology was used to study the transient temperature distribution inside surface droplets during the cooling process. The temperature inside a surface droplet was first measured when the temperatures of test plate and droplet were the same as the room temperature. Then, after the surface temperature of the test plate was cooled down to 2.0 °C, a small water droplet with initial temperature of 20.5°C was placed on the test plate and the transient temperature distributions inside the surface droplet were measured. Due to the relatively high temperature sensitivity of the present lifetime-based MTT technique, the small temperature difference within the small water droplet can be revealed clearly from the measured instantaneous temperature distributions.

CHAPTER 2: ELECTROOSMOTIC FLOW AND MARANGONI FLOW

During the present study on the mixing enhancement in different Y-shaped microchannels and on the velocity measurement inside surface droplets, two kinds of flows were formed which were electroosmotic flow (EOF) and Marangoni flow. EOF is the motion of liquid induced by an applied potential across a capillary tube or microchannel and it is an essential component in chemical separation techniques, notably capillary electrophoresis. Marangoni flow is induced by Marangoni effect which is the mass transfer on, or in, a liquid layer due to surface tension differences. In this chapter, detailed knowledge about these two kinds of flows is presented.

2.1. Electroosmotic Flow (EOF)

The electrokinetic phenomena in porous medium are based on the relative motion between a charged surface and the bulk solution at its interface. The formation of electric double layer at the charged surface of microchannel explains these electrokinetic phenomena of interest: electrophoresis and electrroosmosis. Electrophoresis is the movement of a charged surface plus attached material relative to stationary liquid by an applied electric field. On the other hand, electroosmosis is the movement of liquid relative to a stationary charged surface by an applied electric field. The pressure necessary to counterbalance electroosmotic flow is termed the electroosmotic pressure [37].

Generally, most substances will acquire a surface electric charge when brought into contact with an aqueous medium. Some of the charging mechanisms include ionization, ion

absorption, and ion dissolution. We can find it whenever we apply a voltage to a liquid system that is in close contact with a charged surface. The magnitude and the direction of the resulting electroosmotic flow depend on the composition of the microchannel and the nature of the solution within the microchannel. Empirically, it is found that the phase with the higher dielectric constant is positively polarized versus the other. Because of its high dielectric constant, water is usually positively polarized in comparison to the surface of fused silica microchannel. Hence, if an electric field is applied across the microchannel, the mobile ions of the solution migrate with their hydrate water towards the cathode resulting in a flow of the whole solution. Figure 2.1 demonstrates structure of electric double layer with inner stern layer in the electroosmosis phenomenon.

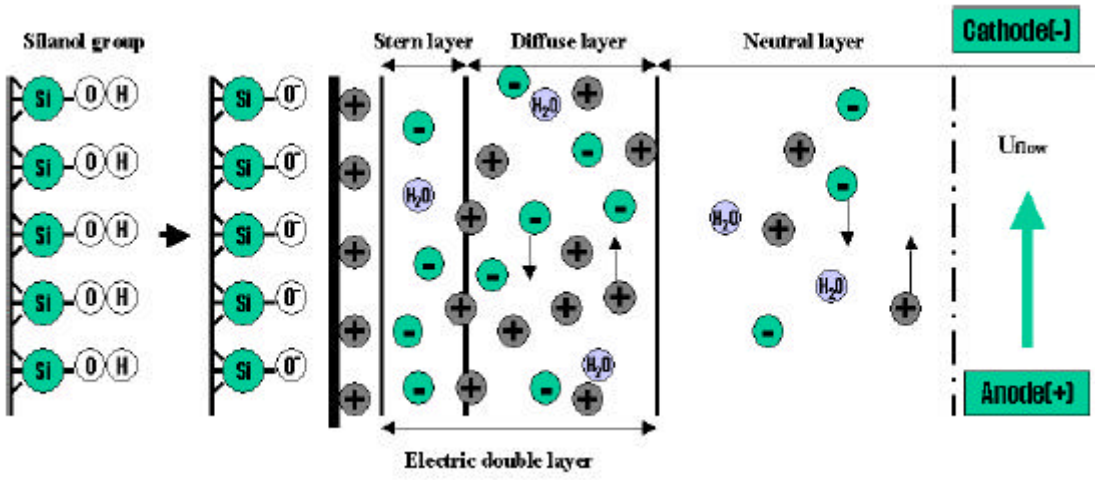

Figure 2.1. Structure of electric double layer with inner stern layer

Dissociation of functional surface groups and/or adsorption of ions in the electrolyte solution are the most important processes in electroosmosis. The zeta potential, which is defined as

the potential at the shear surface between the charge surface and the electrolyte solution, is a consequence of the existence of surface charge, and can give information on electrical interaction forces between the dispersed particles. The zeta potential is given by

$$\varsigma = \frac{4\pi\delta e}{\varepsilon} \qquad (2.1)$$

where δ is the thickness of the electric double layer, e is the charge per unit surface area, and ε is the dielectric constant of the buffer. The thickness of the electric double layer, which is approximately 1nm ~ 100nm thick in the aqueous solution, is inversely proportional to the concentration of the buffer.

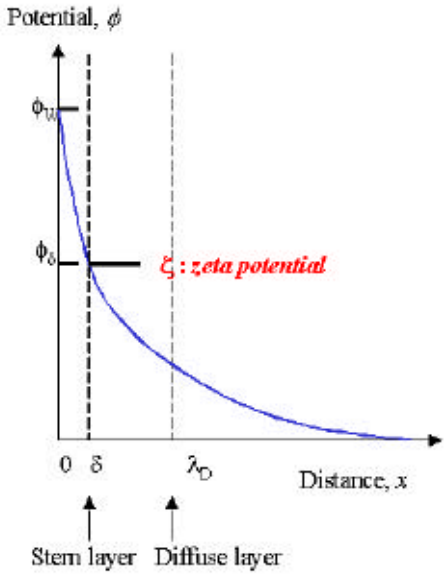

Figure 2.2. Schematic of the zeta potential (ς)

Electroosmotic flow has a relatively flat profile, as shown in Figure 2.3, compared to the pressure driven flow that frictional forces at the liquid-solid boundaries cause a strong pressure drop across the microchannel. This uniform velocity profile is ideal for transporting immersed or solvated substances with minimal hydrodynamic dispersion [38].

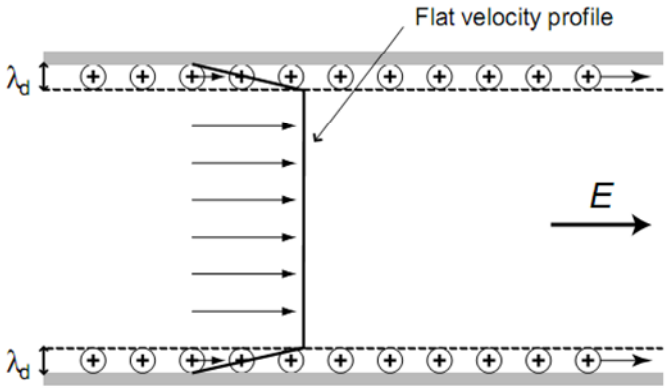

Figure 2.3. Velocity profile of the electroosmotic flow

The velocity of the EOF is proportional to the applied electric field as given in the following equation:

$$U_{eo} = \mu_{eo} E \qquad (2.2)$$

where μ_{eo} is electroosmotic mobility and E is electric field. The electroosmotic mobility depends on the zeta potential (ς), the dielectric constant (ε) of the medium and the viscosity (η) of the solution as follows:

$$\mu_{eo} = \frac{\varsigma \varepsilon}{4\pi\eta} \qquad (2.3)$$

There are two benefits of electroosmotic flow in the micro-fluidic devices. First, since all solutes must be carried though the microchannel, the electroosmotic flow, which has a flat flow profile, can make all of the solute molecules experience the same velocity component caused by electroosmotic forces regardless of their cross-sectional position in the micrchannel. The second benefit is that electroosmotic flow does not need moving parts like a check valve to control micro-fluidic flow which enables microfluidic systems to have a much simpler design.

2. 2. Marangoni Flow

To explain Marangoni flow, basic knowledge about surface tension is presented here first. Surface tension is an effect within the surface layer of a liquid that causes that layer to behave as an elastic sheet. It allows insects, such as the water strider, to walk on water. It allows small metal objects such as needles, razor blades, or foil fragments to float on the surface of water.

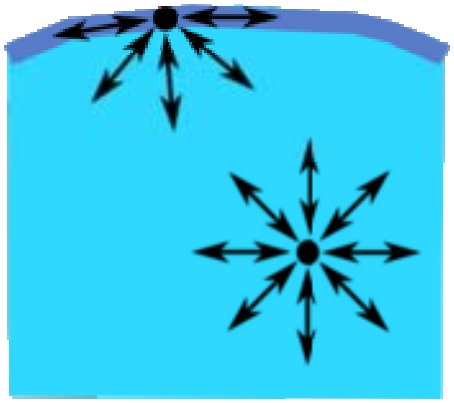

Figure 2.4. Diagram of the forces on a molecule of liquid

Surface tension is caused by the attraction between the molecules of the liquid by various intermolecular forces. In the bulk of the liquid each molecule is pulled equally in all directions by neighboring liquid molecules, resulting in a net force of zero (as seen in Figure 2.4). At the surface of the liquid, the molecules are pulled inwards by other molecules deeper inside the liquid and are not attracted as intensely by the molecules in the neighboring medium (be it vacuum, air or another liquid). Therefore, all of the molecules at the surface are subject to an inward force of molecular attraction which can be balanced only by the resistance of the liquid to compression. This inward pull tends to diminish the surface area,

and in this respect a liquid surface resembles a stretched elastic membrane. Thus the liquid squeezes itself together until it has the locally lowest surface area possible.

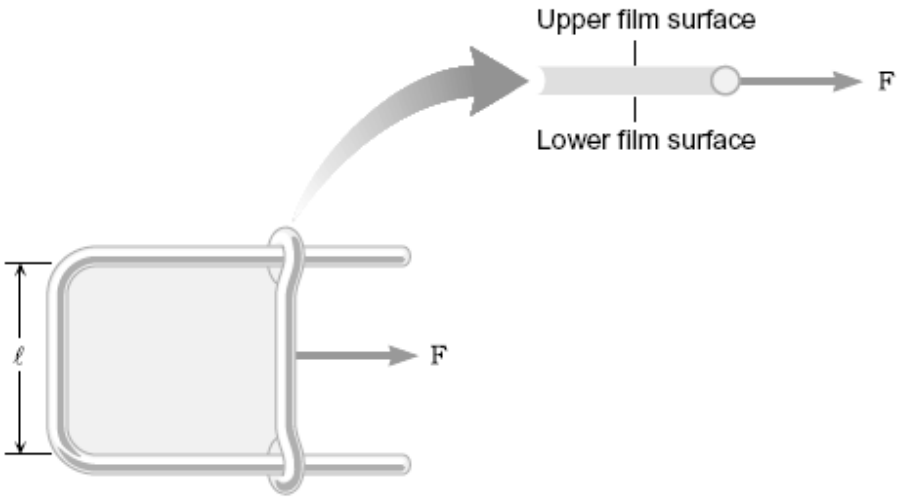

Figure 2.5. A simple apparatus to measure the surface tension of a liquid

The surface tension σ is the magnitude F of the force exerted parallel to the surface of a liquid divided by the length L of the line over which the force acts. For the specific case illustrated in Figure 2.5, there is an upper surface and a lower surface, as the blow-up drawing indicates. Thus, the force F acts along a total length of $L = 2l$, where l is the length of the slider.

$$\sigma = \frac{F}{L} = \frac{F}{2l} \qquad (2.4)$$

The Marangoni flow is induced by Marangoni effect which is the mass transfer on, or in, a liquid layer due to surface tension differences. Since a liquid with a high surface tension pulls more strongly on the surrounding liquid than one with a low surface tension, the presence of a gradient in surface tension will naturally cause the liquid to flow away from regions of low

surface tension. The surface tension gradient can in turn be caused by concentration gradient [35, 36, 39] or by a temperature gradient [40, 41].

Stowell and Korgel [39] conducted surface tension measurement of chloroform solvent in which 3.5 and 5nm gold nanocrystals were dispersed. The surface tension of the solvent was found to increase with increasing particle concentration for both particle sizes. The increase in surface tension with increased concentration was presumably resulted from the much lower volatility of the nanocrystals relative to the solvent.

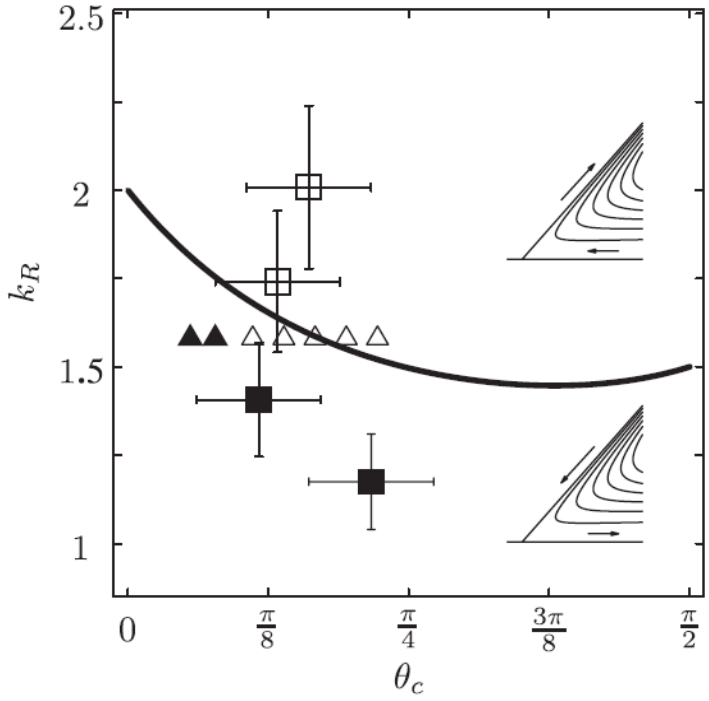

Figure 2.6. Experimental observations and numerical calculations of the circulation direction inside evaporating drops. (By Ristenpart et al [41])

Ristenpart et al [41] established quantitative criteria for the magnitude and direction of thermal Marangoni flow inside evaporating sessile drops. The circulation direction was found

to depend on both the contact angle (θ_C) and the ratio of substrate and liquid thermal conductivities (k_R). The definition of k_R is given by:

$$k_R = \frac{k_S}{k_L} \tag{3.5}$$

where k_S is the substrate conductivity and k_L is the liquid conductivity. Their analysis indicates that the drop is warmest at the contact line only if the substrate conductivity ratio k_R is greater than 2. In this situation, the consequent Marangoni flow is directed radially outward along the substrate (as seen in Figure 2.6). For $1.45 < k_R < 2$, the direction of the temperature gradient (and the resulting flow) depends on the contact angle θ_C, while for $k_R < 1.45$ the drop is coldest near the contact line and the circulation direction is reversed, i.e., radially inward along the substrate.

To illustrate the conclusions of Ristenpart et al [41] on a whole droplet scale, a schematic is shown in Figure 2.7. When k_R is greater than 2, the thermal Marangoni flow in the middle of the droplet moves downward. To the contrary, when k_R is less than 1.45, the thermal Marangoni flow in the middle of the droplet moves upward.

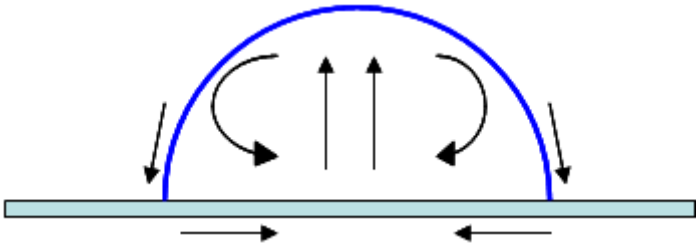

a. k_R <1.45

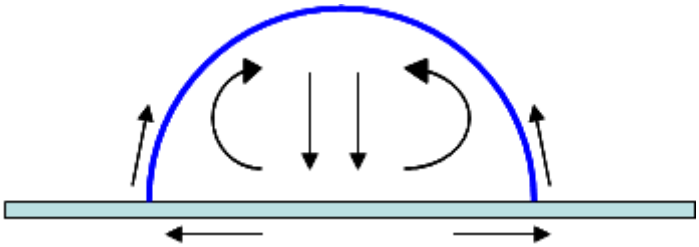

b. k_R >2

Figure 2.7. Schematic of thermal Marangoni flow patterns for different k_R

CHAPTER 3: MICROCHANNEL FABRICATION

In recent years, the research of fluid character in the micro-fluidic systems has been attracting attention of scientists [42-44]. Microfluidic devices have many advantages over conventional bench-top systems. The list of these advantages includes-but is not limited to – reduced size of operating systems, flexibility in design, reduced use of regents, reduced production of wastes, decreased requirements for power, increased speed of analyses, and portability. The design and development of a functional microfluidic device must take into account the type of material used to fabricate the device. Early developments were mostly based on conventional semiconductor materials and technologies. There are many limitations on fabrication, packaging and testing of micro-fluidic devices, such as the geometrical limit of wet-etching, wafer-to-wafer misalignment [45], and the difficulty of measurement due to the opacity of wafer. More recently, various microchannels made of glass and polydimethylsiloxane (PDMS) have been fabricated depending on their applications. Glass possesses favorable biocompatible properties and is inert toward most of the chemicals used in conventional biochemical analyses [46]. In the meanwhile, PDMS is receiving increasing amount of attention because of its attractive physical and chemical properties: elasticity, optical transparency, flexible surface chemistry and low permeability to water [47]. In this thesis, two microchannel fabrication methods are interpreted; one is using both PDMS and glass while the other is utilizing glass only. The discussion of the difference between these two methods is also presented.

3.1. PDMS-Glass Hybrid Microchannels Fabrication Process

The summary of the Y-shaped PDMS-Glass Hybrid microchannel fabrication process is shown in Figure 3.1 and the detailed process is described as follows:

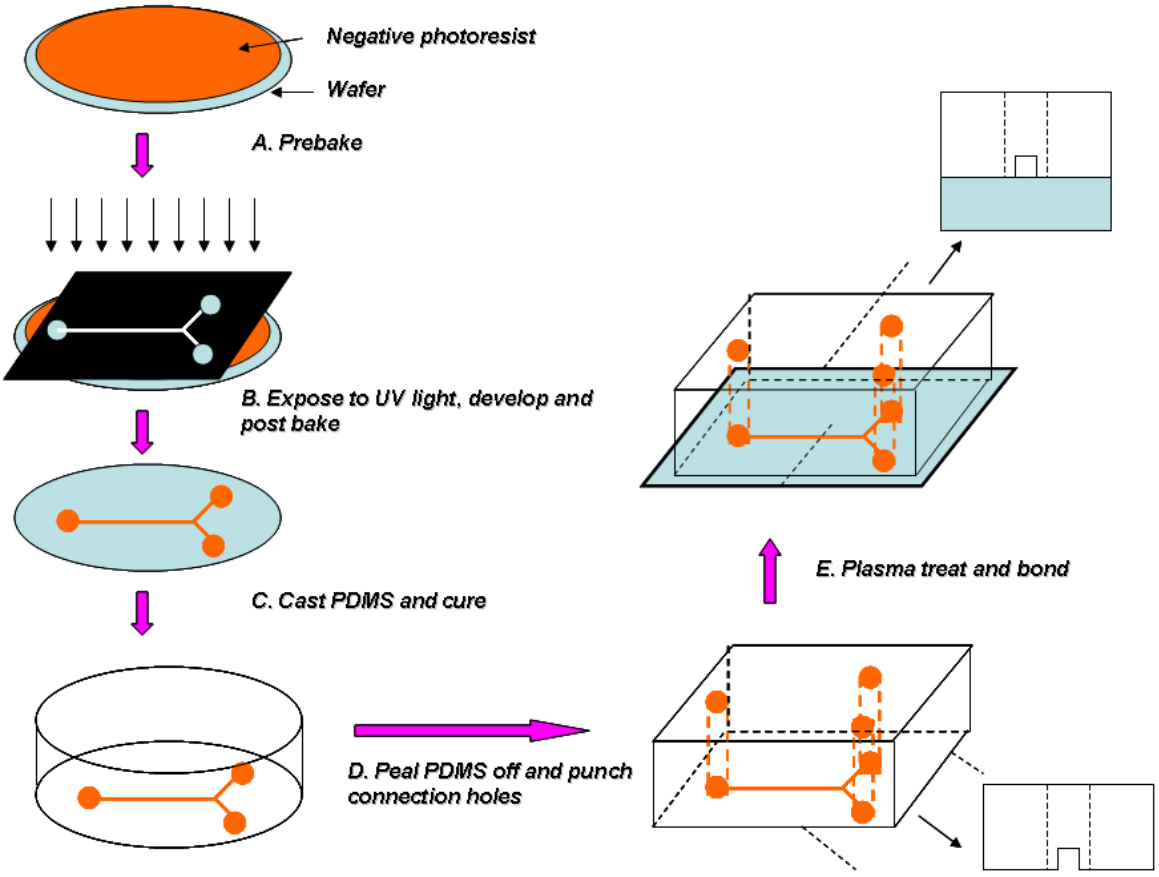

Figure 3.1. Summary of PDMS-Glass Hybrid Microchannel Fabrication

3.1.1. Photoresist coating and photopatterning

The photomask was designed with the software named Adobe Illustrator and printed on a high-resolution transparency film of 10000 dpi (CAD/Art Services, Inc). The mold was made from patterned negative photoresist (SU-2100, Microchem) on a 5-in silicon wafer (University Wafer) which was put in a spinner. A puddle of photoresist was dispensed first

onto the substrate carefully to avoid introducing air bubbles. Then the spinner ramped up to 500 rpm in 25 seconds and stays there for 5 sec. After that, by accelerating at 300 rpm/s, the spinner reached its highest speed, 2500 rpm, and held for 35 sec. The substrate was then baked in for 35 min at $65^0 C$ and photopatterned with UV light for 18s (365nm; 500W). It was again baked for 10 min at $95^0 C$ before immersion into the developer (Microchem) for 7 min. Finally, the developed substrate was quickly rinsed with isopropyl alcohol (Fisher) and dried with high purity nitrogen.

3.1.2. Casting PDMS

Polydimethylsiloxane (PDMS) elastomer (Sylgard (R) 184 Silicone Elastomer Kit, Dow Corning) was used to make the upper part of the channel. The PDMS polymer was mixed with the curing agent in a 10:1 ratio and exposed to low pressure in a desiccator (EW-06514-20, Cole-Parmer) to remove bubbles formed during mixing. The prepolymer mixture was poured over the mold and again placed in the desiccator to remove bubbles. The PDMS casting was then cured in a convection oven at $65^0 C$ for 1 hr.

3.1.3. Microchannel Assembly

The PDMS slab was removed from the mold and three wells, each with a diameter of 3mm, were formed in it with a sharp hand-punch. The PDMS slab was then placed in an ethanol bath in an ultrasonic cleaner for 15 min to clean the surface and subsequently dehydrated in a convection oven at $65^0 C$ for 10 min. A micro slide (75 x 50 x 1mm, Corning) was used as the lower portion the microchannel and was treated under a 350mTorr stream of air in a RF-plasma cleaner (Yes-R1, Yield Engineering Systems) for 5 minutes. To seal the two pieces together, both the PDMS slab and the glass substrate were subjected to RF-plasma treatment

under a 1-Torr stream of oxygen for 1 min. The PDMS slab was then bonded to the glass plate by bringing the two components into conformal contact immediately after plasma treatment. The plasma oxidation also changed the surface of the PDMS microchannel from hydrophobic to hydrophilic. To let the surface remain hydrophilic, the microchannel was kept filled with DI water. All the above procedures were performed in a class 10/100 clean room.

3.1.4. Gluing Reservoirs

After assembling the microchannel, four reservoirs were glued to its top by using Dow Corning 732 KTV Sealant. The smallest one was a NanoPort from Upchurch Scientific which can be connected to a syringe with a pipe of 360μm inside diameter. By drawing the syringe, the fluids were driven though the Y-shaped microchannel.

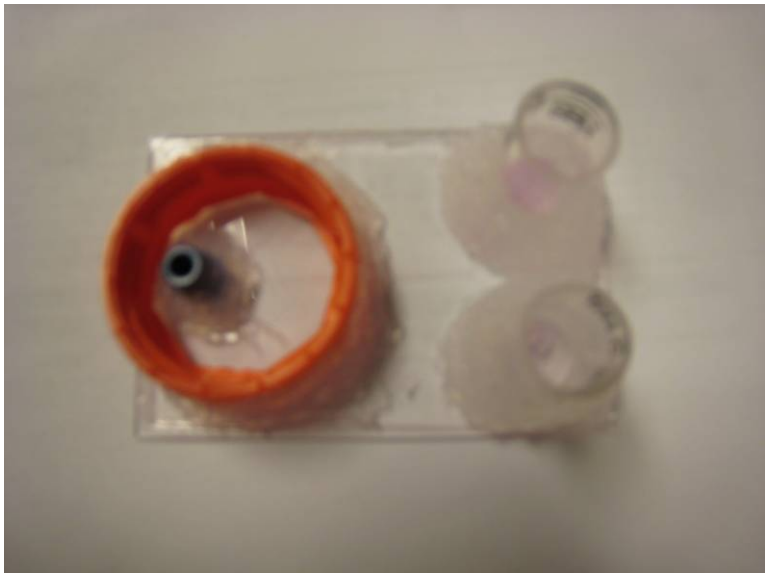

Figure 3.2. Y-shaped PDMS-Glass Hybrid Microchannel

Figure 3.2 shows the Y-shaped PDMS-Glass hybrid microchannel (top view) made by using the process listed above.

3.2. Glass Microchannels Fabrication Process

The summary of the Y-shaped PDMS-Glass Hybrid microchannel fabrication process is shown in Figure 3.3 and the detailed process is described as follows:

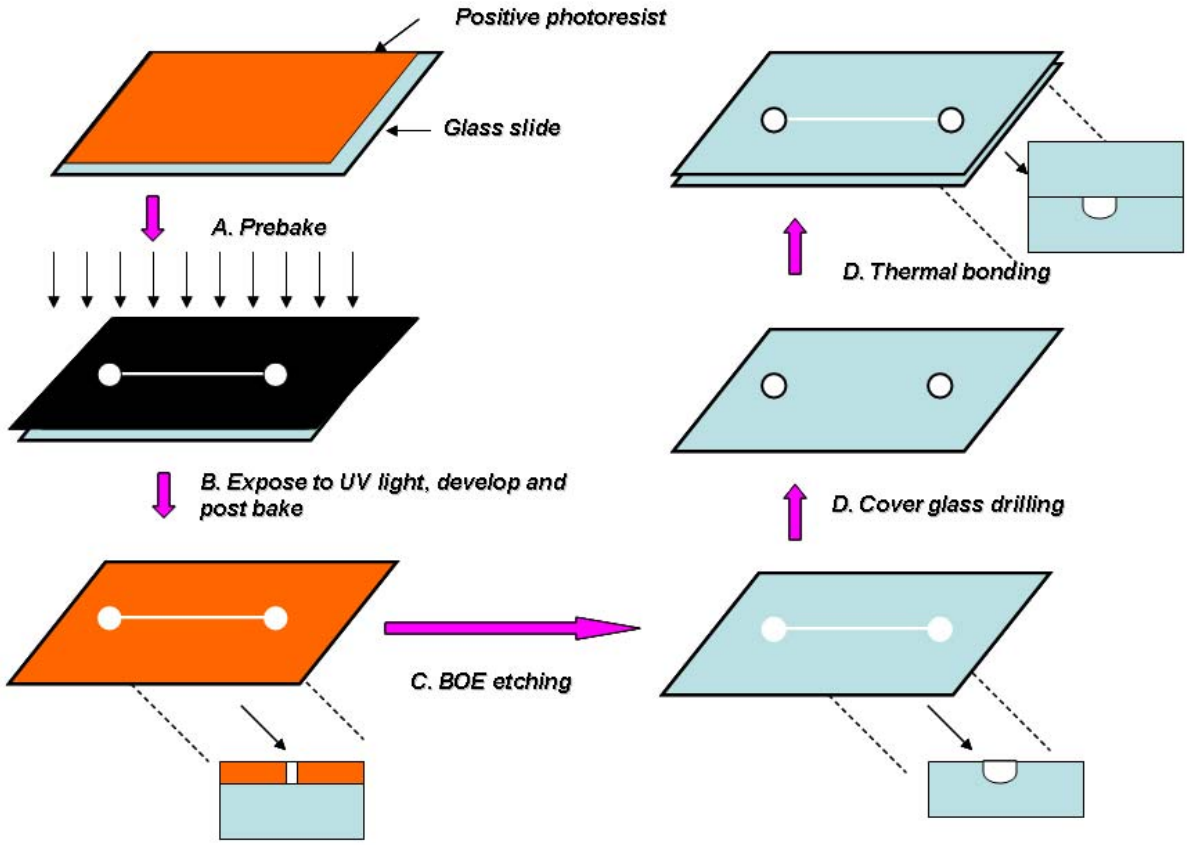

Figure 3.3. Summary of Glass Microchannel fabrication

3.2.1. Photoresist coating and photopatterning

The present study used commercially available microscope glass slides of dimension 75 x 50 x 1 mm, supplied by Corning. Prior to fabrication, the slide was cleaned with a boiling solution ($Hcl(\%)/H_2O_2(\%)=1$) for 15 min. It was then rinsed in DI water and blown dry with nitrogen gas. To ensure the complete removal of residual water molecules, a

dehydration process was carried out by baking the slides in a convection oven for 5 minutes at a temperature of $100^0 C$.

Following the dehydration process, the slide was coated with positive photoresist (AZ5214, Microchem) using a spin coater (KW-4A, Chema Tech.) operating at 4000 rpm for 40 sec, and then baked at $90^0 C$ for 30 min. Using a photomask that was fabricated in-house, the substrate was then exposed to UV light (500W at 365nm; ABM Inc.) for 90 sec. Finally, it was immersed in resist developer (Microchem) for 1 min, rinsed with DI water, dried in a stream of high purity nitrogen, and post-baked at $120^0 C$ for 15 min.

3.2.2. Etching and Bonding

After setting in BOE (Buffered Oxide Etch) tube for 100 min, the substrate was then rinsed with acetone, methyl alcohol, and DI water. Then it was dried with high purity nitrogen. Two holes with a diameter of 2mm were drilled for sample inlets and outlets on another cover plate. The two plates were cleaned with a boiling solution ($Hcl(\%)/H_2O_2(\%)=1$) for 15 min. It was then rinsed in DI water and blown dry with nitrogen gas. To ensure the complete removal of residual water molecules, a dehydration process was carried out by baking the slides in a convection oven for 5 minutes at a temperature of $100^0 C$. The etching depth was $60\,\mu m$. Finally, the base and cover plates were set on an alumina plate and fusion-bonded in a furnace at $600^0 C$ for 6 hours.

3.2.3. Gluing Reservoirs

After assembling the microchannel, three reservoirs were glued to its top using a Dow Corning 732 KTV Sealant. The smallest one was a NanoPort from Upchurch Scientific which can be connected to a syringe with a pipe of 360μm inside diameter. By drawing the syringe, the fluids were driven through the Y-shaped microchannel.

Figure 3.4 shows the Glass microchannel (top view) made by using the process listed above.

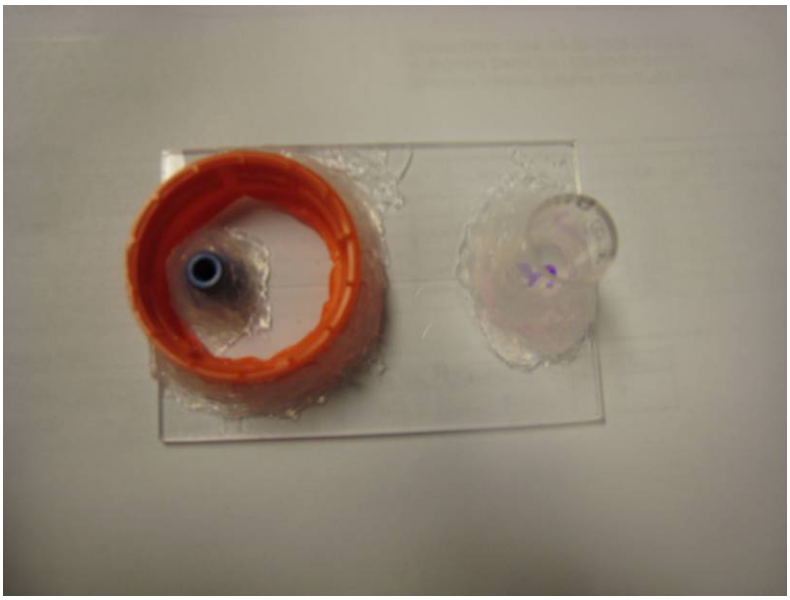

Figure 3.4. Straight Glass Microchannel

	Glass-PDMS Hybrid microchannel	**Glass microchannel**
Photoresist (Positive mask)	Negative	Positive
Channel Formation	PDMS cast	BOE etching
Hole Drilling	Punched	Drilled
Surface Cleaning	Ultrasonic bath (PDMS)	$H_2SO_4(\%) / H_2O_2(\%) = 3:1$
Bonding	Plasma treat	Conventional thermal bonding
Time (hours)	5	24

Table 3.1. Differences of the fabrication process between PDMS-Glass Hybrid Microchannels and Glass Microchannels

Table 3.1 shows the main differences of the fabrication process between the PDMS-Glass Hybrid and Glass microchannels. As seen in Table 3.1, the fabrication process of a Glass microchannel takes a much longer time than that of a Glass-PDMS hybrid microchannel.

CHAPTER 4: MIXING ENHANCEMENT IN A STRAIGHT Y-SHAPED MICROCHANNEL BY UTILIZING ELECTROKINETIC INSTABILITY

In this chapter, a parametric study was carried out to elucidate underlying physics and to quantify the effectiveness of manipulating EKI waves to actively control/enhance fluid mixing inside a Y-shaped microchannel. Epifluorescence microscopy technique was used to conduct qualitative flow visualization and quantitative scalar concentration field measurements to quantify the fluid mixing process inside the Y-shaped microchannel in terms of scalar concentration distribution, shedding frequency of the EKI waves, and scalar mixing efficiency. The effects of the relevant parameters, such as the conductivity ratio of the two mixing streams, the strength of the applied static electric fields, and the frequency and amplitude of the applied alternating perturbations, on the evolution of the EKI waves and resultant fluid mixing process were investigated systematically.

4.1. Epifluorescence Microscopy

Epifluorescence microscopy is a method of fluorescence microscopy that is widely used in life sciences [48]. The excitatory light is passed from above (or, for inverted microscopes, from below), through the objective and then onto the specimen instead of passing it first through the specimen (as shown in figure 4.1). (In the latter case the transmitted excitatory light reaches the objective together with light emitted from the specimen). The fluorescence in the specimen gives rise to emitted light which is focused to the detector by the same

objective that is used for the excitation. A filter between the objective and the detector filters out the excitation light from fluorescent light. Since most of the excitatory light is transmitted through the specimen, only reflected excitatory light reaches the objective together with the emitted light and this method therefore gives an improved signal to noise ratio. A common use in biology is to apply fluorescent or fluorochrome stains to the specimen in order to image a protein or other molecule of interest.

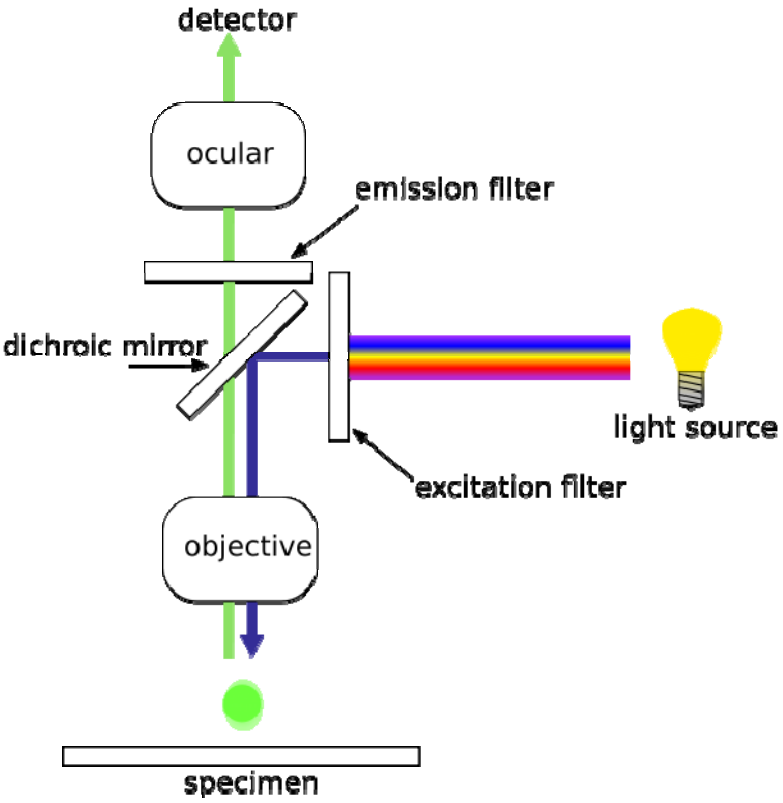

Figure 4.1. Schematic of a fluorescence microscope

The reason why fluorescence dyes can be used in present study as the indicator of mixing process in Y-shaped microchannels is explained as follows:

When a photon of given energy is absorbed by a fluorophore, the energy state of the molecule transits from the ground state to higher electronic states. Energy is subsequently dissipated at these excited states until the molecule reaches the lowest level of the first excited singlet state. Thereafter, the molecule at the first singlet state can return to the ground state in multiple ways. One such path of return is via fluorescence, defined as a radioactive decay process wherein no further energy is dissipated by collisions and the return of the excited molecule to the ground state occurs purely by the emission of energy. In such a scenario, a portion of the remaining energy is lost by the molecule before the emission and consequently, the emitted energy is of longer wavelength than the energy it initially absorbed. This shift in the wavelength of the fluorescence light relative to the absorption wavelength is referred to as the Stokes shift.

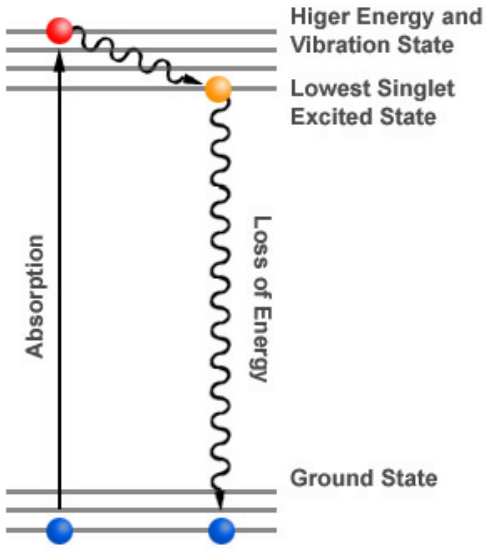

Figure 4.2. Schematic of the generation of Fluorescence

For a dye of concentration C (kgm^{-3}) illuminated with an incident light flux of intensity I_0 (Wm^{-3}), the fluorescence energy emitted per unit volume, I (Wm^{-3}), is

$$I = I_0 C \phi \varepsilon \qquad (4.1)$$

where ε is the absorption coefficient of the dye and Φ is its quantum efficiency. For most organic dyes, variations in I with temperature are predominantly attributable to the temperature dependence of the quantum efficiency. Therefore, in principle, if one can maintain I_0 and T constant, the concentration of a fluorescent dye solution can be measured through variations of fluorescence intensity associated with the concentration dependence of C. The measured concentration fields can be used to quantify the mixing process in microchannels of the present study.

4.2. Experimental Details

The Y-shaped microchannel used in the present study is made of poly-di-methyl-siloxane (PDMS) by using a rapid-prototyping "photolithography" technique [49]. The dimensions of the microchannel are given in Fig. 4.3. The cross section of the channel is rectangular with 320 μm in width and 130 μm in height. The length of both inlet branches is 15.0mm and the angle between the two inlet branches is 90^0. The length of the mixing channel is 40.0mm. Relatively large reservoirs at the inlets and outlet of the Y-shaped microchannel are designed in order to minimize the effect of the induced pressure head difference between the inlets and outlet during the experiments.

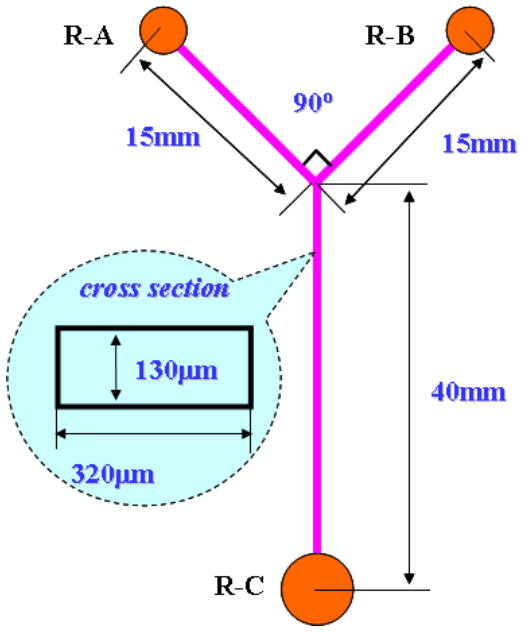

Figure 4.3. The schematic of the Y-shaped microchannel

Deionized water was used as the working fluid in the present study. The DI water was filtered by using a syringe filter unit (Millipore millex-FG, Bedford, 0.2µm) before experiments. Borate buffers (Science Stuff Inc) were used to adjust the molecular conductivity of the two fluid streams. Rhodamine B, which is reported to be neutral for pH values ranging 6.0 to 10.8 [50], was used as the fluorescent dye for qualitative flow visualization and quantitative scalar concentration measurements. Since the molar concentrations of the borate buffers (<10mM) and Rhodamine B (< 0.16 mM) are low, the changes in water physical properties such as the permittivity and viscosity are negligible.

DI water was used to flush the microchannel several times prior to use for experiments.

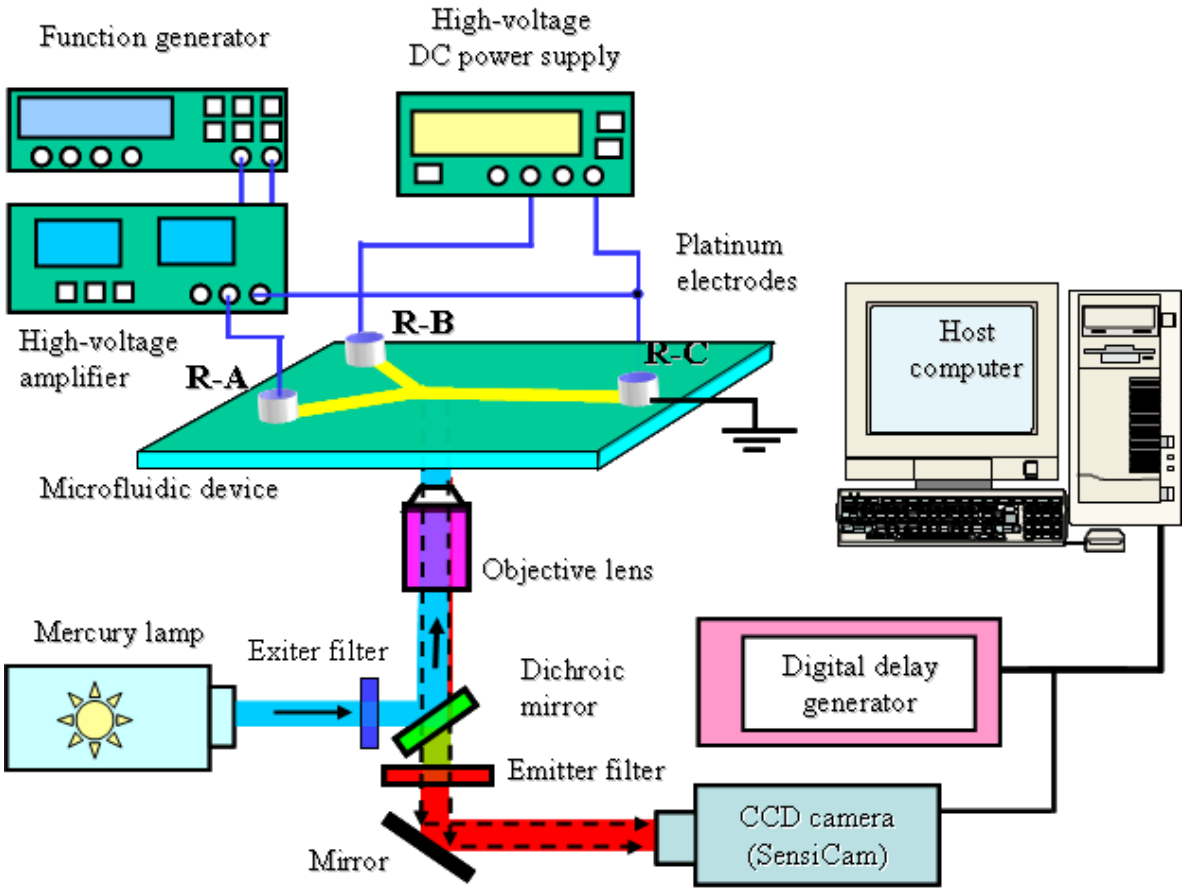

Figure 4.4. Experimental setup

Figure 4.4 shows the schematic of the experimental setup used in the present study. The microchip with the Y-shaped microchannel was placed on the test bed of an inverted fluorescent microscope (Leica DM-IL). A high-voltage DC power supply (Keithley, Model 247) was used to provide a static electric field between the reservoirs R-B and R-C. A function generator (Instek, Model GFG-8250A) and a high-voltage amplifier (Trek, Model 609-E) were used to apply a static electric field or a static electric field along with an

alternating perturbation between the reservoirs R-A and R-C. The electrodes installed in the reservoirs were made of platinum.

A mercury lamp was used as the illumination source in the present study. Passing through an epi-fluorescent prism (Excitation Filter of 532nm with 10nm BP, Dichroic 532nm RDC, Emitter of 610nm with 75 nm BP), the bright light from the mercury lamp was used to excite the Rhodmamine B molecules seeded in the stream R-A. Upon excitation, the seeded fluorescent tracer, Rhodmine B molecules, would emit fluorescence with its emission peak at about 580nm. A 10X objective lens (NA=0.4) was used for the fluorescence imaging. The fluorescence light was captured by a high-resolution CCD camera (SensiCam-QE, Cooke Corp). The CCD camera was connected to a workstation (host computer) via a digital delay generator (Berkeley Nucleonics, Model 565) for the image acquisition timing control, data storage and imaging processing. For the present study, the exposure time of the CCD camera was set at 7ms. Five-hundred fluorescence images were recorded at a frame rate of 10 Hz for each case.

It should be noted that the depth averaging along the optical axis is an artifact of epi-fluorescence imaging to study microflows. All the fluorescent molecules across the imaging depth of the 10X objective would contribute to the measured fluorescence intensity. Based on the formula suggested by Inoue & Spring [51], the depth of focus for the 10X (NA=0.4) objective used in the present study is estimated to be about 5.0 μm. For all the experimental

results reported here, the focus plane of the 10X objective was set in the middle plane of the 130 μm depth microchannel.

It is well known that the collected fluorescence intensity is proportional to the amount of the fluorescent molecules in the flow for diluted solution and unsaturated excitation. Quantitative scalar concentration distributions can be derived from the acquired fluorescence images. The effects of the non-uniformity of the illumination intensity, background noise, and the dark current of the CCD camera were corrected in the present study in order to minimize the measurement errors in the determination of scalar concentration distributions to quantify the scalar mixing process [18].

4.3. Quantification of Fluid Mixing Effectiveness

In order to correct the effects of the non-uniformity of the illumination intensity, background noise and the dark current of the CCD camera, we use the method by Posner and Santiago [18] to obtain the concentration for each pixel:

$$C_i(x,y) = \frac{I_i(x,y)_{raw} - \overline{I(x,y)_{dark}}}{\overline{I(x,y)_{flat}} - \overline{I(x,y)_{dark}}} \qquad (4.2)$$

where,

$$\overline{I(x,y)} = \frac{\sum_{i=1}^{n} I_i(x,y)}{n} \qquad (4.3)$$

The instantaneous image index is *i* and the subscripts *raw*, *flat* and *dark* denote the raw, flat-field, and dark-field images, respectively. The flat-field images are recorded with the

channels filled with a uniform concentration of dye and correct for illumination non-uniformity and detector response. The dark-field images are recorded with the channels filled with buffer. The dark-field images correct for external light scattered off channel walls and not for chromatically filtered fluorescence of wall adsorbed dye, and sensor dark-noise. Two hundred dark and flat-field images are recorded before each experiment.

Following the work of Johnson et al. [52], a statistical approach was used in the present study to quantify the fluid mixing process in the Y-shaped microchannel.

$$\eta = 1 - \frac{\sqrt{\frac{1}{n}\sum_{i=1}^{n}(C_i - C_{ip})^2}}{\sqrt{\frac{1}{n}\sum_{i=1}^{n}(C_{i0} - C_{ip})^2}} \tag{4.4}$$

where n is the total number of pixels, C_i the concentration at the ith pixel, C_{i0} the concentration at the ith pixel with no mixing or diffusion, and C_{ip} the concentration at the ith pixel for a homogeneous mixture. The concentration values for C_{i0} was determined by doubling the concentration profile, C_{ip} , at half the channel width, and then setting the concentration of the opposite half of the channel to zero. The high value of η means that the fluorescent dye is well stirred.

4.4. Experimental Results and Discussions

4.4.1. The effect of conductivity ratio of the two mixing streams in the Y-shaped microchannel on the critical strength of the applied static electric field.

In the present work, a parametric study was conducted to quantify the effect of the conductivity ratio of the two mixing streams on the critic strength of the applied static electric field to trigger EKI waves in a Y-shaped microchannel. During the experiments, the concentration of borate buffer solution in inlet reservoir R-B was kept constant at 10mM and the concentration of the borate buffer in inlet reservoir R-A was changed from 0.1mM to 5mM. It makes the conductivity ratio of the two mixing streams, $\gamma = \sigma_B / \sigma_A$, being 2:1, 5:1, 10:1, 50:1 and 100:1. Rhodamine B molecules were seeded in the stream R-A to visualize the evolution of the interface of the two mixing streams.

In order to determine the critical strength of the applied static electric field to trigger the periodic shedding of convective EKI waves at a selected conductivity ratio, a small static voltage was applied between the inlets and outlet of the Y-shaped microchannel at first. Then, the applied voltage was increased in the step of every 25 volts until noticeable fluctuations of the interface of the two adjacent streams could be observed. During the experiments, the same static voltage was applied to both inlet reservoirs R-A and R-B at all times, i.e., $V_A = V_B$. The required minimum voltage to induce observable fluctuations at the interface of the two adjacent streams is defined as the critical voltage of the applied electric field at that selected conductivity ratio.

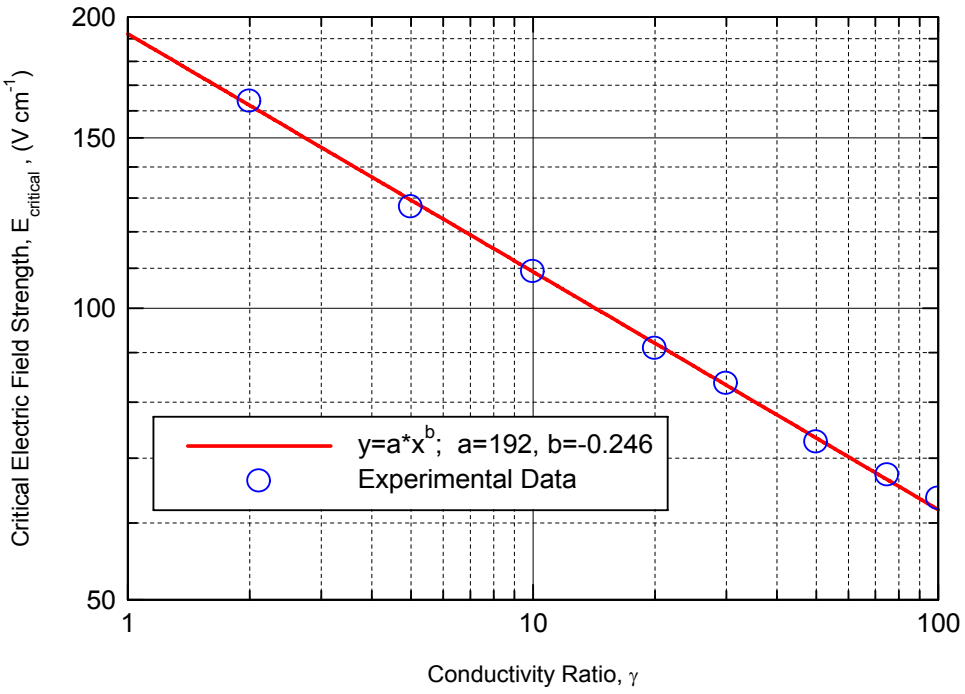

Figure 4.5. Critical strength of the applied electric field vs. conductivity ratio

Figure 4.5 shows the measured critical strength of the applied static electric field as a function of the conductivity ratio of the two mixing streams inside the Y-shaped microchannel. A curve of a power function is also given in this figure to fit the measurement data. It can be seen clearly that the critic strength of the applied static electric field decreases rapidly (the power index of the power function is -0.246) with the increasing conductivity ratio. The critical strength was found to be about $E_{critic} \approx 160\ Vcm^{-1}$ as the conductivity ratio being 2. It drops to about $E_{critic} \approx 60\ Vcm^{-1}$ as the conductivity ratio increases to 100. This can be explained by stating that a larger conductivity ratio would induce a higher free charge density, ρ_e, as suggested by Hoberge & Melcher [11] with a relationship of $\rho_e = -\frac{\varepsilon}{\sigma} \nabla\sigma \bullet E$, where σ the electrical conductivity of the fluid, ε the electrical permittivity of the fluid, and E the external electric field. The greater induced electric charges coupled with the applied

electric field would generate a stronger Coulombic force at the interface of the two adjacent streams to overcome the dissipative effects of the molecular diffusion to promote EKI. Therefore, the critical strength of the applied static electric field would decrease rapidly with the increasing conductivity ratio of the two mixing streams in the Y-shaped microchannel.

It should be noted that, although Posner & Santigao [18] reported a similar trend about the dependence of the critic strength of the applied static electric field on the conductivity ratio of the mixing streams, the present study is the first to reveal that the relationship can be represented well by a power function. It should also be noted that the absolute values of the critical strength for the present study (i.e., for two-streams mixing in the Y-shaped tunnel) were found to be much smaller than those reported by Posner & Santigao [18] (for three-stream mixing in a cross-shaped microchannel). For example, for the same conductive ratio of $\gamma = 10$, the critical strength of the applied electric field to trig EKI waves in the Y-shaped microchannel is $E_{critic} \approx 110\ Vcm^{-1}$ for the present study. Posner & Santigao [18] reported that the critical strength would be as high as $E_{critic} \approx 420\ Vcm^{-1}$ in order to trigger EKI waves for the three-stream mixing in the cross-shaped mcirochannel. This indicates that the required strength of the applied static electric field would be affected by many other factors as well, in addition to the conductivity ratio of the mixing streams. It highlights the necessity of much more systematic studies to establish a compressive database to document EKI and associated flow phenomena in order to further our understanding about EKI and to explore/optimize design paradigms for the development of robust EKI micro-mixers for various microfluidics or “lab-on-a-chip” applications.

a. γ =2 b. γ=5 c. γ=10 d. γ=50 e. γ=100

Figure 4.6. The effect of the conductivity ratio on the fluid mixing process

Figure 4.6 shows typical instantaneous fluorescence images of the fluid mixing inside the Y-shaped channel under the same applied static electric fields of $E \approx 180 Vcm^{-1}$, however, with different conductivity ratio of the two mixing streams. Even though the strength of the applied electric field was kept constant, the fluid mixing process was found to become increasingly turbulent and intensive as the conductivity ratio increases, i.e., the fluid mixing process was found to be enhanced significantly as the conductivity ratio of the two mixing streams increases.

4.4.2. The effect of the applied electric field strength on the evolution of EKI waves

A systematic study was also conducted to investigate the effect of the strength of the applied electric field on the evolution of the EKI waves and the fluid mixing process inside the Y-

shaped microchannel. During the experiment, the conductivity ratio of the two mixing streams is kept constant, i.e., $\gamma = 10$. The same static voltages were applied to both the inlet reservoirs R-A and R-B, i.e., $V_A = V_B$, with the applied voltage varied from 100V to 2000V (i.e., $E \approx 18 \sim 365 Vcm^{-1}$).

Figure 4.7 shows typical fluorescence images under different strengths of the applied static electric field. As visualized clearly in the images, the interface of the two adjacent streams was found to be straight and "clean" as the applied static voltage is relatively low (i.e., < 550V). No noticeable fluctuations of the interface of the two mixing streams can be observed. The fluid mixing was found to concentrate in a very thin layer along the straight interface of the two streams, and the fluid mixing process was found to be diffusion dominated. As the applied voltage becomes greater than 550V (i. e., $E > 110\ Vcm^{-1}$), the interface was found to fluctuate and generate observable convective EKI waves, which were found to propagate downstream.

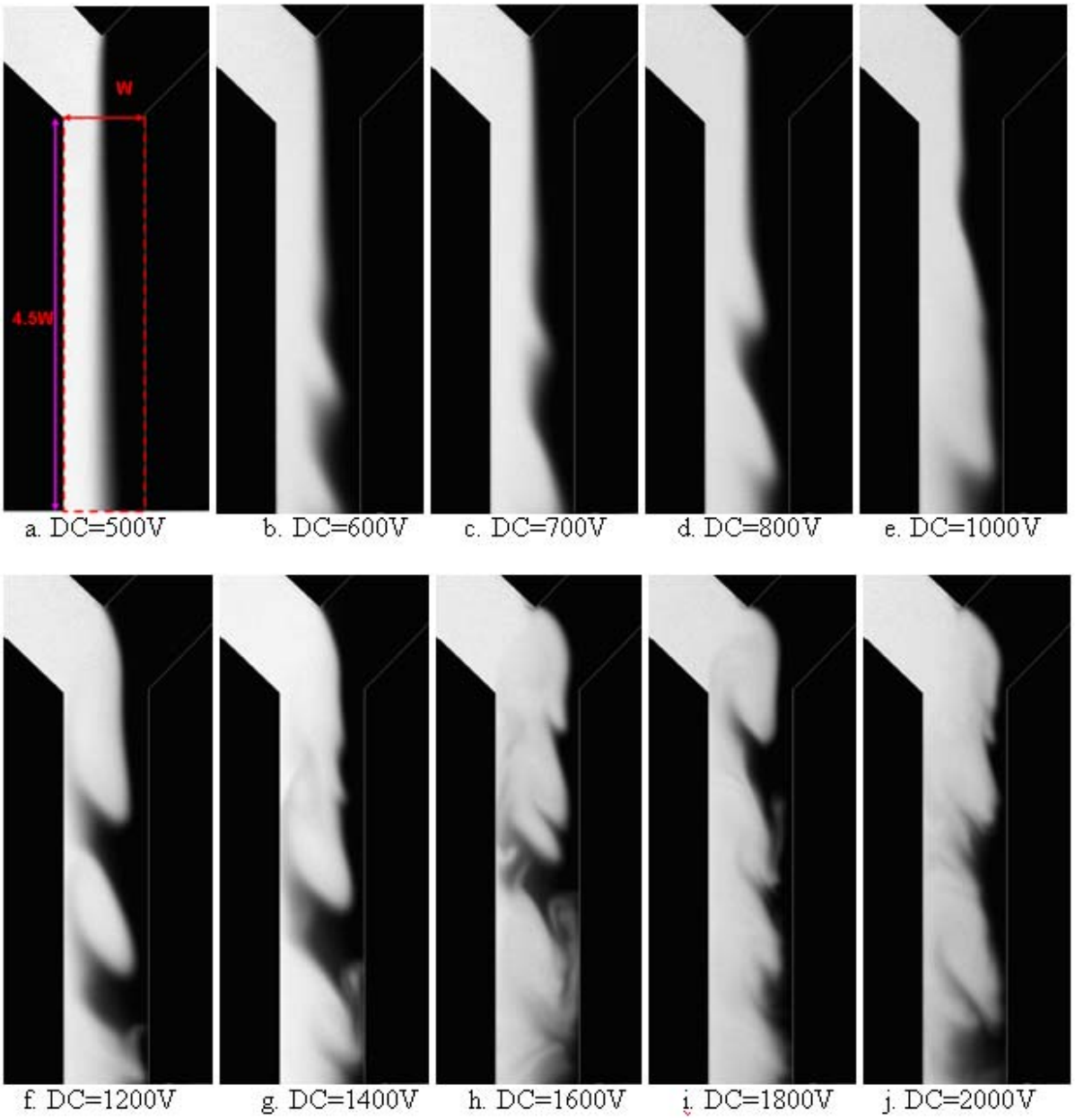

Figure 4.7. The effect of the applied electric field strength on the fluid mixing (γ=10)

The generation of the convective waves was found to be periodic. The shedding frequency of the EKI waves can be identified from the scalar temporal power spectra based on the time sequence of the captured fluorescence images, and the results are given in Fig. 4.8.

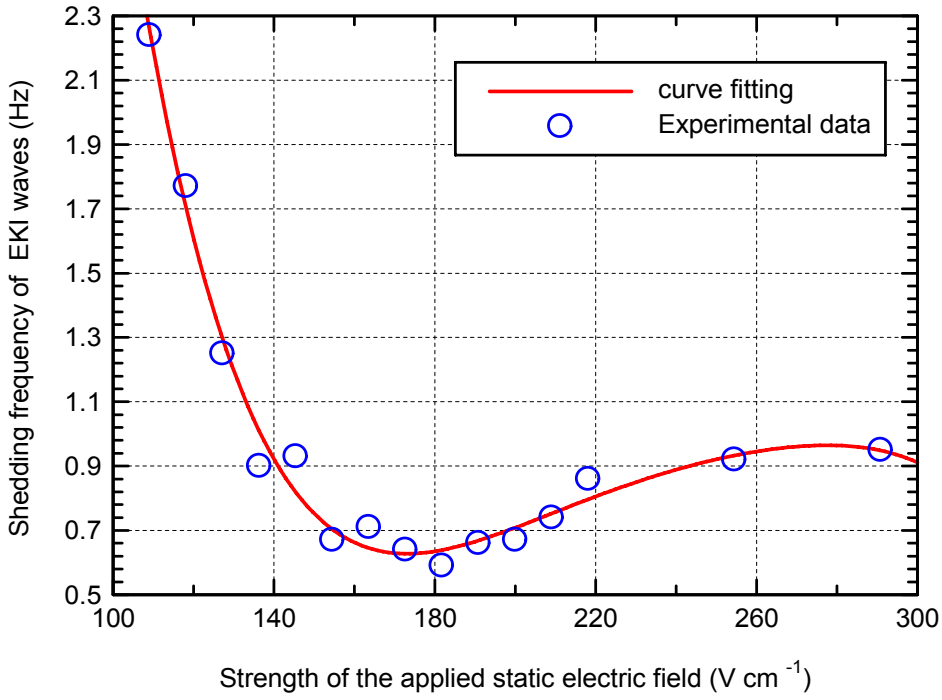

Figure 4.8. The effect of the applied electric field strength on shedding frequency of EKI waves

The amplitude of the interface fluctuation, i.e., the size of the convective EKI waves, was found to increase rapidly as the applied static voltage increased. When the applied static voltage is less than 1000V (i.e., $E<180\ Vcm^{-1}$), the interface of the two mixing streams was found to be "clean" and "laminar" while it was curved due to the periodic shedding of the EKI waves. The shedding frequency of the EKI waves was found to decrease with the increasing voltage of the applied static electric field when the applied static voltage is relatively low (i.e., $E<180\ Vcm^{-1}$).

As the applied static voltage becomes higher than 1000V (i.e., $E>180\ Vcm^{-1}$), additional smaller EKI waves were found to be generated in the braid regions of the large convective EKI waves. The smaller EKI waves were found to propagate upstream instead of downstream. Due to the generation of the additional smaller EKI waves, the shedding frequency of the convective EKI waves was found to increase slightly with the increase of the applied static voltage. The generation of the convective EKI waves became much more random and the interface of the adjacent streams became much "dirtier" and fussier when the applied static voltage is higher than 1200V (i.e., $E>218\ Vcm^{-1}$,). As the applied static voltage becomes higher than 1400V (i.e., $E>255Vcm^{-1}$), the fluid mixing process in the microchannel was found to become much more turbulent and chaotic. The scalar temporal power spectra based on the time sequence of the fluorescence images were found to become continuous energy spectra and no obvious peak can be identified when the applied static voltage become larger than 1600V (i.e., $E>290\ Vcm^{-1}$).

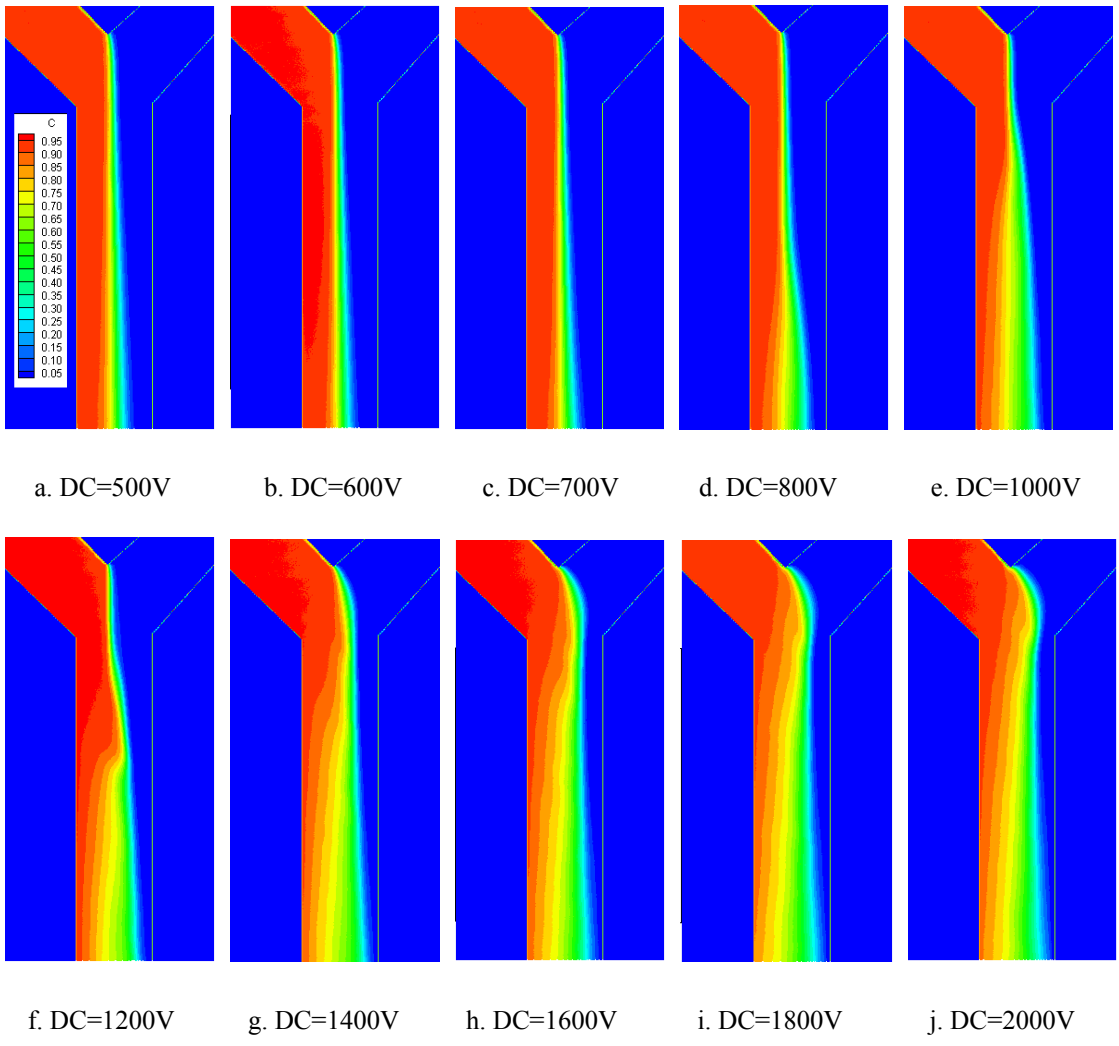

a. DC=500V b. DC=600V c. DC=700V d. DC=800V e. DC=1000V

f. DC=1200V g. DC=1400V h. DC=1600V i. DC=1800V j. DC=2000V

Figure 4.9. Ensemble averaged concentration fields by applying static electric fields with different amplitudes

Figure 4.9 shows the ensemble averaged concentration fields by applying static electric fields with different magnitudes. The interfacial contact surface area of the two adjacent streams increases as the increase of the amplitude of the alternative perturbations. It should be noted that when the strength of the static electric fields is relatively low (DC<1400V), the interfacial contact surface area in the conjunction part does not change much. However, as

the strength of the static electric fields keeps increasing (DC>1400V), the interfacial contact surface area in the conjunction part begins to change.

In order to quantify the effect of the strength of the applied static electric fields on the fluid mixing process inside the microchannel more clearly, fluid mixing efficiency under different strengths of the applied electric field were calculated. The interrogation area used for the fluid mixing efficiency calculation is shown in Figure 4.7a, and the calculated fluid mixing efficiency data are given in Figure 4.10. It can be seen clearly that the fluid mixing efficiency increase monotonically with the increasing strength of the applied static electric field.

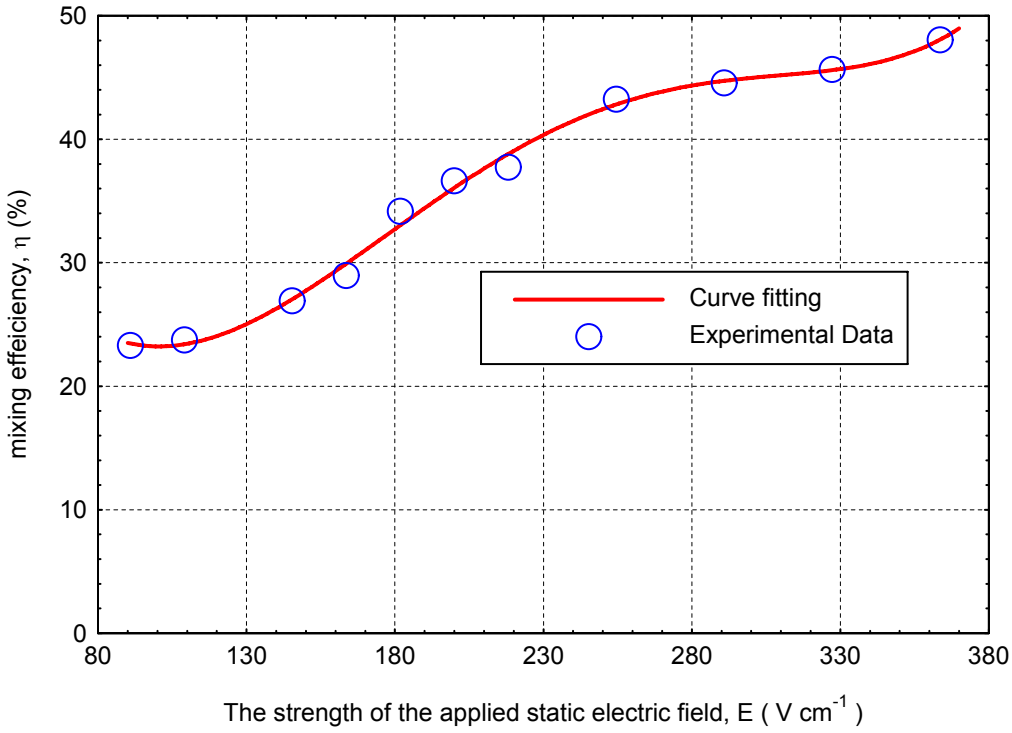

Figure 4.10. The Mixing efficiency vs. the strength of the applied static electric field

4.4.3. Manipulating the EKI waves and fluid mixing process by adding alternative perturbation to the applied static electric field.

Although Shin et al.[19] demonstrated the feasibility of adding alternative perturbations to applied static electric fields to manipulate EKI waves for fluid mixing control, the effects of relevant parameters such as the frequency and amplitude of the alternative perturbation on the evolution of EKI waves and the resultant fluid mixing have not been fully investigated. In the present study, a systematic investigation was conducted to quantify the effectiveness of adding alternative perturbations to the applied static electric field to manipulate EKI waves for further enhancement of fluid mixing in the Y-shaped microchannel. During the experiments, while the same static voltage of 1000V was applied to the inlet reservoirs R-A and R-B, an alternative perturbation was added to the inlet reservoir R-A. Therefore, the voltages applied to the inlets of the Y-shaped microchannel were:

$$\begin{aligned} V_A &= V_{DC} + \widetilde{V}_{AC} = V_{DC} + A_{AC}\sin(2\pi f_{AC}) = 1000V + \sin(2\pi f_{AC}) \\ V_B &= V_{DC} = 1000V \end{aligned} \qquad (4.5)$$

By changing the frequency, f_{AC}, and amplitude, A_{AC}, of the alternative perturbation, the effects of the applied alternative perturbation on the evolution of the EKI waves and the resultant fluid mixing efficiency in the Y-shaped microchannel were assessed.

A mixing augmentation factor is introduced in the present study to quantify the augmentation in fluid mixing due to the addition of the alternative perturbation to the applied static electric field. The mixing augmentation factor, *MAF*, is defined as:

$$MAF = \frac{\eta_{static+perturbation}}{\eta_{static\,only}}, \qquad (4.6)$$

where $\eta_{static\ only}$ is the fluid mixing efficiency for the case without the alternative perturbation. $\eta_{static+\ perturbation}$ represents the fluid mixing efficiency when the alternative perturbation was added to the applied static electric field. $MAF>1.0$ indicates that the fluid mixing process is enhanced by adding an alternative perturbation to the applied static electric field, while $MAF<1.0$ represents that the fluid mixing process is suppressed by the addition of the alternative perturbation.

4.4.3a. The effect of the frequency of the alternative perturbation

During the experiment, the amplitude of the alternative perturbation was kept constant, i.e., A_{AC} =250V. The frequency of the applied alternative electric perturbation was changed from 0.1 Hz to 100 Hz.

According to the experimental data given in Figure 4.8, the shedding frequency of the EKI waves under a static voltage of 1000V ($E\approx 182\ Vcm^{-1}$) between the inlets and the outlet of the Y-shaped microchannel was 0.60 Hz (i.e., $f_{DC}=0.60Hz$). Figure 4.11 shows the mixing augmentation factor as a function of the frequency of the alternative perturbation. While Shin et al. [19] suggested that adding alternative perturbation to applied static electric field can both enhance and suppress fluid mixing of three fluid streams in a cross-shaped microchannel, depending on the frequency of the added alternative perturbation. The measurement results of the present study given in Figure 4.11 indicate clearly that the fluid mixing of the two fluid streams in the Y-shaped microchannel can always be enhanced by adding the alternative perturbation to the applied static electric field.

The mixing augmentation factor was found to reach its peak value as the frequency of the alternative perturbation was about 0.6Hz, which is close to the natural shedding frequency of the EKI waves under the applied static electric field of 1000V ($E \approx 182\ Vcm^{-1}$). When the frequency of the applied alternative electric perturbation is too high (f_{AC} >10 Hz) or too low (f_{AC} < 0.1 Hz) compared with the natural shedding frequency of the EKI waves, the applied alternative perturbations were found to be able to barely affect the evolution of the convective EKI waves, therefore, the mixing augmentation factor was found to be slight bigger than 1.0.

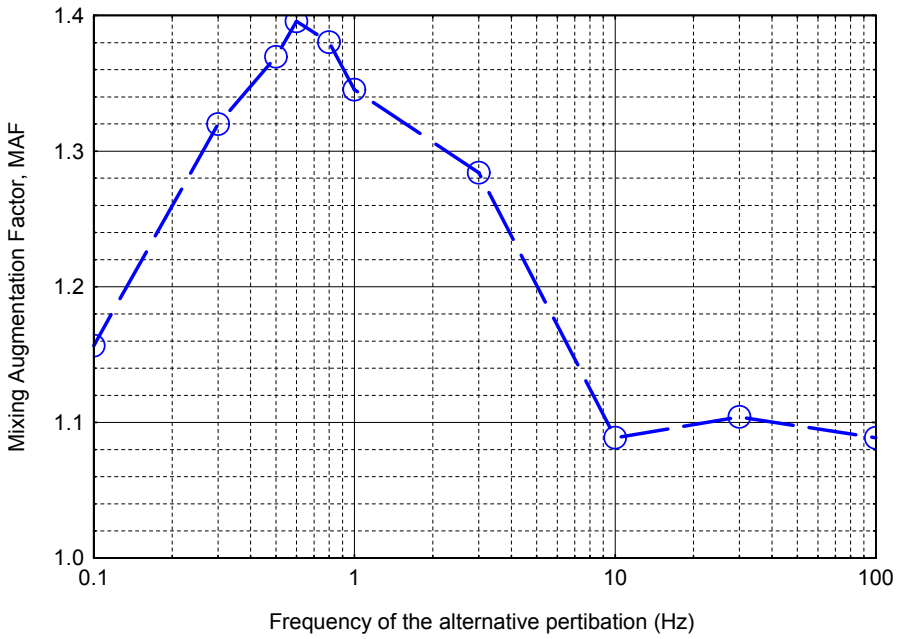

Figure 4.11. Mixing augmentation factor vs. the frequency of the alternative perturbation

The measurement results of the present study indicate clearly that the fluid mixing process inside the Y-shaped microchannel could be most enhanced when the frequency of the applied alternative perturbation equals to the natural shedding frequency of the EKI waves. This fact

may be explained by the concept of hydrodynamic resonance, which has been widely employed in many active flow control studies [52, 53]. The existence of the optimal perturbation frequency is expected to provide a valuable guideline for the design of an EKI micro-mixers for efficient fluid mixing inside microchannels.

It should be noted that Shin et al. [19] suggested that the optimum frequency for the applied alternative perturbation should be twice of the natural shedding frequency of the convective EKI waves when they studied the fluid mixing of three streams in a cross-shaped channel. The inconsistency about the optimum frequency of the alternative perturbation between the present study and Shin et al.[19] is believed to be closely related to the differences in mixing flow arrangement (two-stream mixing vs. three-stream mixing) and number of interfaces (one high-conductivity-gradient layer vs. two high-conductivity-gradient layers) involved in the two studies.

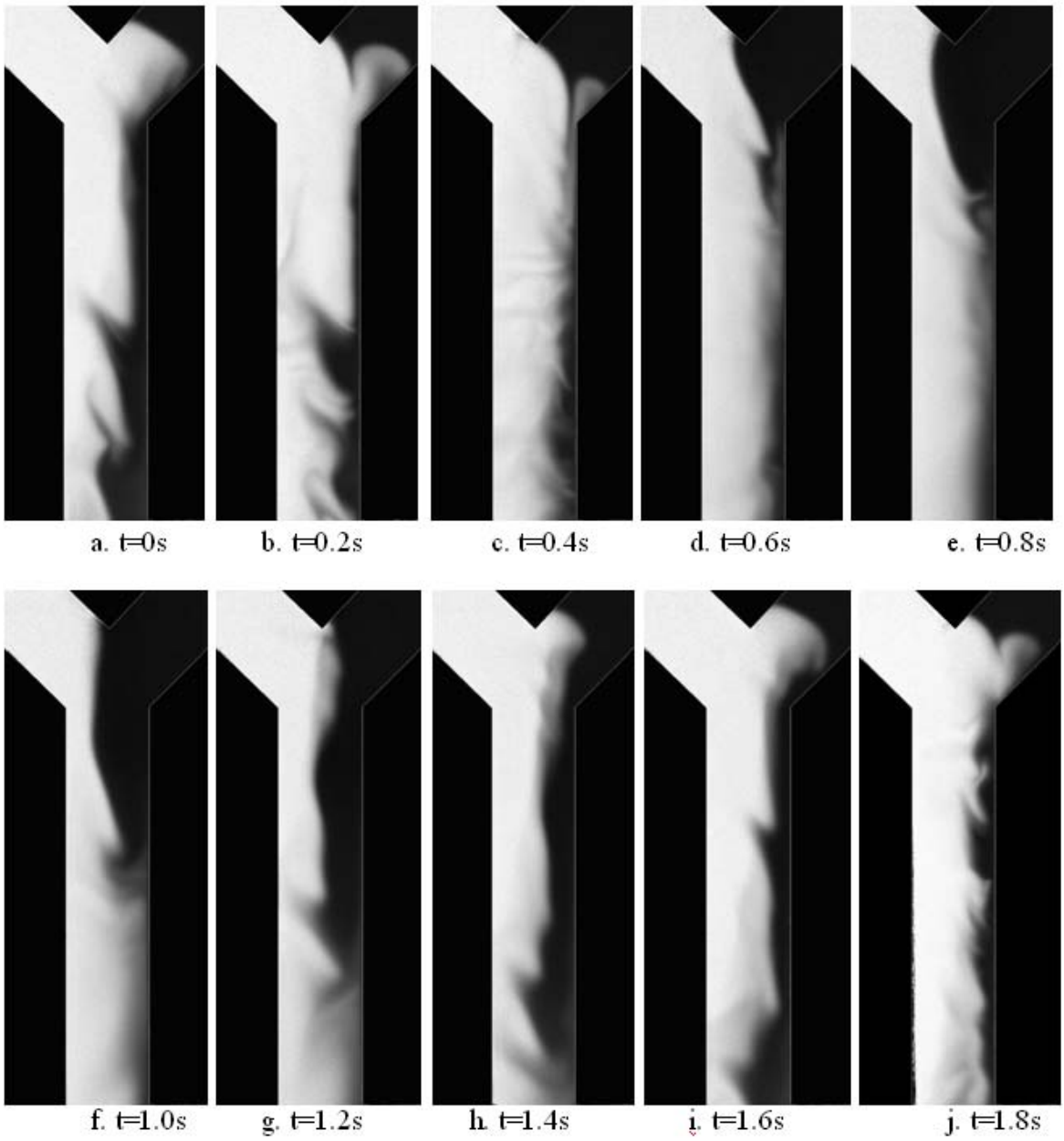

Figure 4.12. Time sequence of the fluorescence images within one cycle of the alternative perturbation (f_{AC}=0.60Hz)

Figure 4.12 shows the time sequence of the fluorescence images within one excitation cycle of the applied alternative perturbation with the frequency of the perturbation being 0.60Hz. The evolution of the EKI waves and the dynamics of the EKI mixing process under the

excitation of the alternative perturbation were revealed clearly from the time sequence of the fluorescence images.

4.4.3b. The effect of the amplitude of the alternative perturbation

Since the fluid mixing process was found to be most enhanced when the frequency of the applied alternative perturbation is close to the natural shedding frequency of the EKI waves, the frequency of the alternative perturbation was set to be the natural shedding frequency of the EKI waves (0.60 Hz) when studying the effect of the amplitude of the alternative perturbation on the evolution of the EKI waves and the resultant fluid mixing process. During the experiment, the parameters of V_{DC}=1000V, f_{AC}=*0.60Hz* were chosen. The amplitude of the alternative perturbation was changed from 50V to 500V.

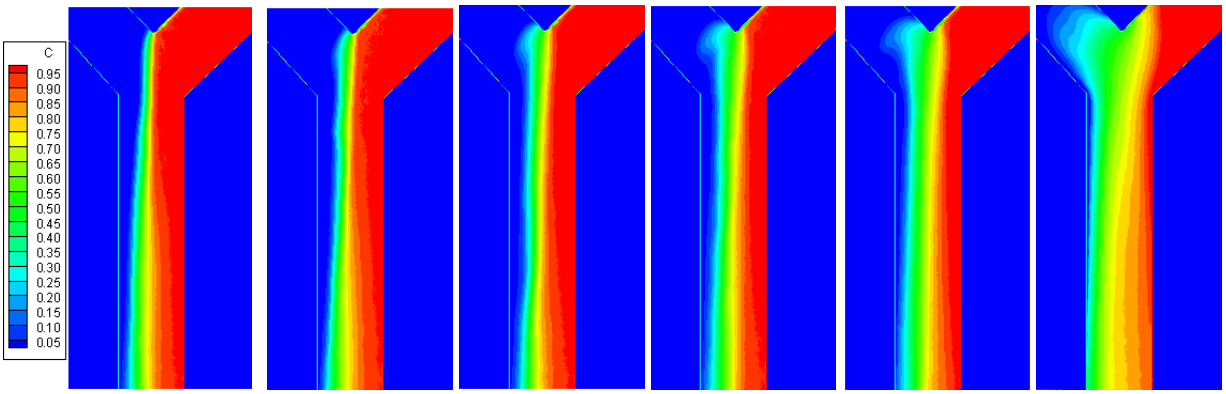

a. AC=50V b. AC=100V c. AC=200V d. AC=300V e. AC=400V f. AC=500

Figure 4.13. Ensemble averaged concentration fields by applying alternative perturbations with different amplitudes

Figure 4.13 shows the ensemble averaged concentration fields by applying alternative perturbations with different amplitudes. The interfacial contact surface area of the two

adjacent streams becomes larger and wider as the increase of the amplitude of the alternative perturbations.

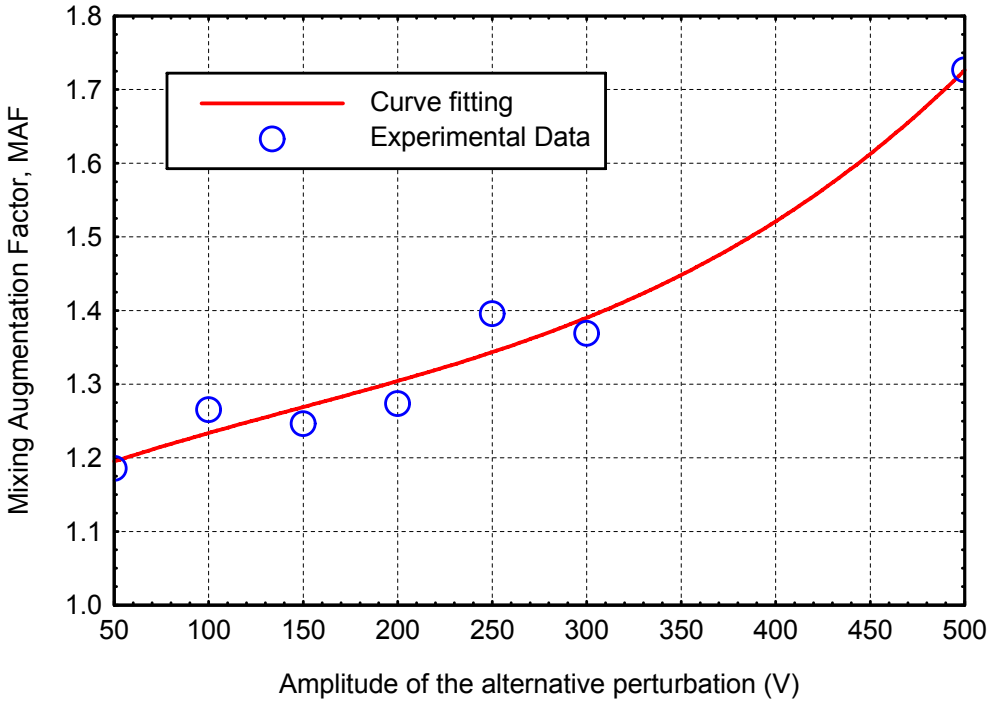

Figure 4.14. *MAF* versus the amplitude of the alternative perturbation

Figure 4.14 shows the profile of the measured mixing augmentation factor versus the amplitude of the alternative perturbation. It can be seen clearly that the fluid mixing efficiency is quite sensitive to the amplitude of the alternative perturbation. The mixing argumentation factor was found to increase almost linearly with the amplitude of the applied alternative perturbation when the perturbation amplitude is relatively small (<200V). The fluid mixing efficiency was found to increase much more rapidly as the perturbation amplitude became relatively large (> 200V).

CHAPTER 5: THE EFFECT OF GEOMETRY OF Y-SHAPED MICROCHANNELS ON MIXING ENHANCEMENT BY UTILIZING EKI

In this chapter, the effect of the geometry of different microchannels on the mixing enhancement was investigated by utilizing the EKI. Three Y-shaped microchannels were used, which are termed as channel with cavities, channel with steps, and straight channel. The mixing efficiencies in different depths of the channel with steps were first measured. Then, the evolution of the convective eletrokinetic waves and the fluid mixing process were compared among these microchannels that were applied with static electric fields. After that, by adding alternative electric perturbations to the static electric fields, the mixing enhancement was also investigated.

5.1. Channel and Reagents

By using the rapid-prototyping "photolithography" technique, the Y-shaped microchannels used in present study are made of poly-di-methyl-siloxane (PDMS) and glass, the dimension of which is shown in Figure 5.1. The channels are 320 μm in width and 130 μm in height. The two upper branches are 15.0mm in length, which form an angle of 90.0^0, while the length of the main channel part is 40.0mm. The specific structures of the conjunction part of the three microchannels are enlarged and shown in figure 5.1 as well. Three plastic cylinders are glued to the top of the channel acting as reservoirs. The diameters of the reservoirs for two inlets, R-A and R-B, are 12mm and the one for the outlet, R-C, is 32mm. The purpose of

using large reservoirs here is to eliminate the pressure driven flows induced by height differences when doing experiments. The electrodes put into the reservoirs are made of platinum.

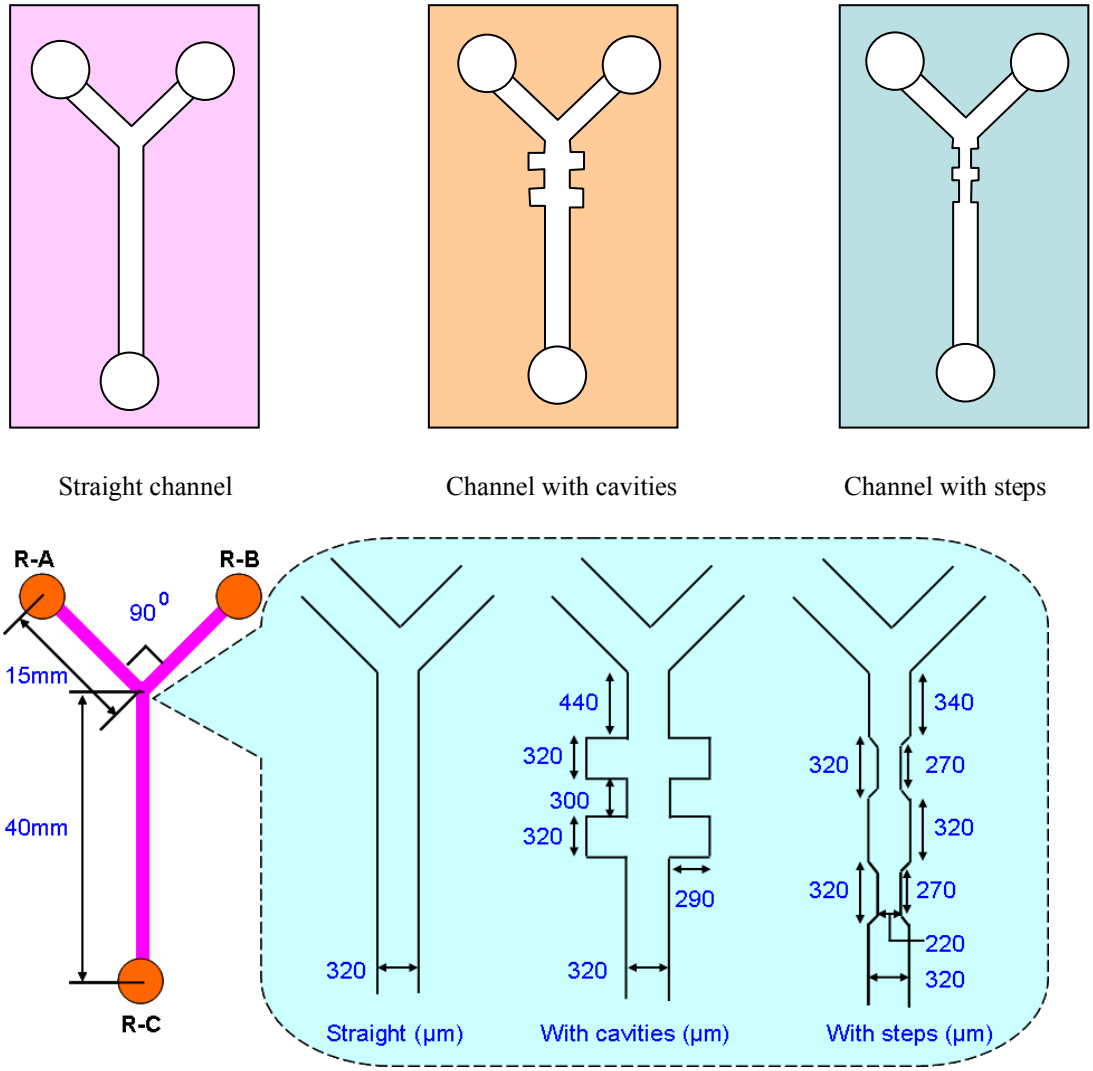

Figure 5.1. Schematic of the Y-shaped microchannels

For all the tests, Rhodamine B was dissolved in 10mM Sodium borate solution to a final concentration of 0.16mM and the mixture was put into reservoir R-A while reservoir R-B contains Sodium borate solution (1mM) only. Thus, the conductivity ratio of the two adjacent

streams in the microchannels was 10. All solutions were made using deionized water and filterd by syringe filter unit (Millipore millex-FG, Bedford, 0.2μm) before usage. As for the channels, they were cleaned with deionized water and sodium borate solution successively prior to use. And then, to eliminate the height difference of the solutions in reservoirs, the channel was set still for one and a half hours before any image was recorded.

5.2. Experimental setup

The same setup was used as explained in 4.2.

5.3. Results and Discussions

In order to quantify the mixing processes inside the microchannels, a small interrogation area is selected right after the structures in the conjunction part of the microchannels. Figure 5.2 shows the fluorescence images of the microchanels with interrogation areas on them. The areas are located 4.4W to the conjunction part of the microchannels and they occupy 25 x 240 pixels.

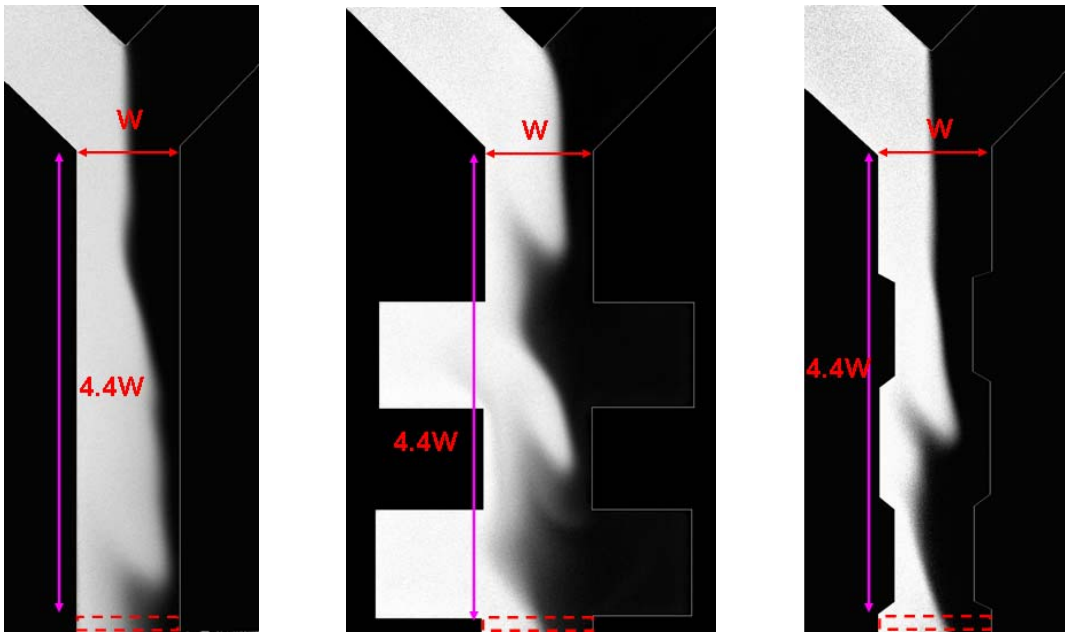

Figure 5.2. The fluorescence images of the microchannels

5.3.1. The mixing process in different depths of the channel with steps

Since the microchannels have a depth of 130μm and the depth of focus for the objective used in the present study is estimated to be about 5.0 μm, it is necessary to investigate the effect of the depth of the microchannels on mixing processes. The channel with steps was used to conduct this study and measured the mixing efficiencies at several depths of the microchannel under different static electric fields. As shown in Figure 5.3, the mixing efficiency does not change much at different depths. For the following study, the mixing processes in the middle depth of the microchannels were measured.

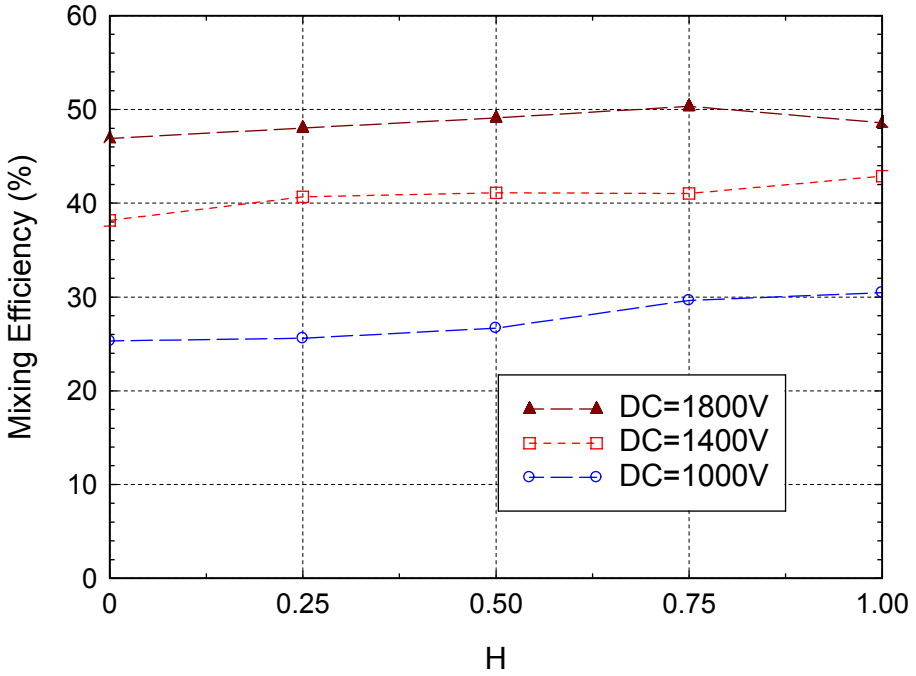

Figure 5.3. The mixing efficiency Vs the depth of the channel of steps

5.3.2. The effect of static electric field on the evolution of convective EKI waves

A systematic investigation was conducted to study the effect of the strength of the applied static electric field on the evolution of the convective EKI waves and the fluid mixing process inside the Y-shaped microchannels. During the experiments, the same static electric field was applied to both the inlet reservoirs, which varied from 100V to 2000V.

Figure 5.4 shows the instantaneous concentration fields of the Y-shaped microchannels under different strengths of the applied static electric fields. The bright side in the microchannels is the mixture of Rhodamine B and borate buffer of 10mM, while the dark side is the borate buffer of 1mM.

600V 800V 1000V 1400V 2000V

600V 800V 1000V 1400V 2000V

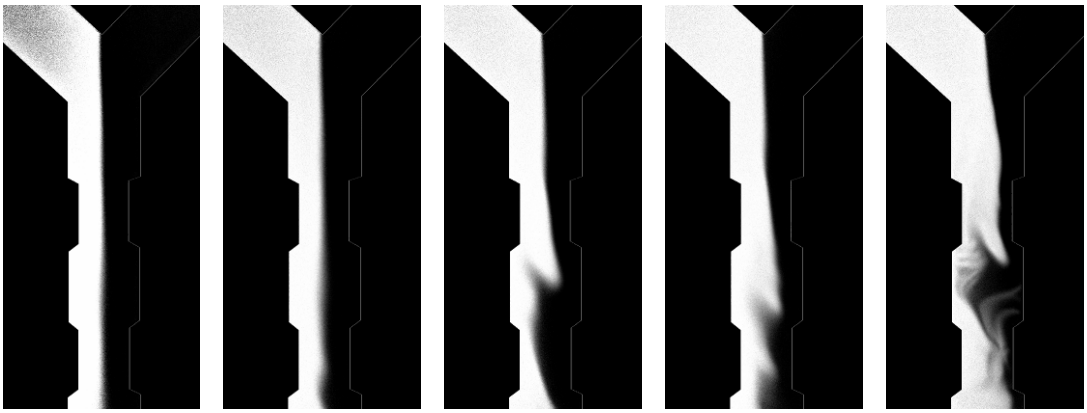

600V 800V 1000V 1400V 2000V

Figure 5.4. The instantaneous fluorescence images of the Y-shaped microchannels under different static electric fields

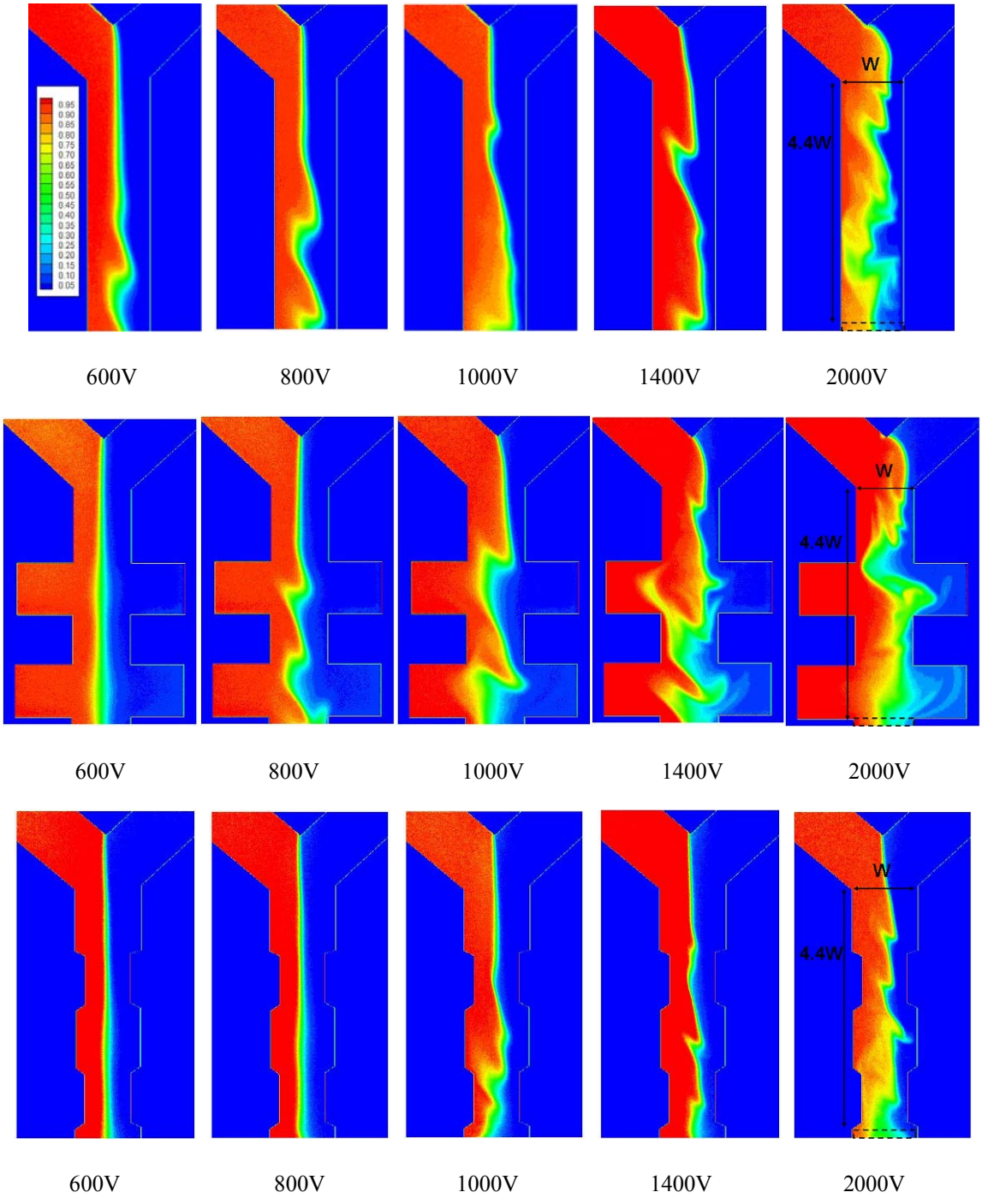

Figure 5.5. The instantaneous concentration fields of the Y-shaped microchannels under different static electric fields

Figure 5.5 shows the instantaneous concentration fields of the Y-shaped microchannels under different strengths of the applied static electric field. When the applied static voltage is relatively weak (i.e., =600V), the noticeable fluctuations can only be found in the straight channel. Once the strength is increased to 800V, an obvious interfacial wave is generated and propagated downstream of the channel with cavities. The apparent perturbations are found in the channel with steps as the strength of the applied static electric field keeps increasing. The EKI waves of the channel with steps have much smaller amplitudes as compared with those of the other channels. Since all these convective EKI waves are periodic, the shedding frequency can be identified from the scalar temporal power spectra and the results are given in Figure 5.6. The straight channel and the channel with cavities have the same trend while the values for the channel with cavities are a little bit smaller than those of straight channel for most cases. The frequency for the channel with steps is much higher than the other two.

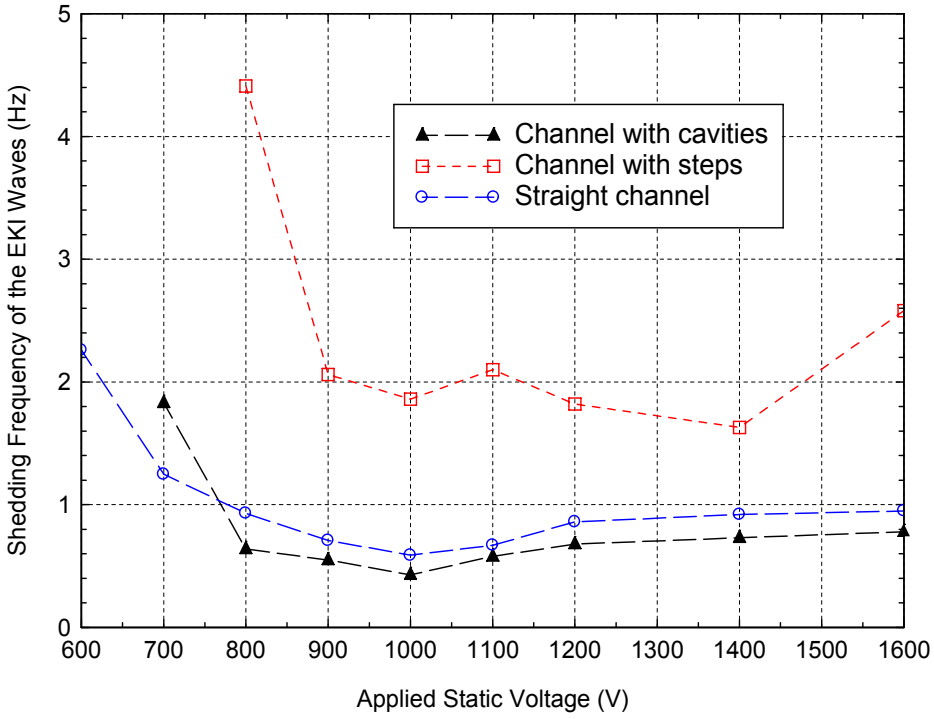

Figure 5.6. The frequency of electrokinetic instability Vs the static electric field

By increasing the strength of the applied static voltage, additional smaller EKI waves are found to be generated in the braid regions of the large convective EKI waves. The smaller EKI waves seem to propagate upstream instead of downstream. As the applied static voltage becomes higher than 1600V, the fluid mixing process in the microchannels was found to become much more turbulent and chaotic. The scalar temporal power spectra based on the time sequence of the fluorescence images were found to become continuous energy spectra, and no obvious peak can be identified.

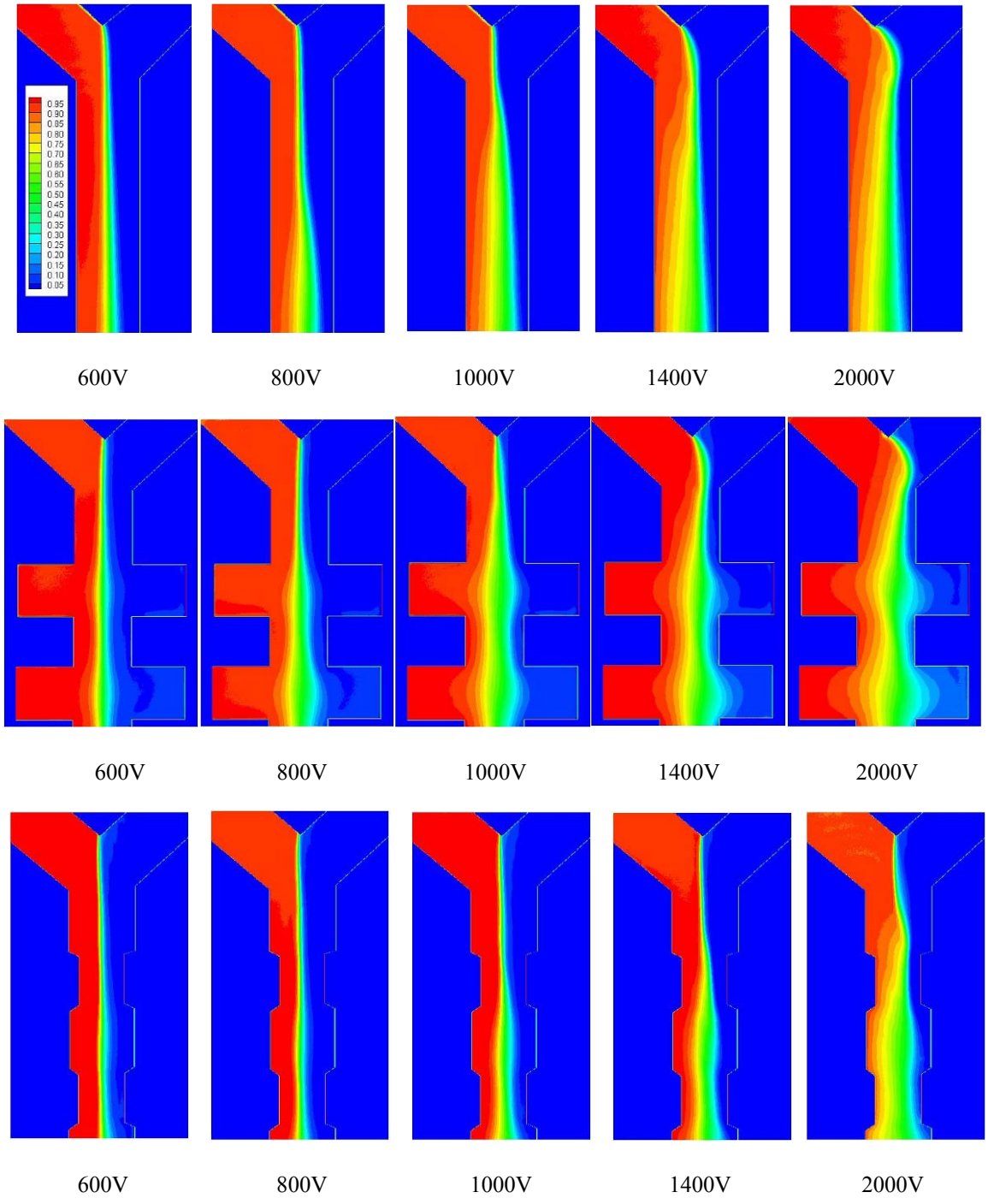

Figure 5.7. The ensemble averaged concentration fields of the Y-shaped microchannels under different strengths of the applied static electric field.

The ensemble averaged concentration fields of the Y-shaped microchannels under different static electric fields are shown in Figure 5.7. As the strength of the applied electric field increases, the influence area of the perturbations widens across the channels and also moves upstream till the conjunction part of the channels.

The effect of the strength of applied static electric field on the mixing process of the microchannels can be quantified by calculating the mixing efficiency in the region of interest and the results are shown in Figure 5.8. The mixing efficiency curves follow the same trend. As the strength of the static electric field becomes higher, the mixing efficiency curves keep increasing because of the more input of the electric energy. The channel with steps has relatively smaller values. According to the study of Kang et al [53], a stronger and highly nonuniform electric field is created near the edge of the blocks inside the microchannel with a step. The dieletrophoretic force generated by this nonuniform electric field repels small dielectric particles away from the surface of the blocks. For our present study, highly nonuniform electric field is inevitable due to the step structure. So even though the Rodanmine B molecules are small in size, such force might still exit and cause the flows propagate downstream without mixing efficiently. As the strength of the static electric field is low, the mixing efficiency of the straight channel is higher than that of the channel with cavities, which is due to that channel with cavities needs higher strength of the static electric field to induce the EKI waves than the straight channel. However, when the applied static electric field is higher than 1250V, the mixing efficiency of the channel with cavities becomes higher than the straight one. There might be two reasons for such better mixing.

One is the vortices generated near the corners of the concave structures. And the other is that the concave structures give the two adjacent streams larger area to diffuse.

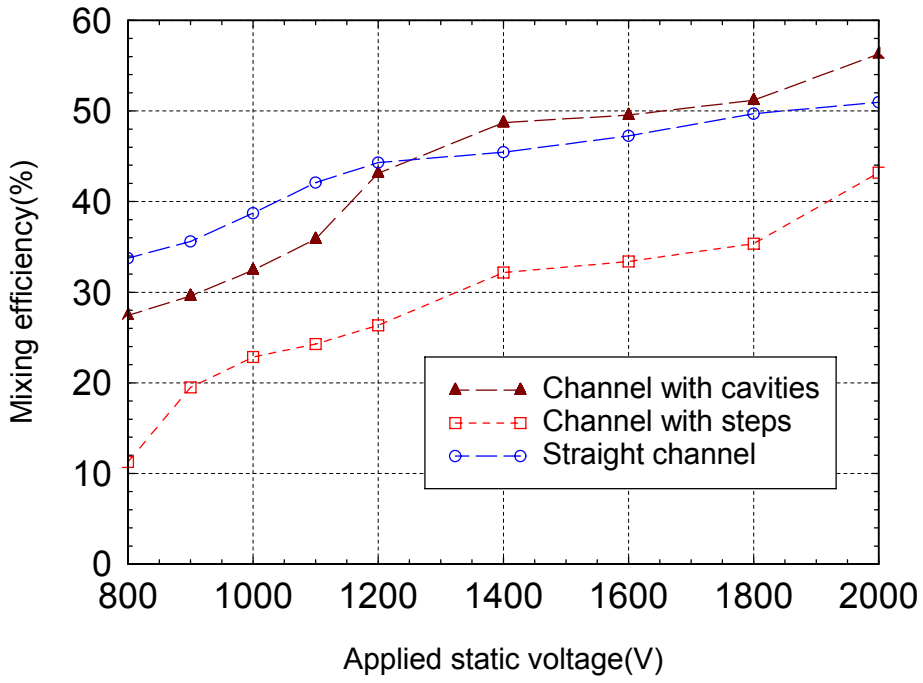

Figure 5.8. The mixed efficiency Vs the static electric field

5.3.3. The effect of alternative electric perturbations on the mixing enhancement

A parametric study was conducted to explore the effectiveness of using alternative electric fields to manipulate the convective EKI waves to further enhance fluid mixing in the Y-shaped microchannels. During the experiments, 1000V static voltage is applied to reservoir R-B while the sum of a static electric field and an alternative electric field is applied to inlet reservoir R-A which is defined by:

$$V = 1000V + V_{AC}\sin(2\pi ft) \qquad (5.1)$$

where V_{AC} is the magnitude of the alternating electric field imposed on the static electric potential and f is the frequency of the external electric field. By changing the magnitude and frequency of the alternative electric field, the effects of the applied alterative electric field on the evolution of the convective EKI waves and fluid mixing enhancement in the microchannels are assessed.

5.3.3a. The effect of the frequency of alternative electric perturbations

To study the effect of the frequency of alternative electric perturbation on the mixing enhancement in the Y-shaped microchannels, the magnitude of the AC is chosen to be 250V while the frequency is changed from 0.1 to 100. The interrogation region for calculating the mixing efficiency is the same as that mentioned before.

The relationship between the mixing augmentation factor and the frequency of the alternative electric field is shown in Figure 5.9. The natural frequency for the straight channel, channel with cavities and channel with steps under static electric 1000V only can be obtained from Figure 5.6, which is 0.6, 0.43 and 1.9, respectively. As increasing the frequency, for the channel with cavities and straight channel, mixing efficiency reaches its highest point when the imposed frequency of external force is the same as the natural frequency of the system.

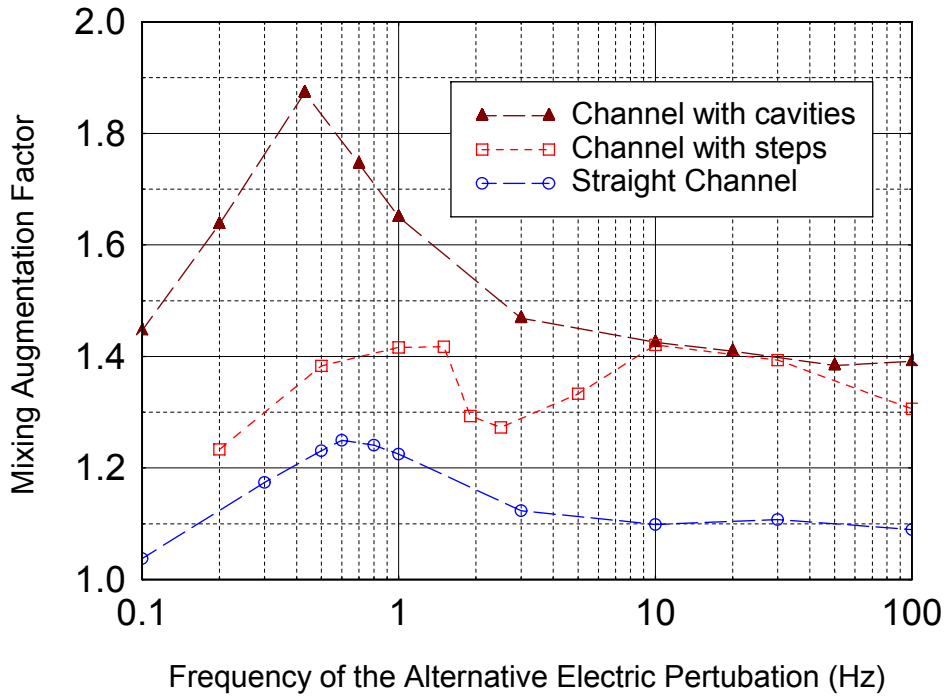

Figure 5.9. The frequency of the alternative electric perturbation Vs mixing augmentation factor

For both straight channel and channel with cavities, the mixing efficiency does not vary much when the frequency is larger than 10. However, for the channel with steps, this optimum frequency phenomenon is difficult to identify. The mixing frequency has relatively high values when frequency is near 1 and 10. It also should be noted that the channel with cavities has higher mixing augmentation factors than the other two channels. Since for all the microchannels, the mixing augmentation factors are greater than 1, which means that the alternative perturbations do enhance the mixing processes in the microchannels.

5.3.3b. The effect of the amplitude of the alternative electric perturbation

As described above, the fluid mixing process was found to be most enhanced when the frequency of the applied alternative electric perturbation is close to the shedding frequency of the convective EKI waves for the straight channel and channel with cavities. Therefore, the frequency of the applied alternative electric perturbation was set to be 0.6 and 0.43 for the straight channel and channel with cavities. Although the channel with steps does not have that phenomenon, its natural frequency was still chosen as 5.9. During the experiment, the amplitude of the applied alternative electric perturbation was changed from 50V to 500V.

The ensemble averaged concentration fields of the Y-shaped microchannels by applying alternative perturbations with different frequencies are shown in Figure 5.10. The interfacial contact surface area of the two adjacent streams becomes larger and wider as we increase the amplitude of the alternative perturbations.

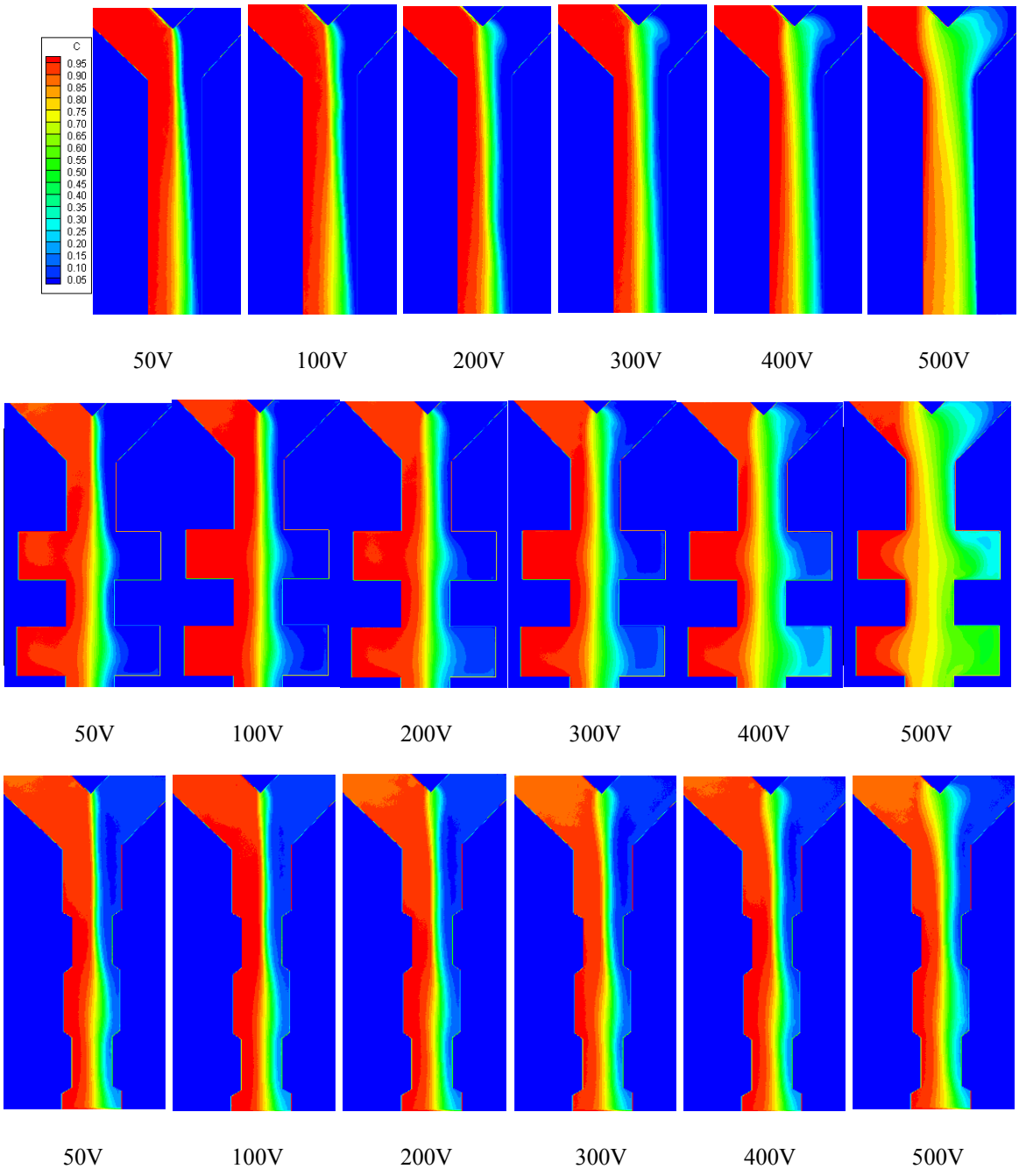

Figure 5.10. The ensemble averaged concentration fields of the Y-shaped microchannels by applying alternative perturbations with different amplitudes.

As shown in Figure 5.11, for all the microchannels, the mixing augmentation factors are greater than one which means that the alternative perturbations do enhance the mixing processes. Moreover, the mixing augmentation factors keep increasing with the increase of the magnitude of the alternative electric perturbation, which is resulted from the higher disturbance energy input. For the straight channel and channel with steps, their mixing augmentation factors are almost the same when the magnitude of the perturbation is relatively low (<300V). Meanwhile, the mixing augmentation factors of the channel with cavities increase at a higher rate than those of the other two channels.

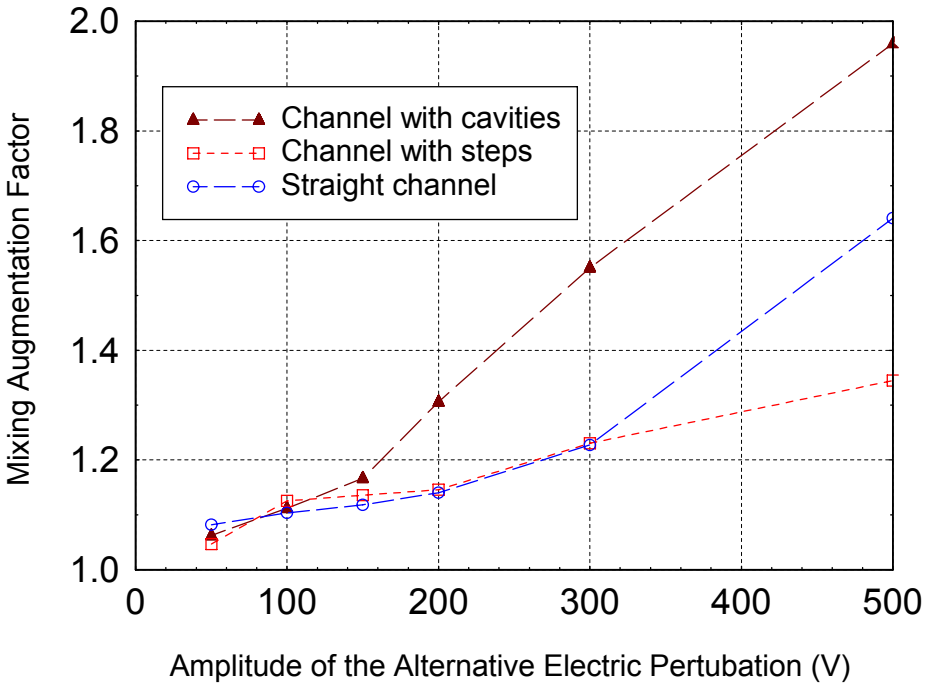

Figure 5.11. The magnitude of the alternative electric perturbation Vs mixing augmentation factor

CHAPTER 6: FLOW VELOCITY MEASUREMENT WITHIN SURFACE WATER DROPLETS

In this chapter, detailed information is provided on the flow field inside surface droplets on a test plate of different temperatures by using Particle Image Velocimetry (PIV) technique. To overcome the image distortion due to the refraction of light at the droplet surface, an image mapping method developed by Kang et al [33] was used (the details of which are shown in Appendix A). In addition, related parameters, such as contact angle and normalized droplet volume were also investigated.

6.1. Particle Image Velocimetry (PIV)

Particle Image Velocimetry (PIV) is an optical method used to measure velocities and related properties in fluids [55, 56]. The fluid is seeded with particles which, for the purposes of PIV, are generally assumed to faithfully follow the flow dynamics. It is the motion of these seeding particles that is used to calculate velocity information.

Typical PIV apparatus consists of a camera (normally a digital camera in modern systems), a high power laser, for example a double-pulsed Nd:YAG laser or a copper vapor laser, an optical arrangement to convert the laser output light to a light sheet (normally using a cylindrical lens), and the fluid/gas under investigation (see Figure6.1). The laser acts as a photographic flash for the digital camera, and the particles in the fluid scatter the light. It is this scattered light that is detected by the camera.

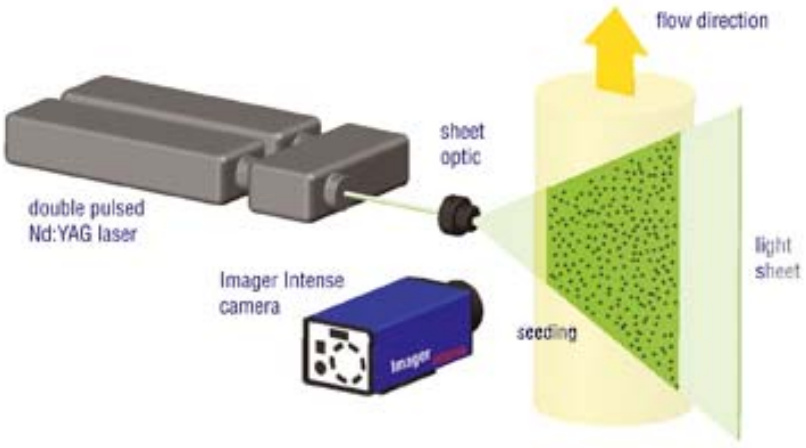

Figure 6.1. Schematics of a typical PIV setup.

In order to measure the fluid's velocity, at least two separate exposures must be recorded. This typically involves producing a pair of laser pulses which are recorded onto a pair of camera frames. The frames are next split in a large number of interrogation areas. It is then possible to calculate a displacement vector for each interrogation area with help of signal processing. This is converted to a velocity using the time between image exposures.

6.2. Experimental Setup

A droplet of 5.6μl (the diameter of which is about 2.9mm) was placed on a test plate by squeezing a syringe which was fastened on a holder (see Figure 6.2). The liquid tested in this investigation was DI water with fluorescent seeding particles inside (diameter 6μm, Duke Scientific Coop.). The number density of the particles in the solution was about $1.5\times10^{4}\,\mu l^{-1}$. The test plate was placed on the top of a circulator (Neslab, Rte-211 w/c), which had a mixture of antifreeze and coolant (PEAK Global Life Time) as the running fluid. In order to

prevent disturbance from air flows in the room on the evaporation process of the droplet, a plexiglass chamber was designed and placed outside the test plate.

A 532nm laser beam from a Nd:YAG laser (New Wave) passed through an optical slit and generated an approximately 600μm wide laser sheet. The laser sheet illuminated the middle plane of the droplet. A cooled CCD camera (SensiCam, Cooke) was used to capture the particle images (The laser and camera synchronization setup for PIV is shown in Appendix B). The depth of focus of the lens (AF MICRO NIKKRR 105mm, Nikon) attached to the camera was about 1 mm.

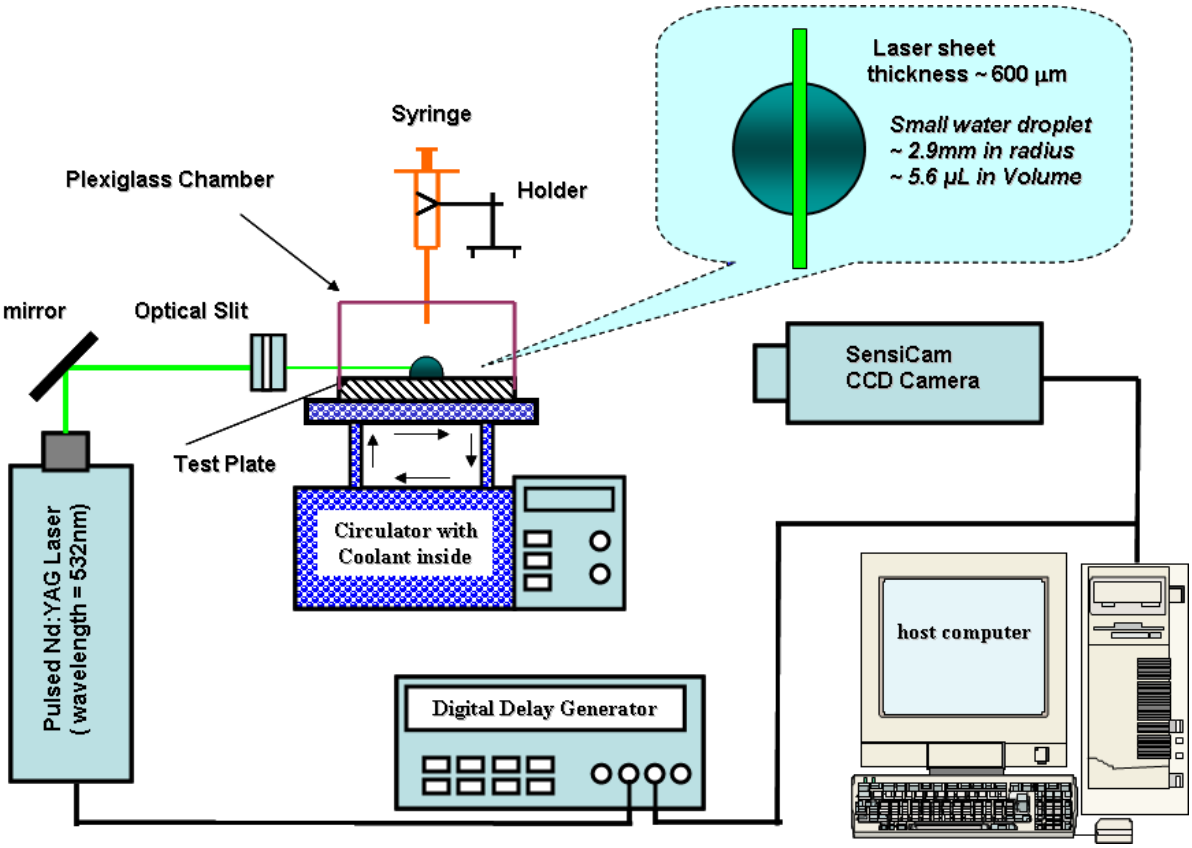

Figure 6.2. The experimental setup

6.3. Results and Discussions

6.3.1. Images of surface droplets

Figure 6.3 - 6.7 show the average images of the surface droplets on a test plate under different temperatures. Since these images are the averages of 10 actual PIV images, particle trajectories are formed in some of them. When the test plate temperature is at room temperature, 21.9°C, the droplet evaporates with a constant contact radius and a reducing contact angle. Vortices begin to from right after the droplet arrives on the plate and then becomes more apparent as time went by. However, 20 minutes later such vortices can no longer be noticed and flow moves at a slow speed while the florescence particles begin falling down to the bottom of the droplet. Eventually, the evaporation results in a droplet with very small contact angle. Only a few particles are left in the middle region of the droplet and they are moving very slowly. The curvature change of the droplet causes a signification distortion which forms a very bright region on the droplet image.

When the test plate temperature is 0.0°C, the droplet contact angle does not decrease. The vortices inside the droplet still become less and less recognizable with time and in the end only irrational flow movements are found inside droplet. The erratic movements of the fluid might be explained by the fact of water condensation on the test plate. The thin water film formed by such condensation merges with the droplet and causes the change of the shape of the droplet (see Figure 6.6), which makes it not a sphere cap anymore. This irregular shape produces complicated surface tension which might result in complex flow movement inside

the droplet. As for the cases of 15.0°C, 10.0°C, and 5.0°C, the flow pattern change happens in some way between these two cases.

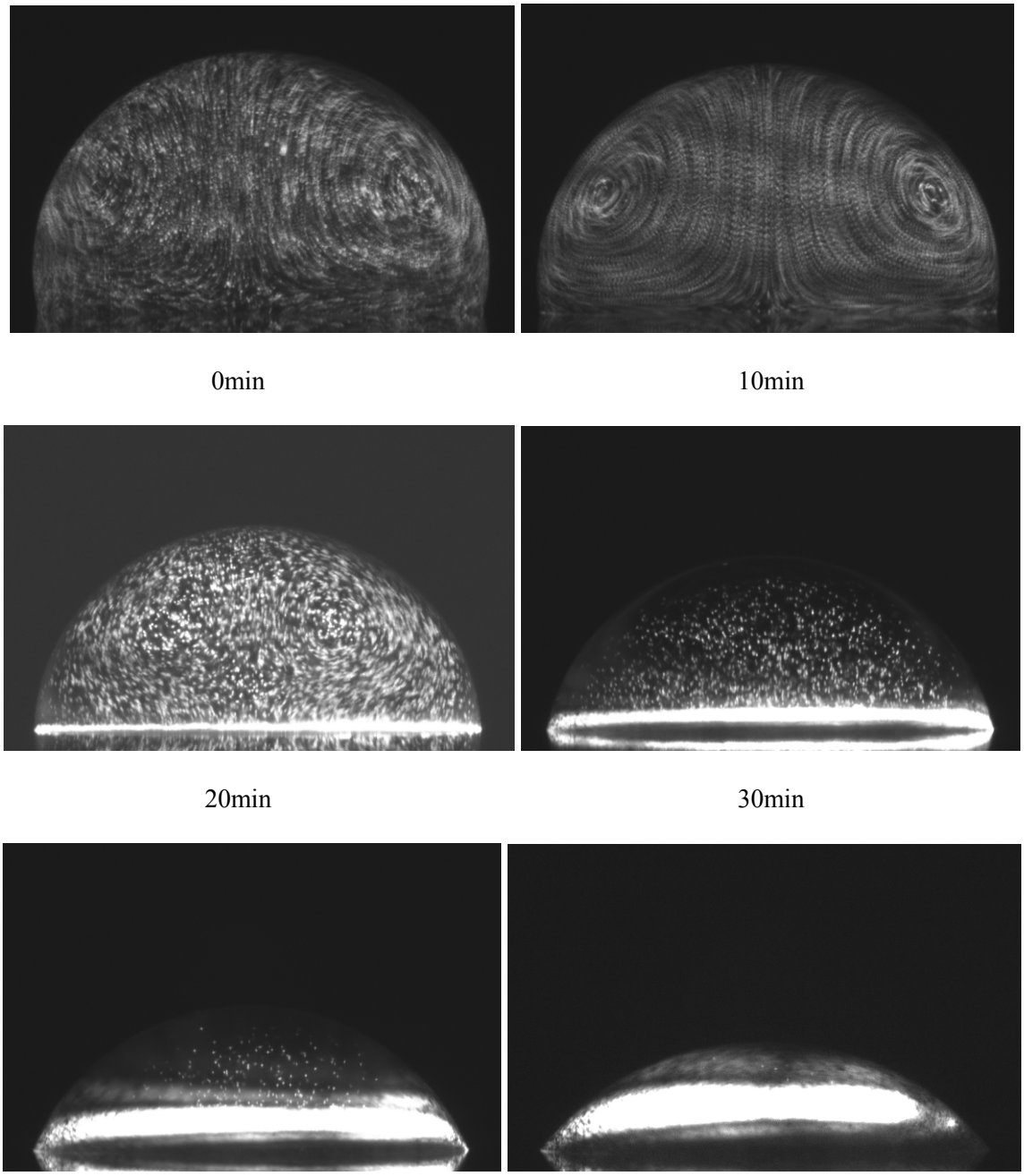

Figure 6.3. Images of droplet with time when test plate temperature is 21.9°C

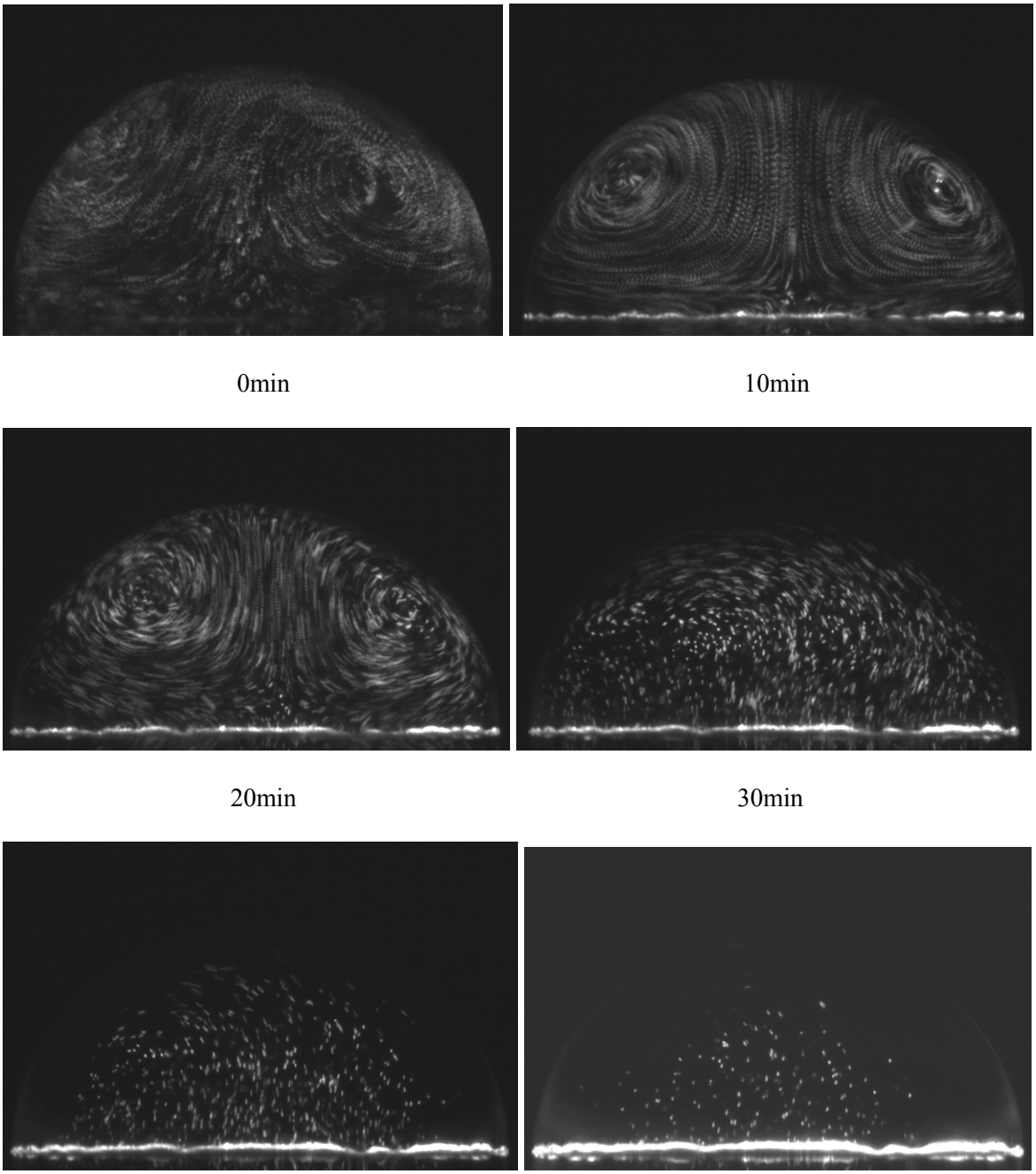

0min 10min

20min 30min

40min 50min

Figure 6.4. Images of droplet with time when test plate temperature is 15.0°C

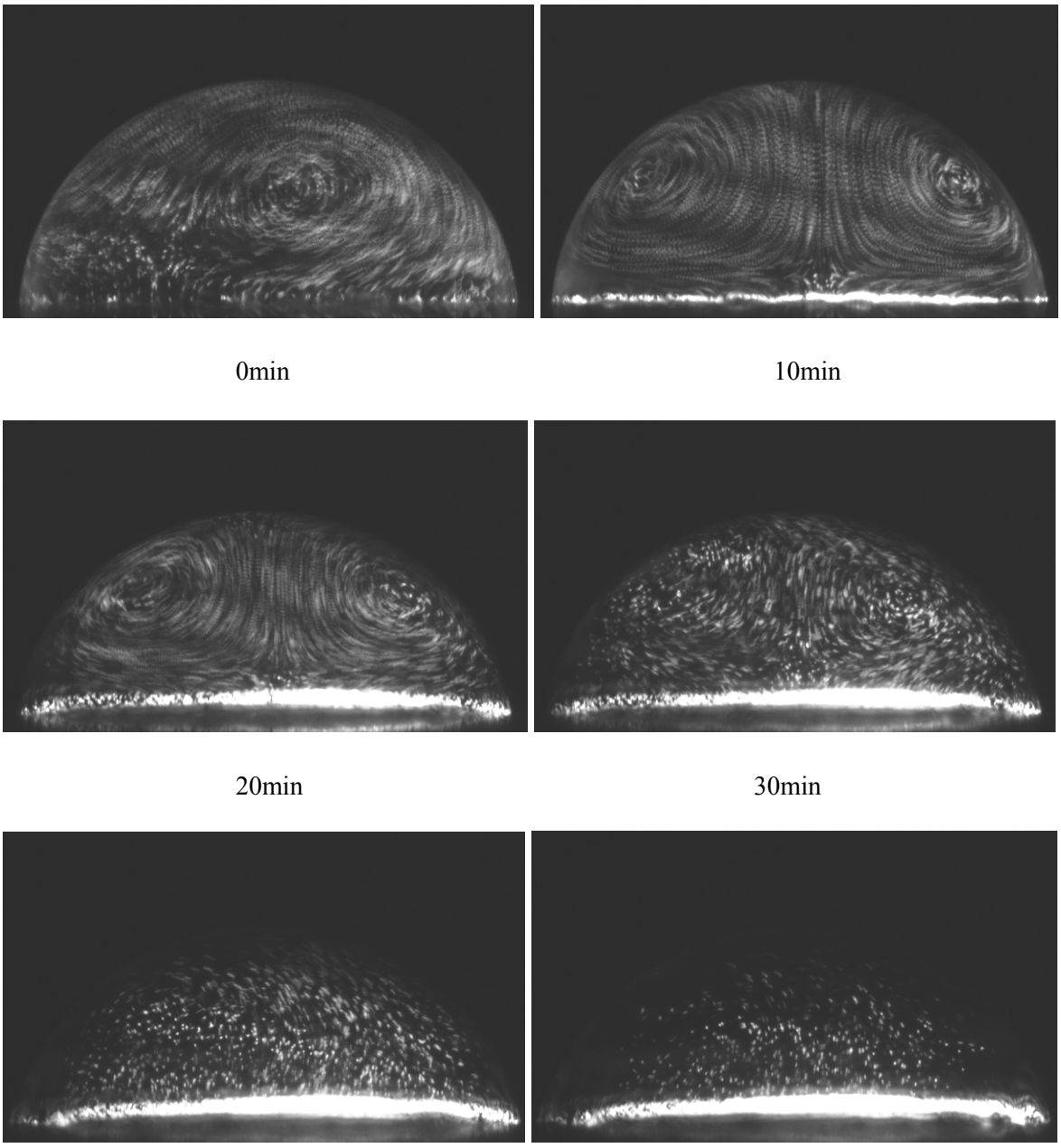

0min 10min

20min 30min

40min 50min

Figure 6.5. Images of droplet with time when test plate temperature is 10.0°C

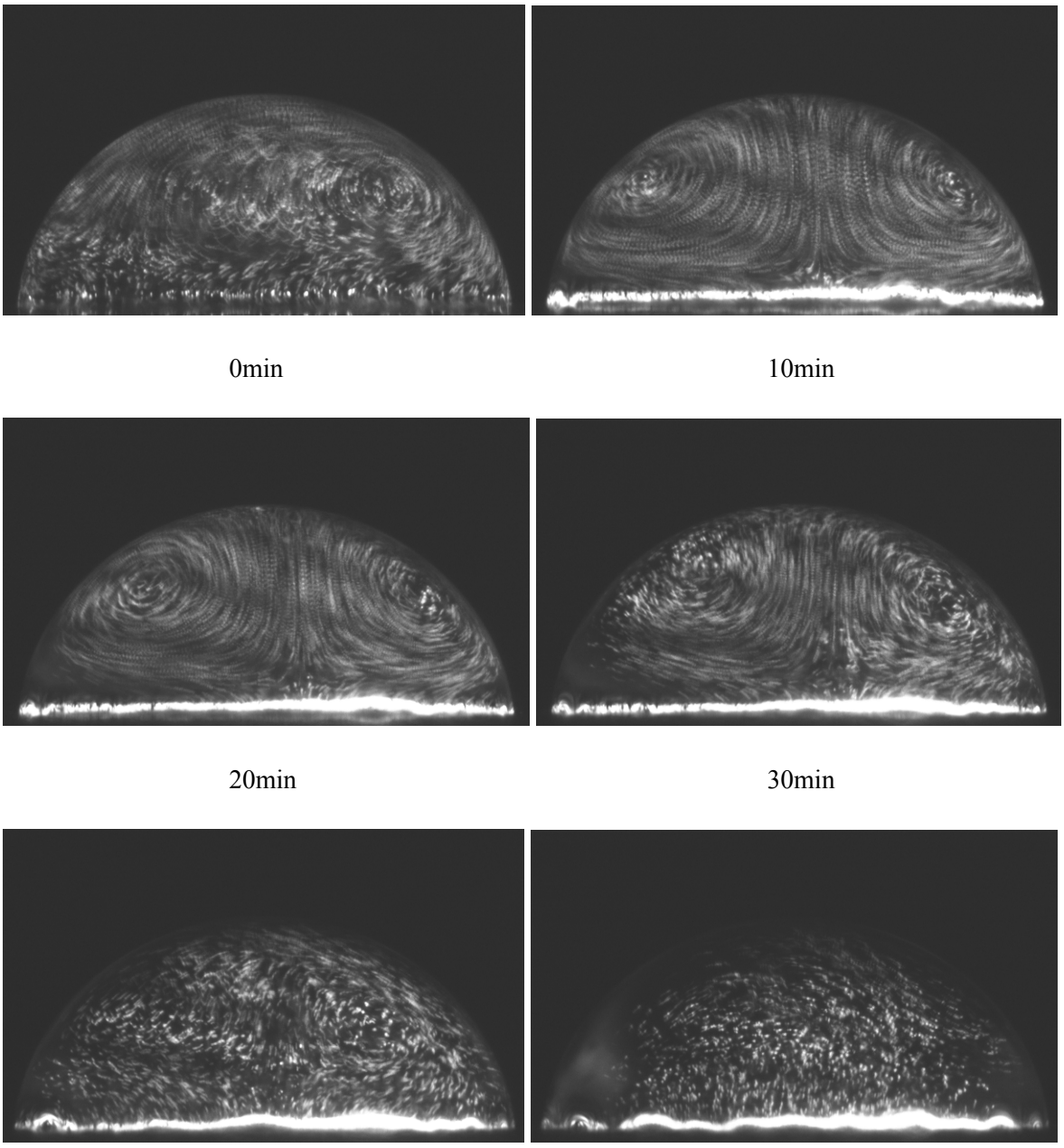

0min 10min

20min 30min

40min 50min

Figure 6.6. Images of droplet with time when test plate temperature is 5.0°C

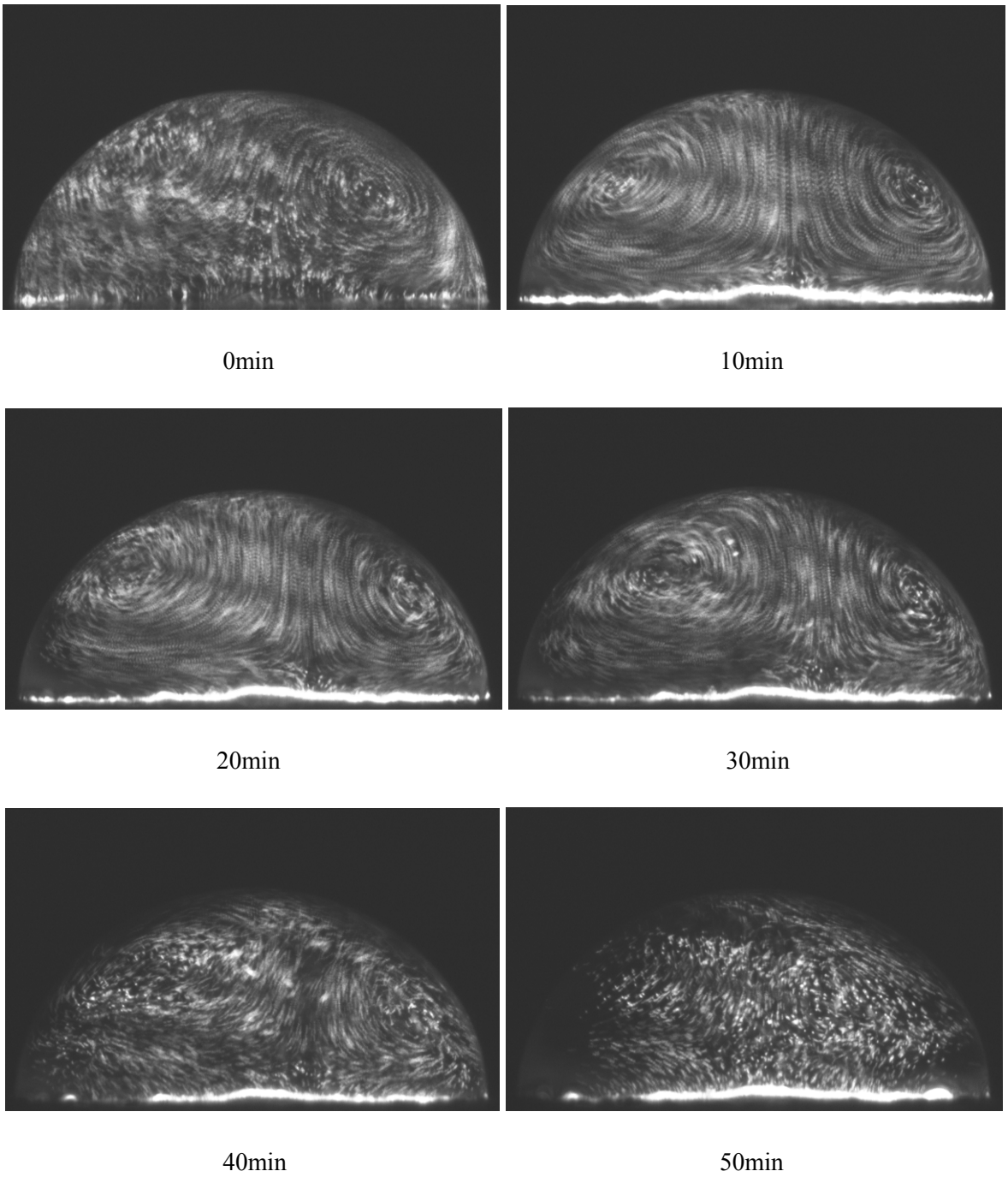

Figure 6.7. Images of droplet with time when test plate temperature is 0.0°C

6.3.2. The change of evaporation and contact angle

Figure 6.8 shows drawings and equations for the calculations of contact angle θ, contact area S_g and volume V using the size of droplets (x and y in the drawing). It is assumed here that the concave outline of the droplet is a part of a sphere [57].

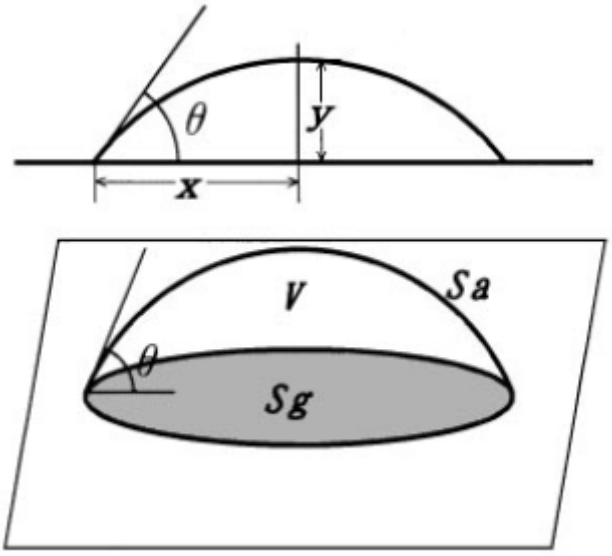

Figure 6.8. Measurement and calculation of droplet size

$$\theta = 2 * \tan^{-1}(\frac{y}{x}) \tag{6.1}$$

$$S_g = \pi x^2 \tag{6.2}$$

$$V = \frac{\pi x^3 (1-\cos\vartheta)^2 (2+\cos\theta)}{3\sin^3\theta} \tag{6.3}$$

Since the droplets were squeezed onto the test plates, their sizes were not necessarily the same for each case. In order to eliminate the effect of such differences on current evaporation study, a factor named normalized droplet volume, V_N, is introduced. It is decided by the

actual volume of droplets with time and their initial volume. Thus, evaporation processes between them can be compared by this normalized number:

$$V_N = \frac{V}{V_0} \tag{6.4}$$

The relationship between normalized droplet volume and time is shown below in Figure 6.9. When the plate temperature is 21.9°C, the fast evaporation of the droplet causes it to decrease lineally to about 62% of its initial size after 20 minutes. However, once the plate temperature drops to 15°C, the evaporation process happens at a much lower rate which results in a droplet 90% of its initial size at 20 minutes later. When the plate temperature is 10°C, there is little evaporation and the droplet size keeps constant. This phenomenon can be explained by the fact that the cool test plate condenses the water vapor in the air and the new water added to the droplet just balances off the part that is evaporated. As the temperature of test plate decreases to 5°C, the condensation process becomes even more prominent and it actually enlarges the size of the droplet gradually. When the plate temperature is 0°C, the size of the droplet increases more rapidly and reaches a point of a 5% increase over its initial value at 20 minutes later.

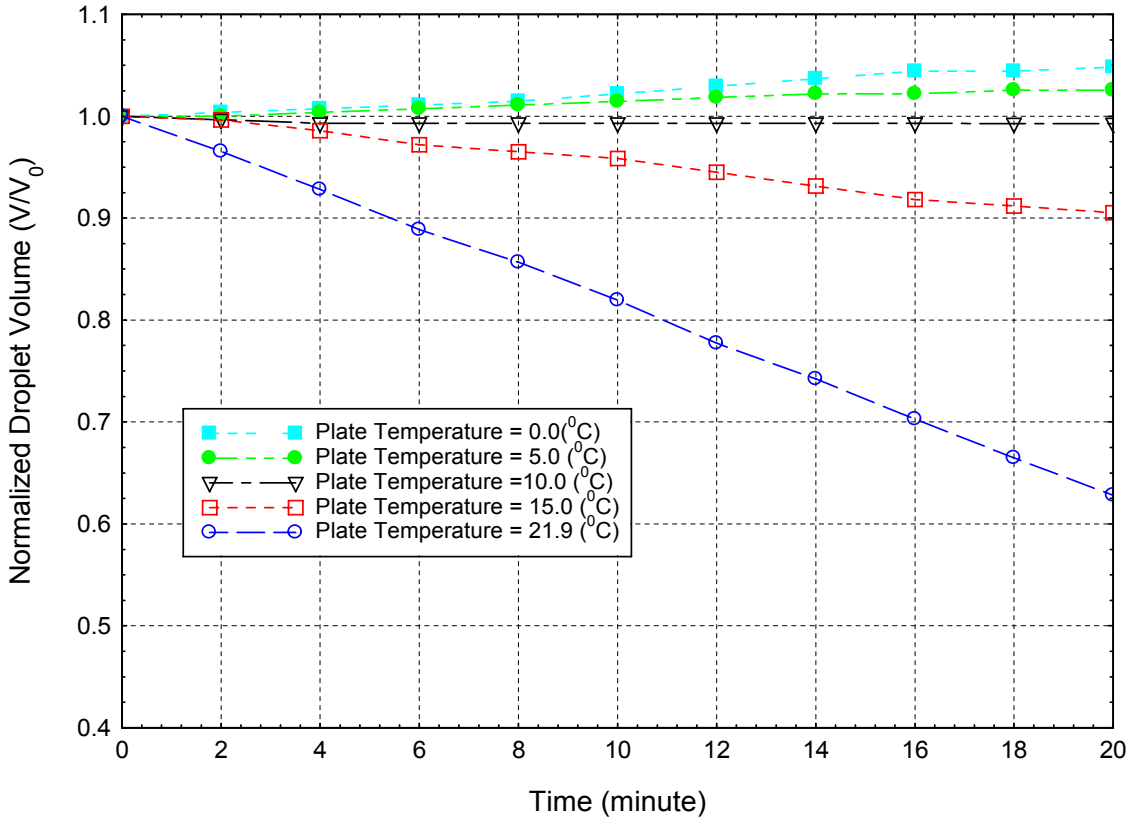

Figure 6.9. Normalized droplet volume vs time.

Figure 6.10 shows the change of contact angle of droplets with time. When the plate temperature is 21.9°C, the contact angle reduces rapidly from 99° to 81°, which is due to the fast evaporation process. As the plate temperature reduces to 15°C, the contact angle decreases almost linearly at a much lower rate. When the plate temperature is 10°C, the contact angle keeps constant during the first 14 minutes and then decreases lineally at a slight rate. As the temperature of test plate decreases to 5°C and 0°C, the condensation process becomes even more prominent and it enlarges its contact angle gradually.

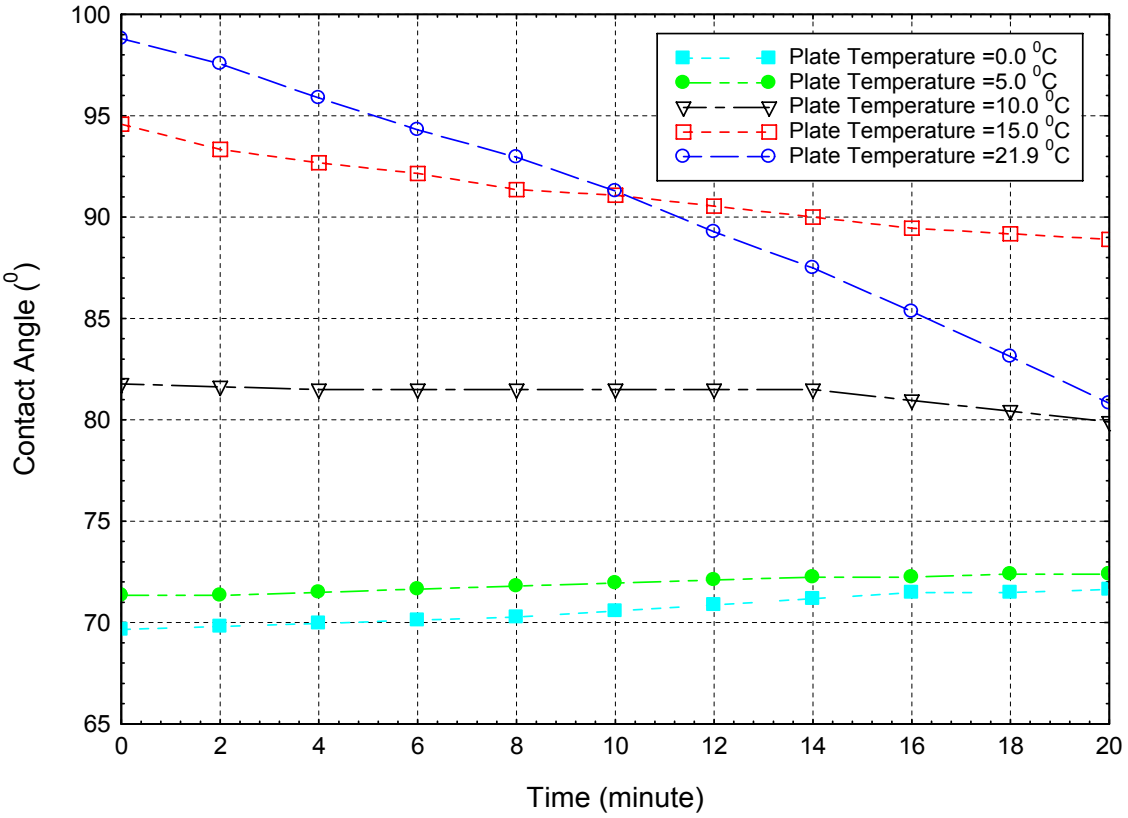

Figure 6.10. Contact angle vs time.

6.3.3. The velocity measurement

The two-frame cross-correlation PIV method was employed to obtain the velocity vectors in the middle plane of the droplets [55, 56]. The interrogation window had a size of 32 × 32 pixels and overlapped 50%. The instantaneous velocity fields of the droplets (4 minutes after they were placed on the plate) are shown in Figures 6.11-6.15.

When conducting PIV measurements on surface droplets, the refraction of light at the droplet surface caused a significant image distortion problem. For instance, Figures 6.11a shows a strong upward flow in the centre region and a relatively weak downward flow at the boundary region of the droplet. With the velocity vectors alone, the continuity requirement

appears to be violated. This results form the distortion of particle images due to the lens effect of the droplet itself. Thus, it becomes obvious why the flow field should be corrected.

In Figures 6.11-6.15, the red arc represents the edge of the surface droplets for each case. Due to the limitation of the image mapping restoration method, the centre region of the droplet is well restored, while the accuracy of image restoration is not so good in the outer region. Only about 75% of the original region can be seen in the restored ones. In the meanwhile, the vortices are placed more towards the middle of the droplets in the restored velocity fields.

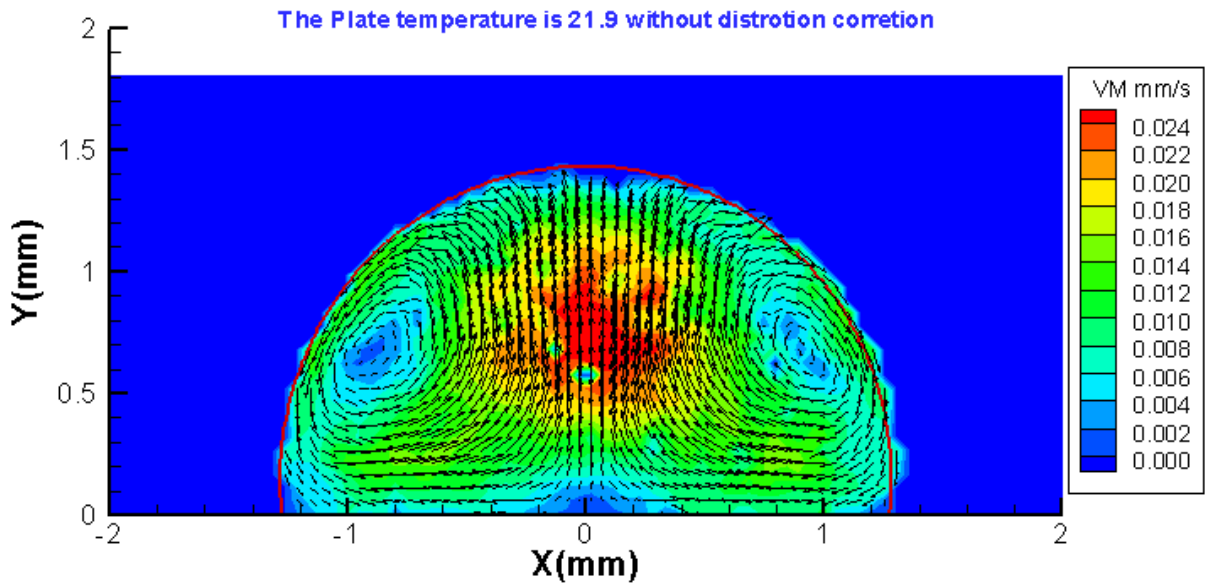

a. without distortion correction

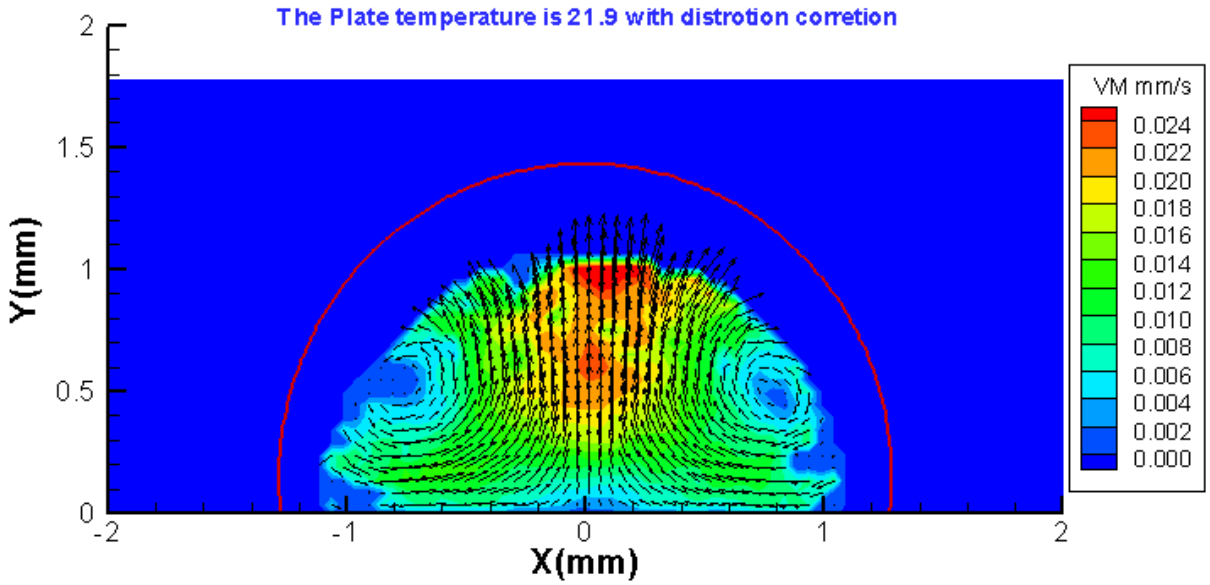

b. with distortion correction

Figure 6.11. Instantaneous velocity distribution when the plate temperature is 21.9°C.

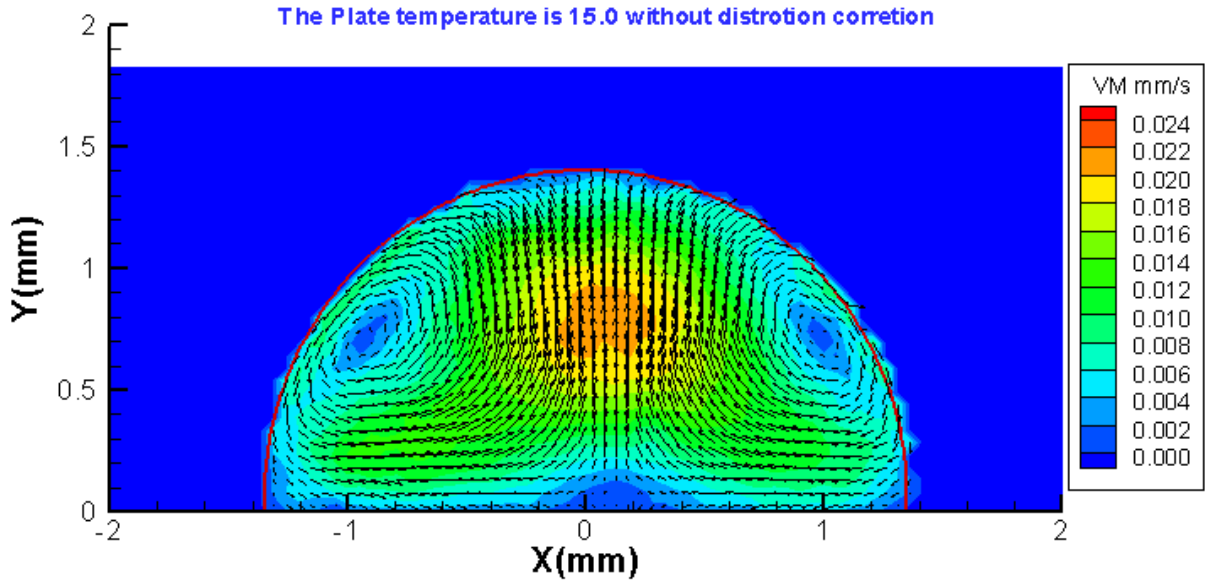

a. without distortion correction

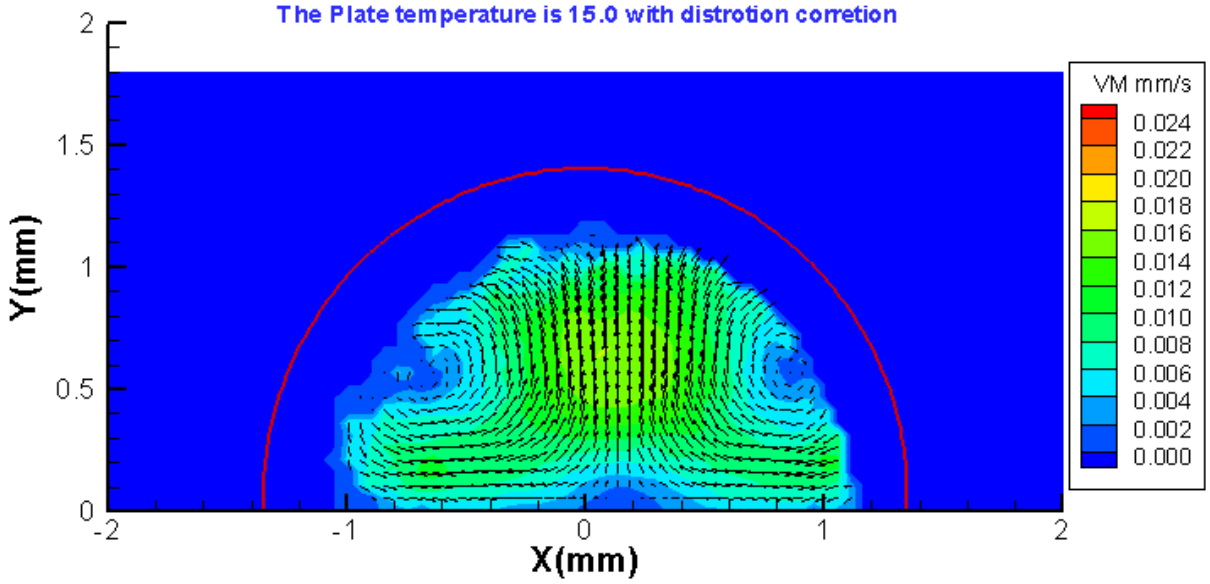

b. with distortion correction

Figure 6.12. Instantaneous velocity distribution 4 minutes later when the plate temperature is 15.0°C.

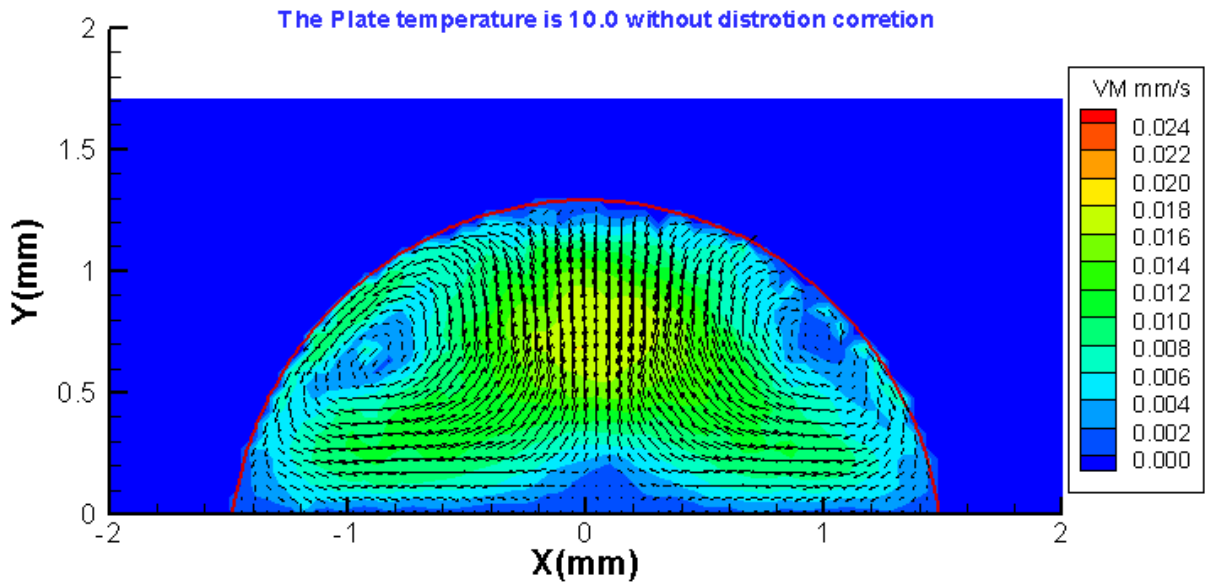

a. without distortion correction

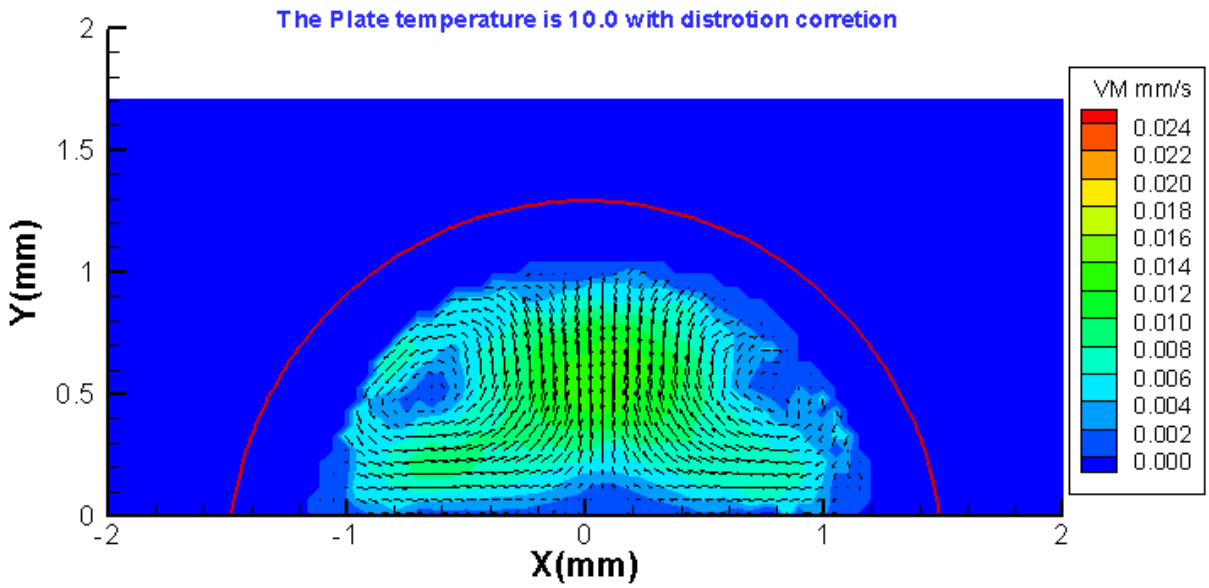

b. with distortion correction

Figure 6.13. Instantaneous velocity distribution 4 minutes later when the plate temperature is 10.0°C.

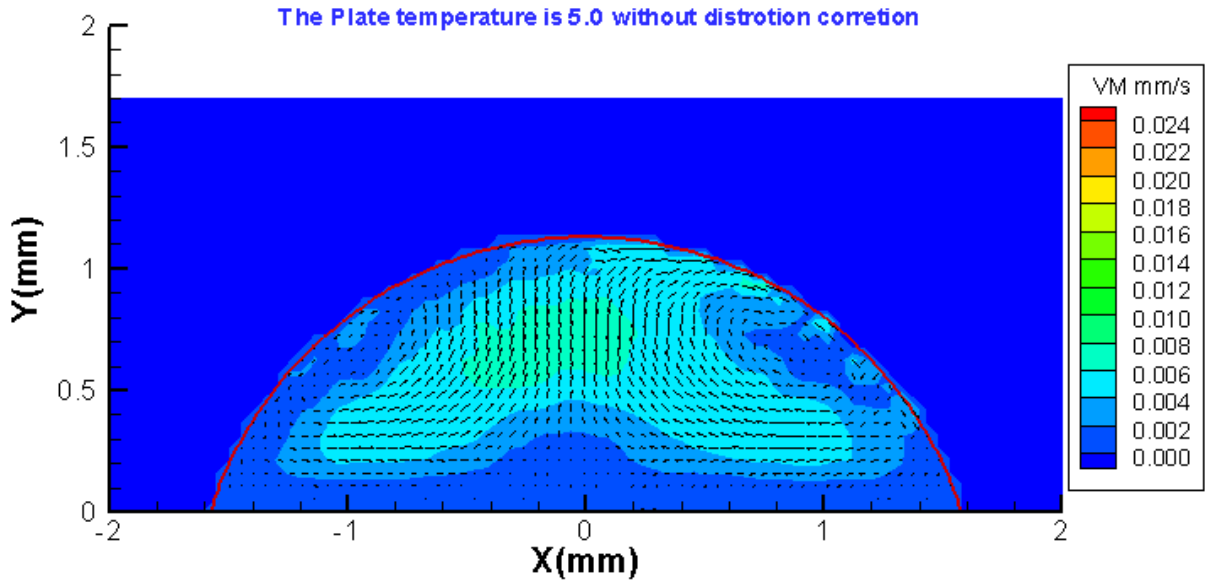

a. without distortion correction

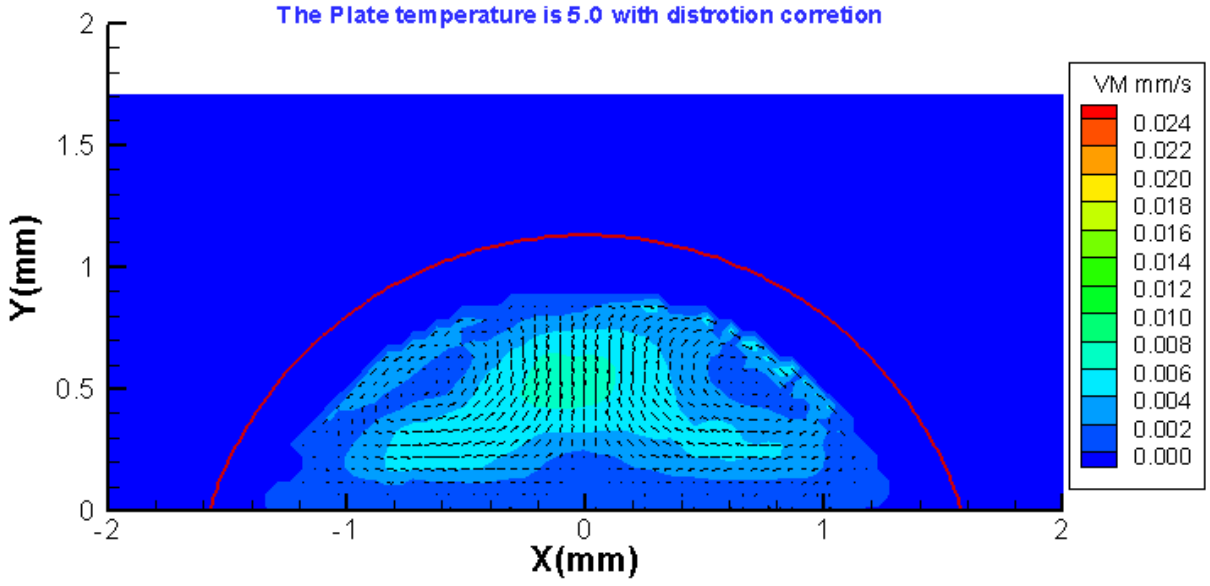

b. with distortion correction

Figure 6.14. Instantaneous velocity distribution 4 minutes later when the plate temperature is 5.0°C.

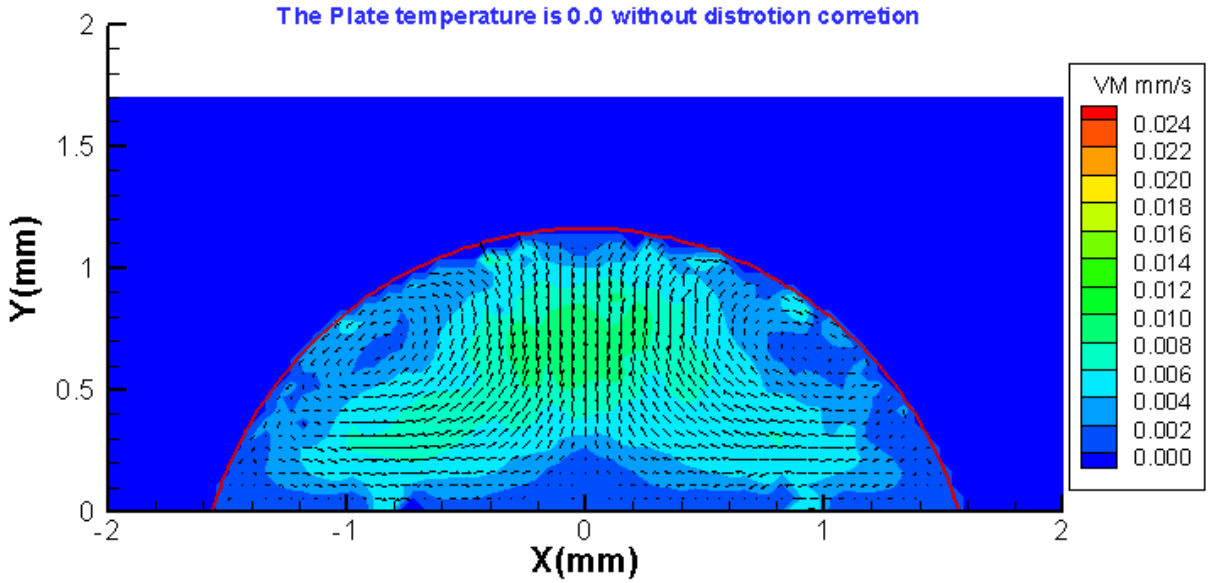

a. without distortion correction

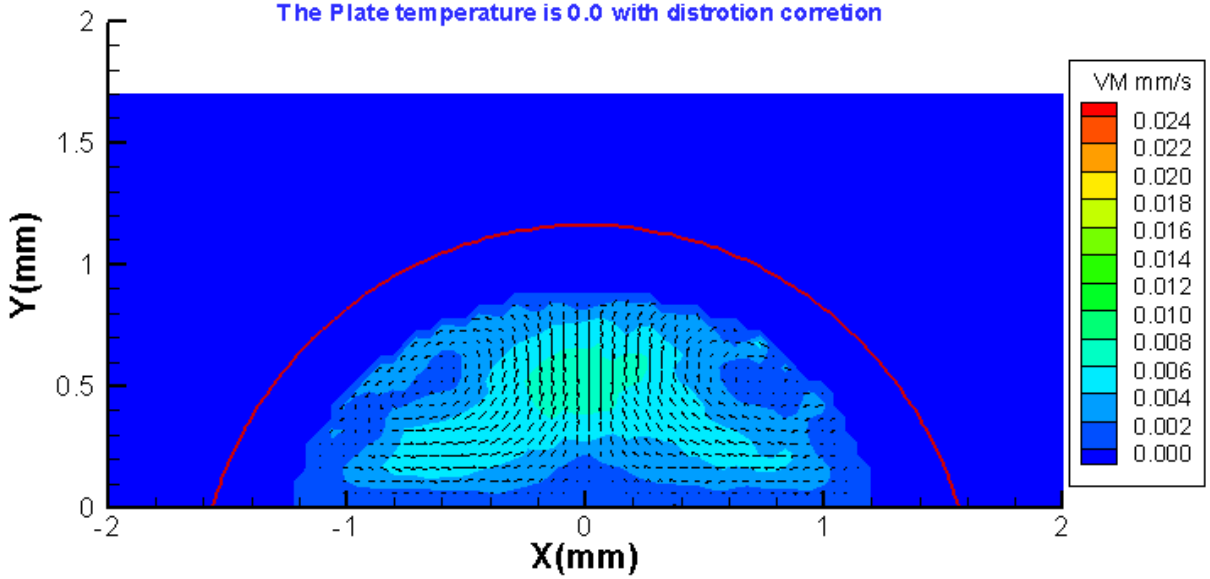

b. without distortion correction

Figure 6.15. Instantaneous velocity distribution 4 minutes later when the plate temperature is 0.0°C.

To illustrate the effect of the plate temperature on the velocity distribution inside the droplets, a point (x=0mm, y=0.5mm) was selected and the instantaneous upward velocity (after image restoration) at that location is shown Figure 6.16. The results were actually starting from 4 minutes after the droplets arrived on the test plate. The velocity for the case of room temperature remains the highest which is about 0.018mm/s. As the temperature of the plate drops, velocity also decreases which is due to the cooling down process from the cold plate. However, for the cases of 5.0°C and 0.0°C, the velocity curves are almost the same.

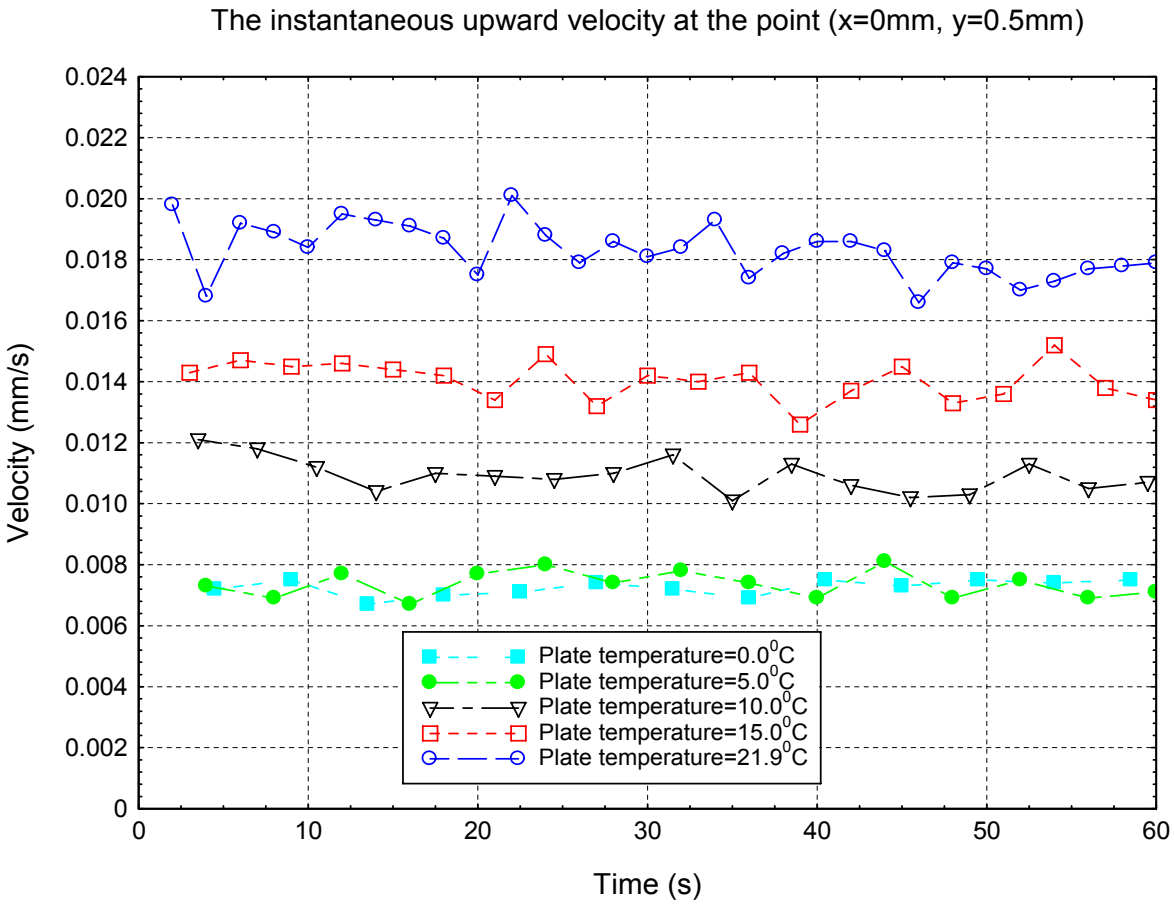

Figure 6.16. The instantaneous upward velocity at the point (x=0mm, y=0.5mm), starting from 4 minutes after the droplets' arrival on the test plate.

According to the study by Ristenpart et al [41], if the substrate and liquid conductivity ratio k_R is greater than 2, the consequent Marangoni flow is directed radially outward along the substrate (as seen in Figure 6.17b). Since the test plate used in present study was made of brass, the thermal conductivity of brass is 109 W/mK, while the thermal conductivity of water is 0.58 W/mK. By assuming the change of thermal conductivity of water due to the addition of florescence particles was negligible, the ratio was estimated to be about 187, which meant the flow pattern should follow Figure 6.17b if it was induced by the thermal Marangoni effect. However, the actual flow pattern was contrary to that, as shown in Figure 6.17a.

Stowell and Korgel [39] conducted surface tension measurement of chloroform solvent in which 3.5 and 5nm gold nanocrystals were dispersed. The surface tension of the solvent was found to increase with increasing particle concentration for both particle sizes. The increase in surface tension with increased concentration was presumably resulted from the much lower volatility of the nanocrystals relative to the solvent. Their discovery might help explain the possible reason for the present flow pattern. Even though the particles were premixed well with water before the experiments, they tended to sink toward the test plate due to gravity (the density of the particles is 1.05 g/cm^3), which caused the particle concentration in the lower part higher than that of the upper part. Because the surface tension of the solvent increased with increasing particle concentration, the high surface tension pulled more strongly on the surrounding liquid than one with a low surface tension. The presence of a gradient in surface tension caused the liquid to flow away from regions of low surface tension and formed a flow pattern as shown in Figure 6.17a.

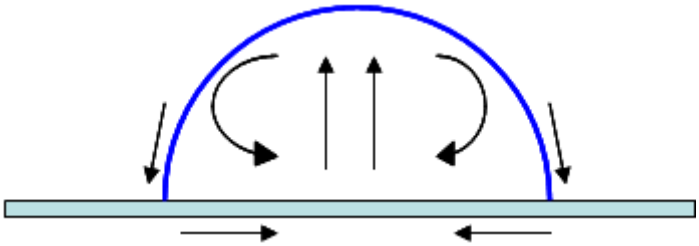

a. The present flow pattern

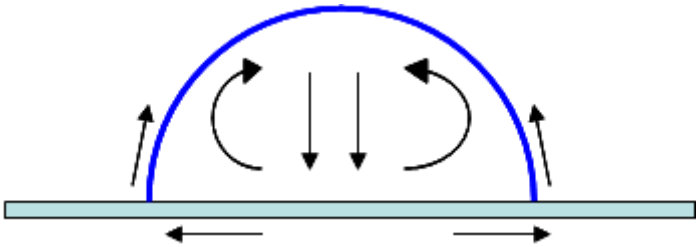

b. The theoretical thermal Marangoni flow pattern

Figure 6.17. Comparison of present flow pattern and theoretical thermal Marangoni flow pattern

The above explanation about the cause of the present flow pattern inside surface droplets is only a tentative assumption. To figure out the exact reason for this phenomenon, more research work is suggested to be done in the future.

CHAPTER 7: TRANSIENT TEMPERATURE MEASUREMENTS OF SURFACE WATER DROPLETS

In this chapter, the feasibility and implementation of the lifetime-based Molecular Tagging Thermometry (MTT) technique are demonstrated by conducting measurement of spatially-and-temporally-resolved temperature distribution within a convectively-cooled, micro-sized, water droplet over an aluminum test plate.

7.1. Fluorescence and phosphorescence for temperature measurements

It is well known that both fluorescence and phosphorescence are molecular photoluminescence phenomena [58]. Compared with fluorescence, which typically has a lifetime on the order of nanoseconds, phosphorescence can last as long as microseconds, or even minutes. Since emission intensity of photoluminescence is a function of the temperature for some substances, both fluorescence and phosphorescence of tracer molecules may be used for temperature measurements.

According to Beer's Law for low concentration of the tracer molecules and unsaturated laser excitation [58], photoluminescence intensity, I_p, (both fluorescence and phosphorescence) can be expressed by following equation;

$$I_p = A I_i C \varepsilon \Phi , \qquad (7.1)$$

where I_i is the local incident laser intensity, C the concentration of tracer molecules, ε the absorption coefficient, and Φ the quantum efficiency. A is the fraction of the photoluminescence emission collected by a CCD detector.

7.1.1. LIF-based techniques for droplet temperature measurements

Laser-induced fluorescence (LIF) techniques have been widely used for temperature measurements of liquid droplets for combustion applications [59-60]. For some fluorescent molecules, such as Rhodamine B, the absorption coefficient and quantum efficiency are temperature dependent. Therefore, in principle, fluorescence intensity may be considered to depend only on temperature as long as the incident laser excitation is uniform and the concentration of the tracer molecules remains constant in the measurement region. In practice, however, it is very difficult, if not impossible, to ensure a temporally-and-spatially non-varying incident laser excitation or/and uniform molecular tracer concentration in the measurement region for heat transfer studies due to the temperature dependence of the index of refraction for the work fluid. The issue could become much more serious for the transient temperature measurements within small water droplets over solid surfaces since the curved droplet surfaces would cause tremendous variation of laser illumination (i.e., refraction, reflection and scattering) in the measurement domain. Photobleaching effect may also become significant due to the small size of the water droplets. Such issues may cause significant errors in the droplet temperature measurement.

In order to decouple the effects of the non-uniformity of incident laser illumination and the molecular tracer concentration (due to photo bleaching) on fluid temperature measurement, several ratiometric LIF techniques have been developed recently [59-64]. The ratiometric LIF techniques developed for the temperature measurement of liquid droplets are usually called two-color LIF technique [59-60, 64]. The two-color LIF technique achieves temperature measurements by taking advantage of the differences in temperature sensitivity

of fluorescence emission at two different bands of the same fluorescent dye. After taking the ratio of the fluorescence emission intensity simultaneously collected at two different emission bands (i.e., two colors), the effects of the non-uniformity of incident laser illumination and concentration of the fluorescent tracer molecules on the droplet temperature measurements can be eliminated.

It should be noted that it usually requires two cameras with various mirrors, optical filters and lens in order to capture two fluorescence images at the same time to implement the two-color LIF method. It also requires a careful image registration or coordinate mapping procedure in order to establish a spatial correlation between the two acquired fluorescence images acquired by two difference cameras for the LIF intersity ratio calculation. The optical distortions due to the different mirrors, filters and lenses mounted in the fronts of different cameras can cause ambiguities to locate corresponding fluorescent molecules in the two acquired fluorescence images for the LIF intensity ratio calculation. This would result in uncertainties for the droplet temperature measurements.

By using LIF-based thermometry techniques, the total fluorescence intensity (integration of all of the fluorescence emission along time axis) is usually collected for the temperature measurement due to the short emission lifetime of fluorescence (on the order of nanoseconds). Based on the calibration curves of the collected fluorescence intensity (or intensity ratio) vs. temperature, the collected flourescence intensity (or intensity ratio) distributions are converted to fluid temperture distributions. Therefore, LIF-based techniques are actually *intensity-based* techniques for temperature measurement.

7.1.2. Lifetime-based techniques for droplet temperature measurements

Laser-induced phosphorescence (LIP) techniques have also been suggested recently to conduct temperature measurements of "in-flight" or levitated liquid droplets [65-66]. Compared with LIF techniques, the relatively long lifetime of phosphorescence could be used to prevent interference from scattered/reflected light and any fluorescence from other substances (such as from solid surfaces) that are present in the measurement area, by simply putting a small time delay between the laser excitation pulse and the starting time for phosphorescence image acquisitions. Furthermore, LIP was found to be three to four times more sensitive to temperature variation compared with LIF [65-66], which is favorable for the accurate measurements of small temperature differences within small liquid droplets.

The MTT technique described here is a LIP-based technique, which can be considered as an extension of the Molecular Tagging Velocimetry and Thermometry (MTV&T) technique developed by Hu & Koochesfahani [67]. Unlike most commonly-used LIF-based techniques that rely on information obtained from the "intensity axis" of the fluorescence emission process, the lifetime-based MTT technique described in the present study rely on the information contained in the "time axis" of the phosphorescence emission process, as temperature change would cause significant variation in the phosphorescence lifetime for some phosphorescent dyes. For MTT measurement, a pulsed laser is used to "tag" phosphorescent tracer molecules (e.g. phosphorescent dye) premixed in the working fluid. The long-lived LIP emission is imaged at two successive times after the same laser excitation pulse. The LIP emission lifetime distribution can be estimated from the intensity ratio of the acquired phosphorescence image pair. While the size of a small droplet can be determined

from the acquired phosphorescence images, the temperature distribution within the small water droplet can be derived by taking advantage of the temperature dependence of phosphorescence lifetime. It should be noted that both the present MTT measurement and the work of Omrame *et al*. [65-66] are based on a similar idea of achieving temperature measurement by taking advantage of temperature dependence of phosphorescence lifetime. The work of Omrame *et al*. [65-66] is only a single-point feasibility study using photomultiplier-based instrumetation. However, the present work is the planar temperature field measurement to achieve simultaneous measurements of droplet size and temporally-and-spatially resolved temperature distribution within a small water droplet based on direct imaging of phosphorescence lifetime with a conventional image detecting CCD camera.

The technical basis of the lifetime-based MTT measurements is given briefly at here. According to quantum theory, the intensity of phosphorescence emission decays exponentially [58]. As described in Hu *et al.* [67], for a dilute solution and unsaturated laser excitation, the collected phosphorescence signal (S) by using a gated imaging detector with integration starting at a delay time t_o after the laser pulse and a gate period of δt can be given by:

$$S = AI_i C\varepsilon\Phi_p \left(1 - e^{-\delta t/\tau}\right) e^{-t_o/\tau} \tag{7.2}$$

where A is a parameter representing the detection collection efficiency, I_i is the local incident laser intensity, C is the concentration of the phosphorescent dye (the tagged molecular tracer), ε is the absorption coefficient, and Φ_p is the phosphorescence quantum efficiency. The

emission lifetime τ refers to the time at which the intensity drops to 37% (i.e. 1/e) of the initial intensity.

In general, the absorption coefficient ε, quantum yield Φ_p, and the emission lifetime τ are temperature dependent, resulting in a temperature-dependent phosphorescence signal (S). Thus, in principle, the collected phosphorescence signal (S) may be used to measure fluid temperature if the incident laser intensity and the concentration of the phosphorescent dye remain constant (or are known) in the region of interest. It should be noted that the collected phosphorescence signal (S) is also the function of incident laser intensity (I_i) and the concentration of the phosphorescent dye (C). Therefore, the spatial and temporal variations of the incident laser intensity and the non-uniformity of the phosphorescent dye in the region of interest would have to be corrected separately in order to derive quantitative temperature data from the acquired phosphorescence images. To overcome this problem, Hu & Koochesfahani [67] developed a *lifetime-based* thermometry to eliminate the effects of incident laser intensity and concentration of phosphorescent dye on temperature measurements.

The lifetime-based thermometry works as follows: As illustrated in Figure 7.1, phosphorescence emission of the tagged tracer molecules is interrogated at two successive times after the same laser excitation pulse. The first image is detected at the time $t=t_0$ after laser excitation for a gate period δt to accumulate the phosphorescence intensity S_1, while the second image is detected at the time $t= t_0+\Delta t$ for the same gate period to accumulate the

phosphorescence intensity S_2. It is easily shown, using Equation (7.2), that the ratio of the two phosphorescence signals (R) is given by:

$$R = \frac{S_2}{S_1} = e^{-\Delta t/\tau} \tag{7.3}$$

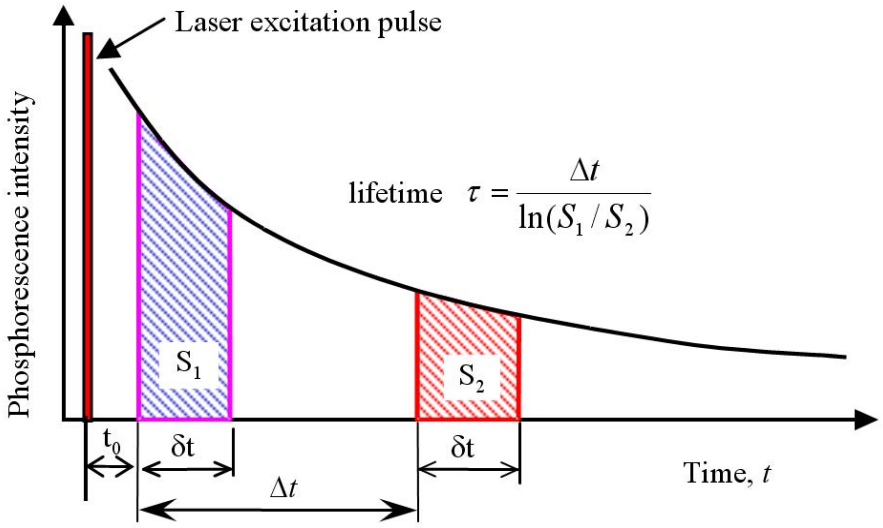

Figure 7.1. Timing chart for lifetime-based thermometry technique.

In other words, the intensity ratio of the two successive phosphorescence images is only a function of the phosphorescence lifetime τ, and the time delay Δt between the images, which is a controllable parameter. This ratiometric approach eliminates the variations in the initial intensity and, along with it, any temporal and spatial variations in the incident laser intensity (e.g. reflecting and/or scattering) and non-uniformity of the dye concentration (e.g. due to bleaching). The phosphorescence lifetime can be calculated according to

$$\tau = \frac{\Delta t}{\ln(S_1/S_2)} \tag{7.4}$$

For a given molecular tracer and fixed Δt value, Equation (7.3) defines a unique relation between phosphorescence intensity ratio (R) and fluid temperature T, which can be used for thermometry as long as the temperature dependence of phosphorescence lifetime is known.

7.2. Phosphorescent molecular tracers and experimental setup

7.2.1. Phosphorescent molecular tracers used in the present study

The phosphorescent molecular tracer used in the present study is phosphorescent triplex (1-BrNp·Mβ-CD·ROH). The phosphorescent triplex (1-BrNp·Mβ-CD·ROH) is actually the mixture compound of three different chemicals, which are lumophore (indicated collectively by 1-BrNp), maltosyl-β-cyclodextrin (indicated collectively by Mβ-CD) and alcohols (indicated collectively by ROH). Further information about the chemical and photoluminescence properties of the phosphorescent triplex is available at [68-71]. In the present study, we used a concentration of 2×10^{-4} M for Mβ-CD, a saturated (approximately 1×10^{-5} M) solution of 1-BrNp and a concentration of 0.06 M for the alcohol (ROH), as suggested by Gendrich et al. [70].

For a given molecular tracer, such as phosphorescent triplex 1-BrNp·Mβ-CD·ROH used in the present, and fixed Δt value, Equation (7.4) can be used to calculate the phosphorescence lifetime of the tagged molecules on a pixel-by-pixel basis, which would resulting in a distribution of the phosphorescence lifetime over a two-dimensional domain. Therefore, with a calibration profile of phosphorescence lifetime vs. temperature as the one shown in Fig. 7.2, a two-dimensional temperature distribution can be derived from a phosphorescence image

pair acquired after the same excitation laser pulse (The detailed procedures of MTT calibration test can be found in Appendix C).

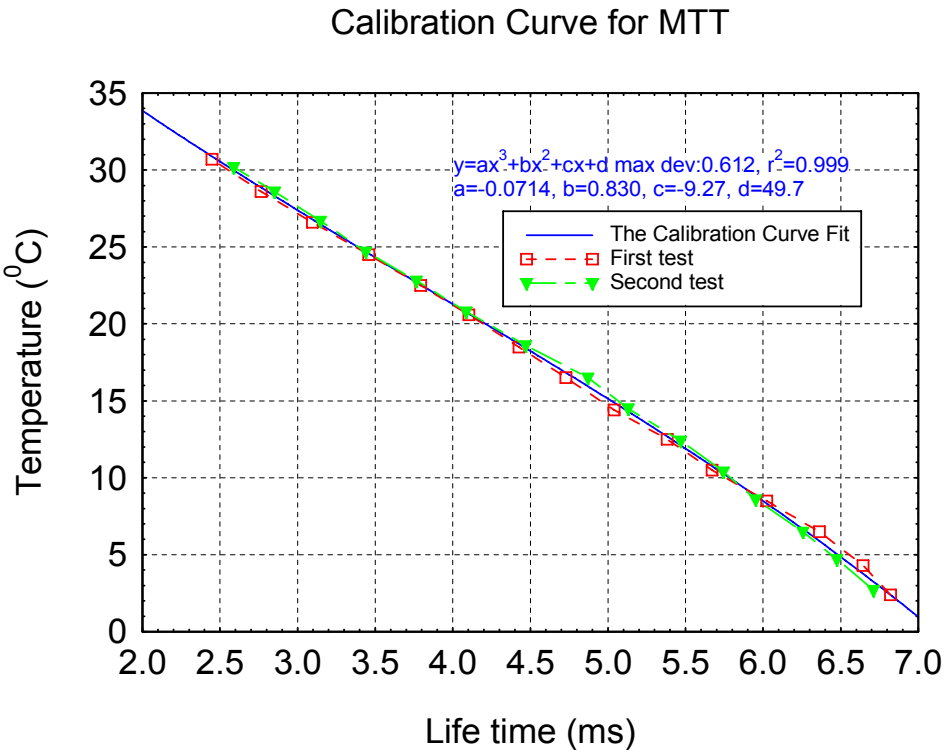

Figure 7.2. Variation of phosphorescence lifetime vs temperature

7.2.2. Experimental setup

Figure 7.3 shows the schematic of the experimental setup used for the demonstration experiments. A micro-sized water droplet was placed on an aluminum test plate. Phosphorescent triplex 1-BrNp·Gβ-CD·ROH was premixed within the water droplet. A laser sheet (~ 200 μm in thickness) from a pulsed Nd:YAG at quadrupled wavelength of 266nm was used to tag the premixed 1-BrNp·Gβ-CD·ROH molecules along the middle plane of the small water droplet, as shown in Fig. 7.3. A 12-bit gated intensified CCD camera (PCO DiCam-Pro) with a fast decay phosphor (P46) was used to capture the phosphorescence emission (The detailed PCO DiCam-Pro camera performance tests can be found in Appendix

D). A 10X objective (Mitsutoyo infinity-corrected) was mounted in the front of the camera. The camera was operated in the dual-frame mode, where two full-frame images of phosphorescence were acquired in a quick succession after the same laser excitation pulse. The camera and the pulsed Nd:YAG lasers were connected to a workstation via a digital delay generator (BNC 555 Digital Delay-Pulse Generator), which controlled the timing of the laser illumination and the image acquisition.

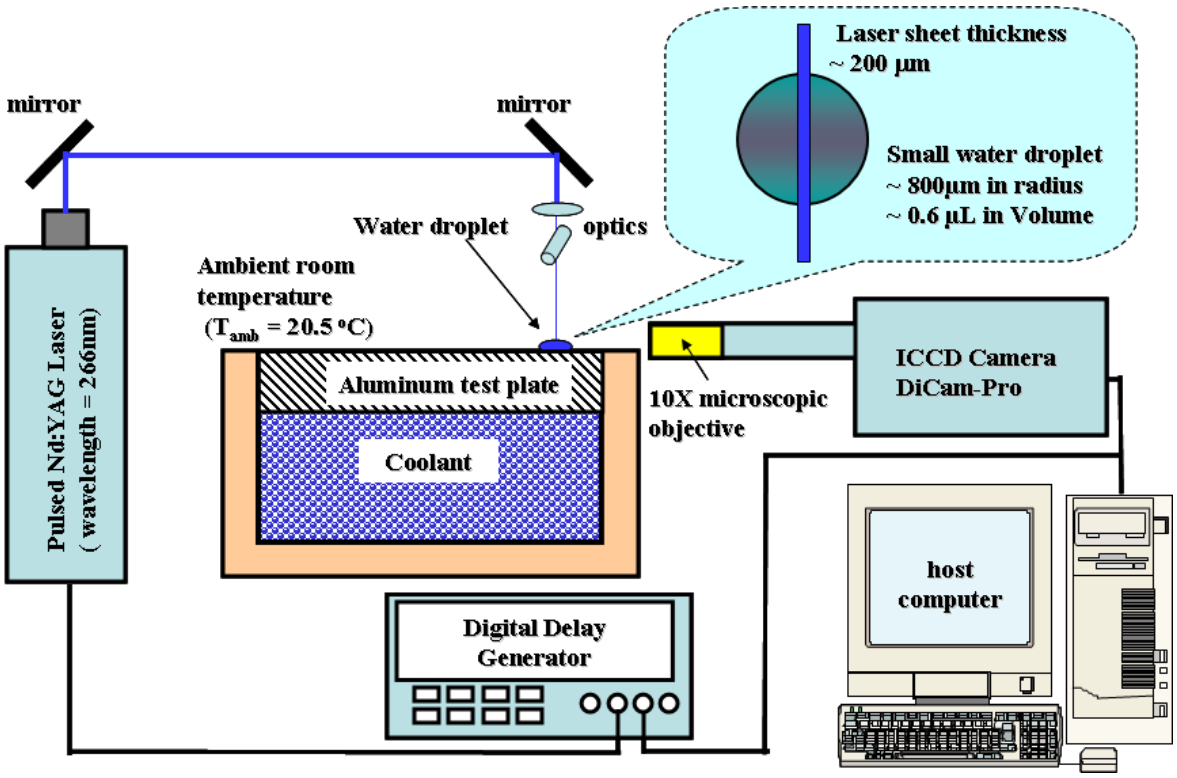

Figure 7.3. Experimental setup

7.3. Results and discussions

Figure 7.4 shows a typical phosphorescence image pair of the small water droplet placed on the aluminum test plate. The first image was acquired at 0.5 ms after the laser pulse and the

second image at 3.5 ms after the same laser pulse with the same exposure time of 1.5 ms for the two image acquisitions. As described above, since the time delays between the laser excitation pulse and the phosphorescence image acquisitions can eliminate scattered/reflected light and any fluorescence from other substances (such as from solid surface) in the measurement region effectively, the phosphorescence images of the water droplet are quite "clean". With the calibration profile of phosphorescence lifetime vs. temperature shown in Figure 7.2, a two-dimensional, instantaneous temperature distribution within the water droplet can be derived from the phosphorescence image pair.

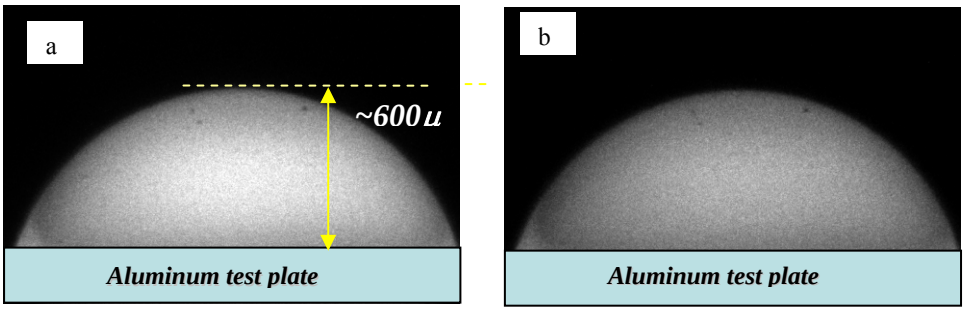

a). The first phosphorescence image acquired at 0.5ms after laser pulse

b). The second phosphorescence image acquired at 3.5ms after the same laser pulse

Figure 7.4. A typical phosphorescence image pair acquired for MTT measurement

For the first demonstration experiment, no coolant was placed underneath the aluminum test plate. A micro-sized water droplet with its temperature of 20.5^{o}C (room temperature) was placed on the aluminum test plate, and the surface temperature of the test plate was as the same as the room temperature of 20.5^{o}C, measured by using a thermocouple. Figure 7.5(a) shows the profiles of the acquired phosphorescence intensity, within a small region of 10 pixel × 10 pixels (about 14μm × 14μm in physical plane) near the center of the water

droplet, for the first and second phosphorescence images as a function of the numbers of the excitation laser pulse. The acquired phosphorescence intensities were found to decay monotonically with the increasing numbers of excitation laser pulse due to the photobleaching effect. However, the calculated phosphorescence lifetime, shown in Figure 7.5(b), remains constant, as expected, at a level corresponding to the room temperature of 20.5^{o}C. The Root-Mean-Square (RMS) value of the measured temperature was found be about 0.35 ^{o}C.

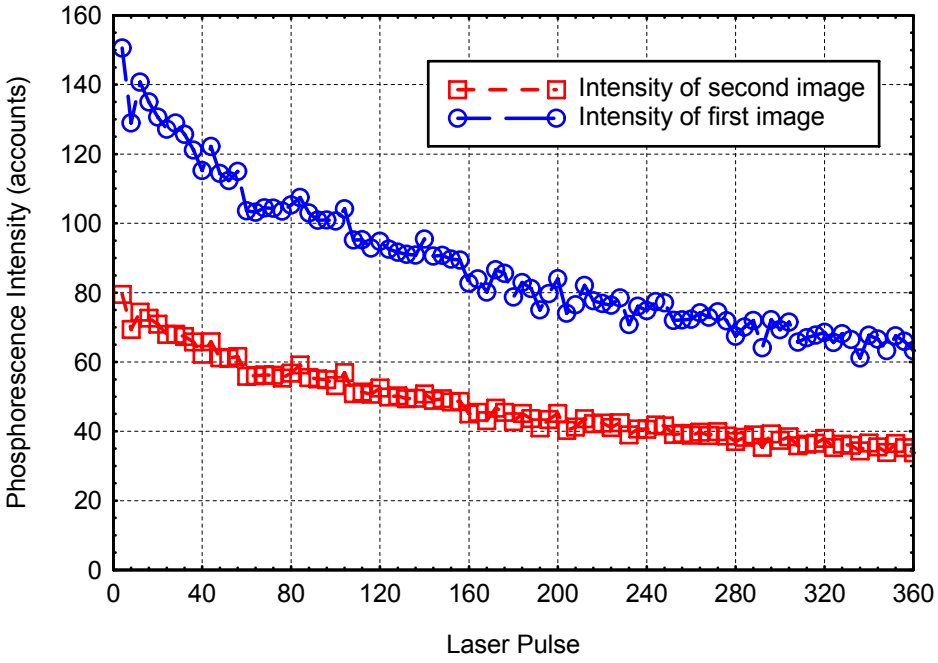

a. Acquired phosphorescence intensities vs. number of laser pulse

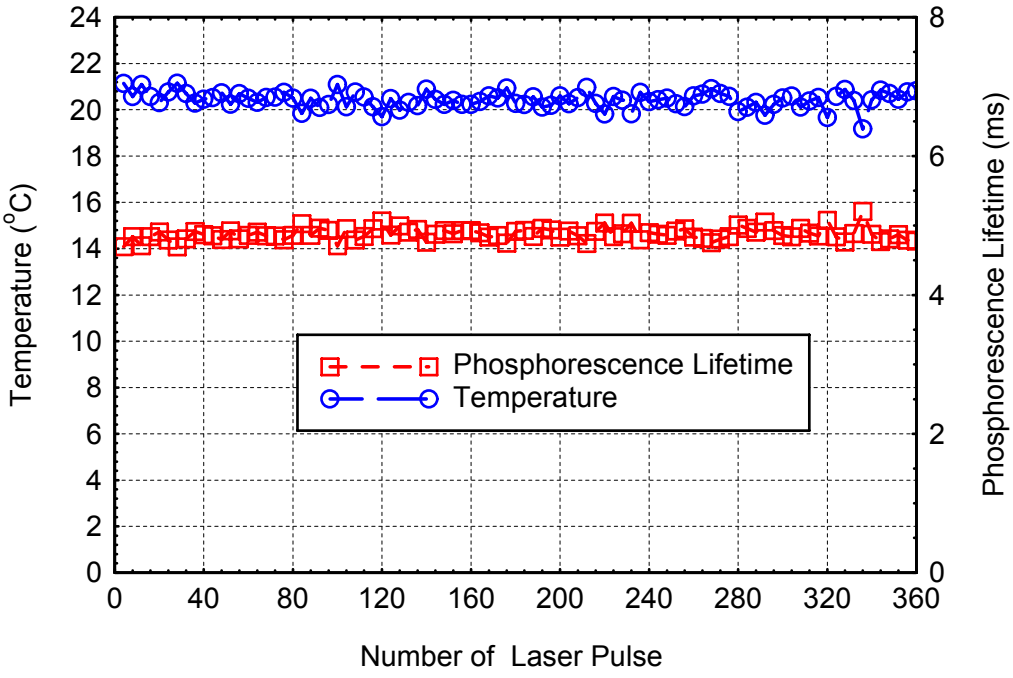

b. Derived phosphorescence lifetime and temperature vs. numbers of laser pulse

Figure 7.5. Compensation of photobleaching effect

Then, the surface temperature of the aluminum test plate was maintained at 2.0 ^{o}C (measured by using a thermocouple) by placing coolant underneath the aluminum test plate to demonstrate the feasibility and implementation of the lifetime-based MTT technique for measurements of transient temperature distribution within a convectively-cooled, micro-sizes water droplet on the test plate. A small water droplet (~ 0.6μ liter in volume) with initial temperature of 20.5^{o}C (room temperature) was placed on the aluminum test plate. The water droplet would be convectively cooled after it was placed on the cold test plate.

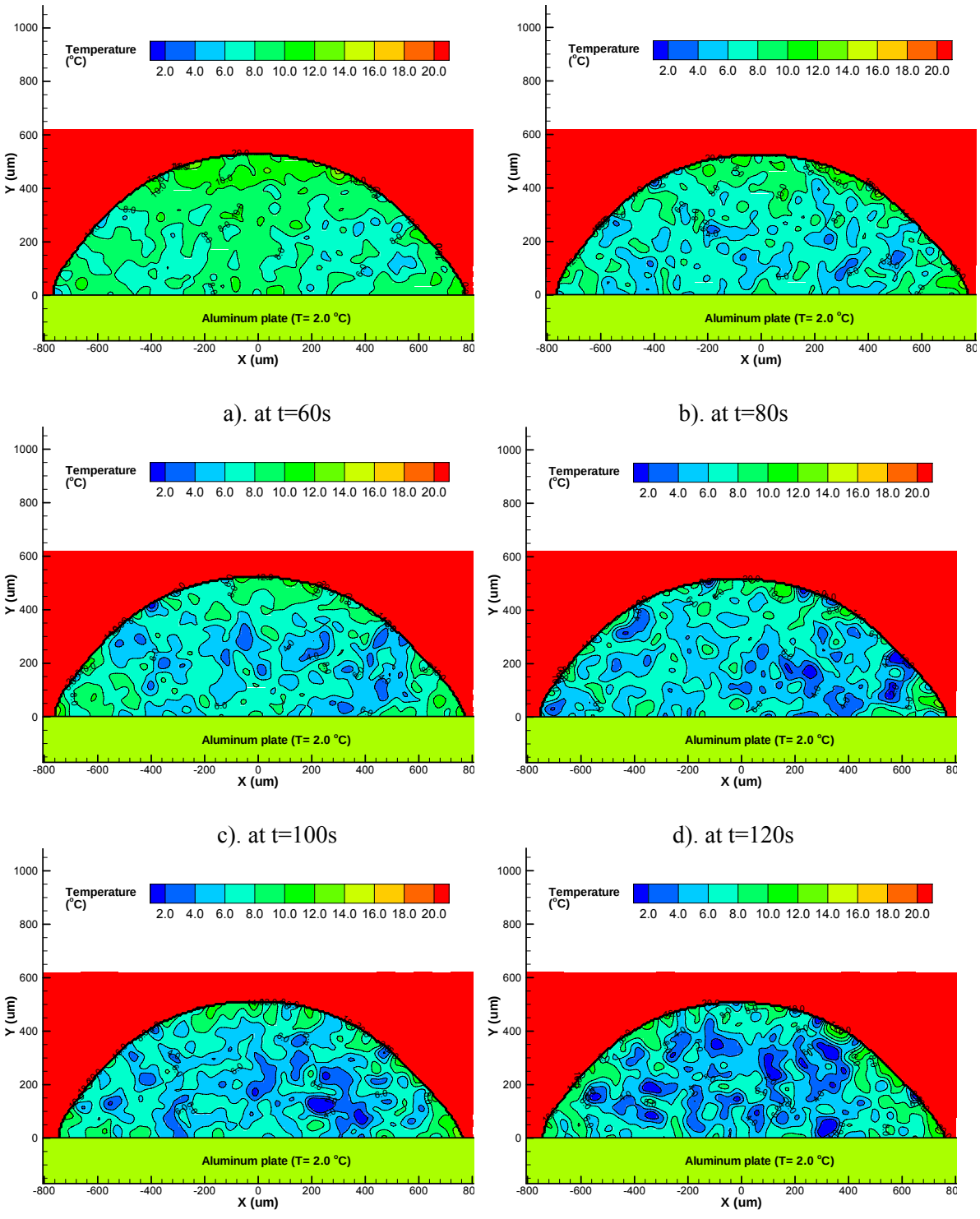

a). at t=60s

b). at t=80s

c). at t=100s

d). at t=120s

e). at t=140s

f). at t=160s

Figure 7.6. Instantaneous temperature distributions within the convectively-cooled water droplet

Figure 7.6 shows the measured instantaneous temperature distributions within the convectively-cooled water droplet as a function of the time after the droplet was placed on the test plate. Due to the relatively high temperature sensitivity of the present lifetime-based MTT technique, the small temperature difference within the small water droplet can be revealed clearly from the measured instantaneous temperature distributions. As it is expected, the regions with lower temperature values were found to concentrate mainly near the bottom the water droplet. As the time goes by, more and more dark regions, i.e., lower temperature regions, were found in the measured instantaneous temperature distributions, which indicates the temperature of the water droplets became lower and lower due to the convective cooling.

Figure 7.7 shows the profile of the spatially-averaged temperature of the water droplet as a function of the time, which was calculated based on the time sequence of the measured instantaneous temperature distributions. The characteristics of the unsteady heat transfer process within the convectively cooled water droplets were revealed quantitatively from the evolution of the spatially-averaged temperature of the water droplet. Since initial temperature of the water droplet (20.5 ^{o}C) was significantly higher than that of the cold aluminum test plate (2.0 ^{o}C), the spatially-averaged temperature of the water droplet was found to decrease rapidly and monotonically after it was placed on the cold aluminum test plate. The temperature measurement results given in Figure 7.7 also revealed that a thermal equilibrium state would be reached at about 150 seconds later after the water droplet was placed on the cold test plate. The spatially-averaged temperature of the water droplet would not decrease anymore when the thermal equilibrium state was reached. The spatially-averaged

temperature of the water droplet was found to be about 6.0 ^{o}C after the thermal equilibrium state was reached.

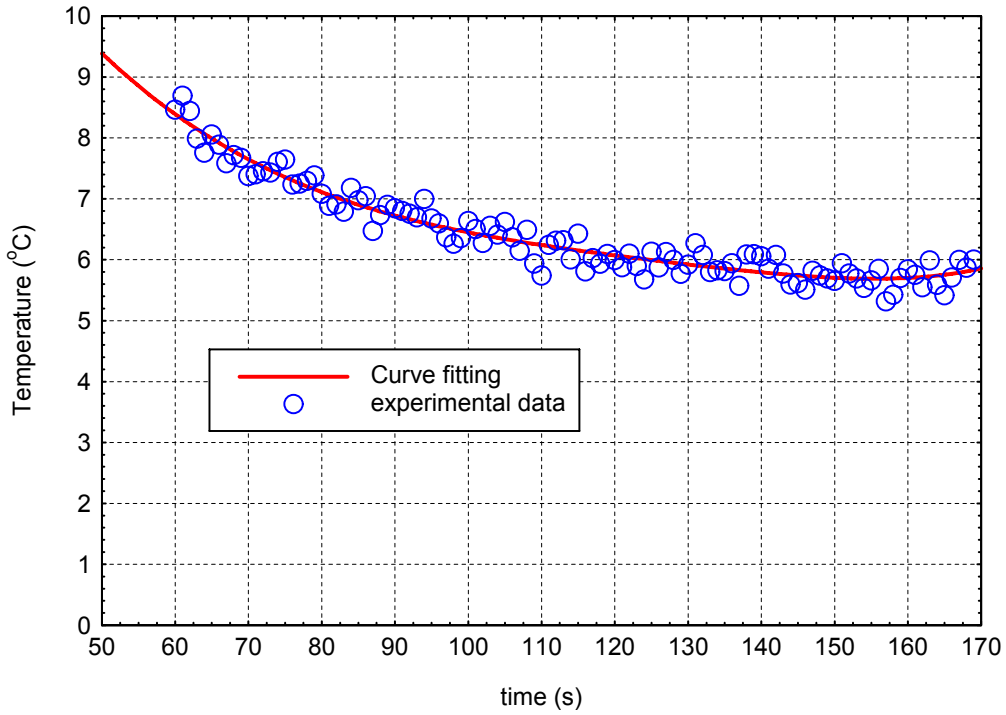

Figure 7.7. Spatially-averaged temperature of the small water droplet vs. time

As demonstrated by the measurement results shown above, the lifetime-based MTT technique described in the present study is capable of providing detailed measurements to quantify the unsteady mass and heat transfer processes within convectively-cooled, small water droplets on solid surfaces. Such information is highly desirable to elucidate underlying physics to improve our understanding about micro-physical phenomena for various microfluidics studies.

CHAPTER 8: CONCLUSIONS AND FUTURE WORK

In this chapter, the major objectives met in this dissertation are summarized and discussed, and future work with regard to mixing enhancement in microchannels and heat and mass transfer in surface droplets is also suggested.

8.1. Two-stream mixing enhancement study in a Y-shaped microchannel by utilizing electrokinetic instabilities (EKI)

Epifluorescence microscopy technique was used to conduct qualitative flow visualization and quantitative scalar concentration field measurements to quantify the fluid mixing process inside a Y-shaped microchannel in terms of scalar concentration distribution, shedding frequency of the EKI waves and scalar mixing efficiency.

The critical strength of the applied static electric field decreases rapidly with the increasing conductivity ratio. The amplitude of the interface fluctuation, i.e., the size of the convective EKI waves, was found to increase rapidly as the applied static voltage increased, which results in that the fluid mixing efficiency increases monotonically with the increasing strength of the applied static electric field.

The fluid mixing process inside the Y-shaped microchannel can be most enhanced when the frequency of the applied alternative perturbation equals to the natural shedding frequency of the EKI waves. This fact may be explained by the concept of hydrodynamic resonance, which has been widely employed in many active flow control studies. The fluid mixing

efficiency is also quite sensitive to the amplitude of the alternative perturbation. The mixing argumentation factor was found to increase almost linearly with the amplitude of the applied alternative perturbation when the perturbation amplitude is relatively small (<200V). The fluid mixing efficiency was found to increase much more rapidly as the perturbation amplitude becomes relatively large (> 200V).

To the author's best knowledge, this work represents the first two-stream mixing enhancement study in Y-shaped microchannels by utilizing electrokinetic instabilities (EKI).

8.2. The study of the effect of the geometry of different Y-shaped microchannels on mixing enhancement by utilizing EKI

Three Y-shaped microchannels were used which are termed as channel with cavities, channel with steps and straight channel. Since the mixing efficiencies in different depths of the channel with steps do not change much, the middle depth of the microchannels was selected to study mixing process. As the strength of the static electric field is low, the mixing efficiency of the straight channel is higher than that of the channel with cavities, which is due to the fact that channel with cavities needs higher strength of the static electric field to induce the EKI waves than the straight channel. However, when the applied static electric field is higher than 1250V, the mixing efficiency of the channel with cavities becomes higher than the straight one. The channel with steps has relatively smaller values when compared to the other two microchannels.

For both straight channel and channel with cavities, mixing efficiency reaches its highest point when the imposed frequency of external force is the same as the natural frequency of the system. However, for the channel with steps, this optimum frequency phenomenon is difficult to identify. The mixing frequency has relatively high values when frequency is near 1 and 10. It also should be noted that the channel with cavities has higher mixing augmentation factors than the other two channels.

For all the microchannels, the mixing augmentation factors keep increasing with the increase of the magnitude of the alternative electric perturbation. For straight channel and channel with steps, their mixing augmentation factors are almost the same when the magnitude of the perturbation is relatively low (<300V). Meanwhile, the mixing augmentation factors of the channel with cavities increase at a higher rate than those of the other two channels.

For all the microchannels, the mixing augmentation factors are greater than 1 which means that the alternative perturbations do enhance the mixing processes in the microchannels.

This work represents the first experimental study on the effect of the geometry of different Y-shaped microchannels on mixing enhancement by combining alternative perturbations and static electric field together as EKI waves' generation sources. All the previous studies either focus on using AC and DC together to one particular microchannel or applying static electric field only to several microchannels. To the author's best knowledge, no one has ever

combined both AC and DC together as the EKI waves generation sources to study different types of Y-shaped microchannels at the same time.

8.3. Velocity measurement in surface droplets on a test plate of different temperatures

The velocity distributions inside surface droplets on a plate of different temperatures (from 21.9°C to 0°C) were measured by using the Particle Image Velocimetry (PIV) technique. The significant image distortion problem caused by the refraction of light at the droplet surface was corrected by an image mapping method. The flow pattern found in present study was contrary to the theoretical thermal Marangoni flow pattern. The possible reason for this might be that surface tension gradient was formed on the droplet because of particle concentration gradient. Even though the particles were premixed well with water before the experiments, they tended to sink toward the test plate due to gravity, which caused the particle concentration in the lower part is higher than that of the upper part. Because the surface tension of the solvent increases with increasing particle concentration, the high surface tension pulls more strongly on the surrounding liquid than one with a low surface tension. The presence of a gradient in surface tension caused the liquid to flow away from regions of low surface tension and formed a flow pattern as shown in Figure 6.2a.

Contact angle and normalized droplet volume were also investigated in present study. As the decrease of plate temperature, droplets became less likely to evaporate. At the same time, the

condensation process became more prominent, which turned water vapor into liquid water and enlarged both volume and contact angle of droplets.

To compare the effect of plate temperature on the velocity magnitude, a point was selected in the middle of the droplet. For all the cases, the magnitude of the velocity decreased with time while the velocity for the case of room temperature remained the highest. As the temperature of the plate dropped, velocity also decreased which was due to the cooling down process from the cold plate. However, for the cases of 5.0°C and 0.0°C, the velocity curves were almost the same.

To the author's best knowledge, this work represents the first experimental investigation of the effect of plate temperature on velocity distributions inside surface droplets.

8.4. Transient temperature measurement inside surface droplets by using Molecular Tagging Thermometry (MTT)

For MTT technique, only one laser pulse and one dual-frame CCD camera is required which is much simpler compared to LIF technique. The small time delay between the illumination laser pulse and the phosphorescence image acquisition can effectively eliminate all the effects of scattered/reflected light and any fluorescence from other substances that are present in the measurement region. Furthermore, the high temperature sensitivity of the present lifetime-based MTT technique is highly favorable for the accurate measurements of small temperature differences within small water droplets.

For the first demonstration experiment, no coolant was placed underneath the test plate. A micro-sized water droplet was placed on the aluminum test plate, and both the droplet temperature and the surface temperature of the test plate were the same as the room temperature of 20.5^{o}C. The acquired phosphorescence intensities were found to decay monotonically with the increasing numbers of excitation laser pulse due to the photobleaching effect. However, the calculated phosphorescence lifetime remains constant, at a level corresponding to the room temperature of 20.5^{o}C. The Root-Mean-Square (RMS) value of the measured temperature was found be about 0.35 ^{o}C. For the second demonstration experiment, the surface temperature of the aluminum test plate was maintained at 2.0 ^{o}C and a small water droplet with initial temperature of 20.5^{o}C was placed on the aluminum test plate. Due to the relatively high temperature sensitivity of the present lifetime-based MTT technique, the small temperature difference within the small water droplet can be revealed clearly from the measured instantaneous temperature distributions. As it is expected, the regions with lower temperature values were found to concentrate mainly near the bottom the water droplet. As the time goes by, more and more dark regions, i.e., lower temperature regions, were found in the measured instantaneous temperature distributions, which indicates the temperature of the water droplets became lower and lower due to the convective cooling.

This work represents the first transient temperature measurement in surface droplets by using Molecular Tagging Thermometry (MTT) technique.

8.5. Future work

As for the microchannels, some research work is suggested to be done in the future. Although three different Y-shaped microchannels were designed in the present study, the main channel part is still straight to some degree. In order to further enhance the mixing efficiency in Y-shaped microchannels, a zigzag shape can be designed at the conjunction part of two inlet channels.

As for the surface droplets, more work is needed to elucidate the exact cause for the present flow pattern. Also, the study of surface droplets' phase change process from liquid to solid has an important application directly related to aircraft icing. Lifetime-based molecular tagging thermometry (MTT) technique can be used to quantify important ice growth physical processes such as unsteady heat transfer process within water droplets or ice crystals and phase change process of super-cooled water droplets over solid surfaces. In addition, since present study only focuses on droplets on a cooling plate, considering that there are lots of droplet applications on heating plates, more temperature and velocity measurements need to be conducted with droplets on a heating plate. At the same time, since the evaporation process of surface droplets also depends on humidity, the velocity and temperature distributions inside surface droplets under different humilities can be quantified in the future. Besides, since the temperature of the plate affects the velocity distributions inside the droplets, it might affect deposition pattern as well, which would also be an interesting topic to study.

APPENDIX A: DROPLET DISTORTION CORRECTION

When conducting PIV measurements on surface droplets, the refraction of flight at the droplet surface causes a significant image distortion problem. Figure A-1(a) shows a typical image of seed particles in a cross-sectional plane of an evaporating droplet and the velocity vectors obtained with the PIV method. Figure A-1(b) shows a strong upward flow in the centre region and a relatively weak downward flow at the boundary region of the droplet. With the velocity vectors alone, the continuity requirement appears to be violated. This results form the distortion of particle images due to the lens effect of the droplet itself. Thus, it becomes obvious why the flow field should be corrected.

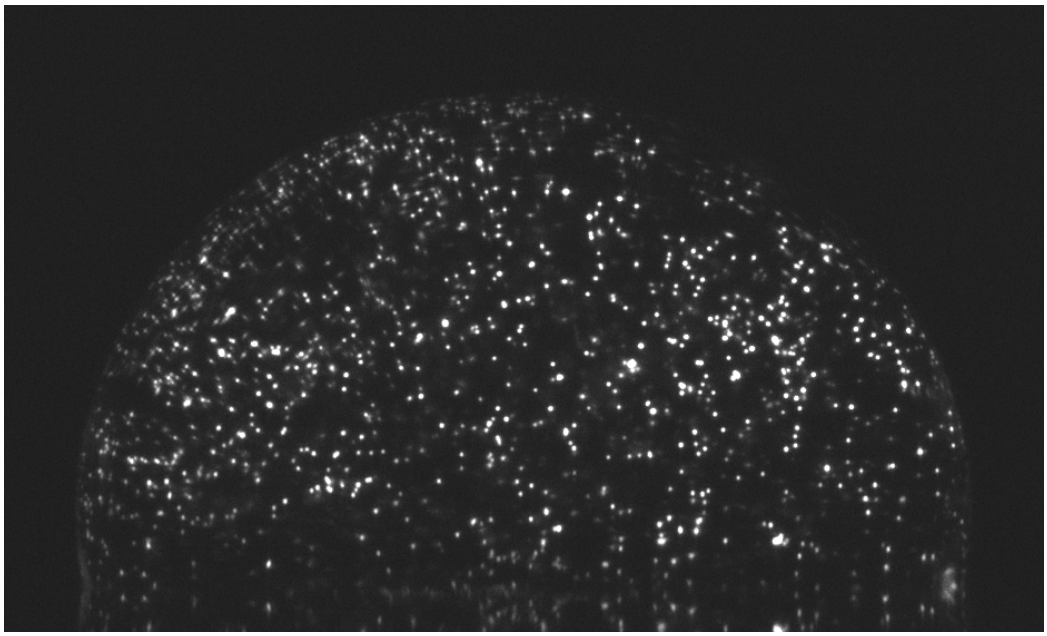

(a)

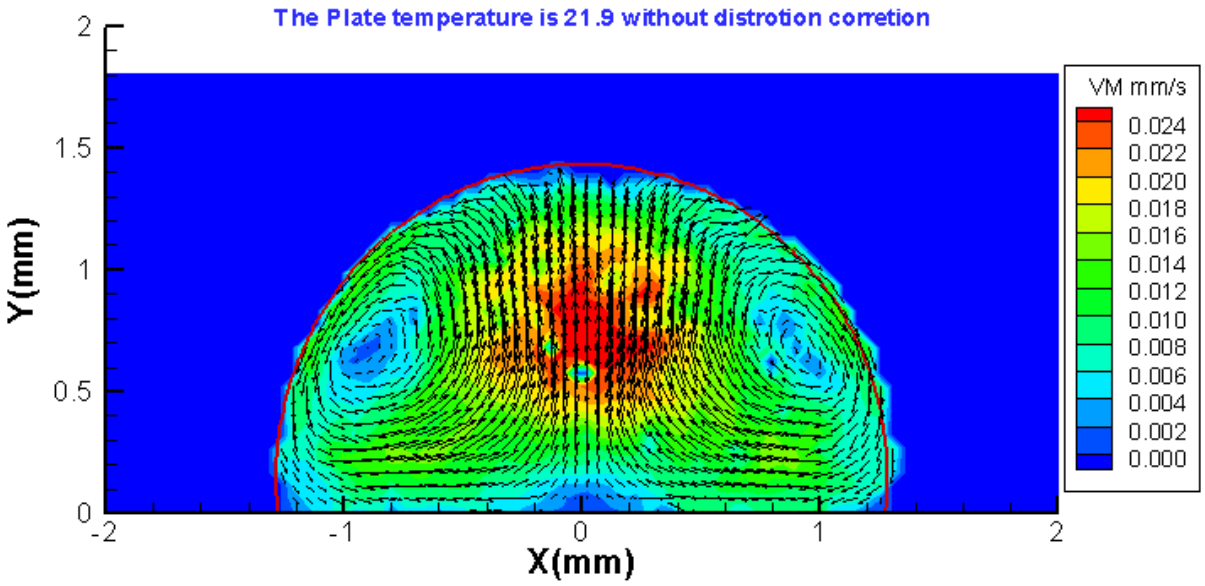

(b)

Figure A-1. PIV image and velocity result of surface droplet without distortion correction

Several researchers have worked out a ray tracing method to solve the problem [35, 36], the detailed derivation process of which is explained in the following contents.

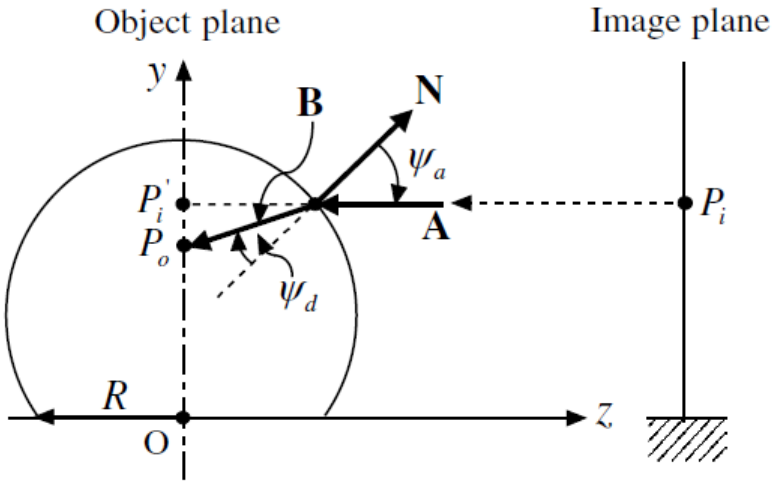

Figure A-2. Tracing of a ray normally incident to the object plane.

As shown in Figure A-2, the rays are refracted as they pass through the droplet surface. The incident and the transmitting angles of a ray passing through the droplet surface are related by the following Snell's law of refraction

$$n_d \sin\psi_d = n_a \sin\psi_a \qquad (1)$$

where n_d and n_a are the refractive indices of air and the fluid inside the droplet, respectively, and ψ_a and ψ_d are the respective incident and transmitting angles of the rays.

The geometrical relationship between the point *P*i on the image plane and the point *P*o on the object plane (see Figure A-3) for an axisymmetric droplet is derived. We introduce the(*x, y, z*) Cartesian coordinate system and the*(r, θ, φ)* spherical coordinate system which have the origin at the centre of the base circle of the droplet. The unit vectors in the *x*, *y* and *z* directions are denoted by $\hat{i}$, $\hat{j}$ and $\hat{k}$, and those in the *r*, *θ* and *φ* directions are denoted by e_r, e_θ and e_ϕ, respectively.

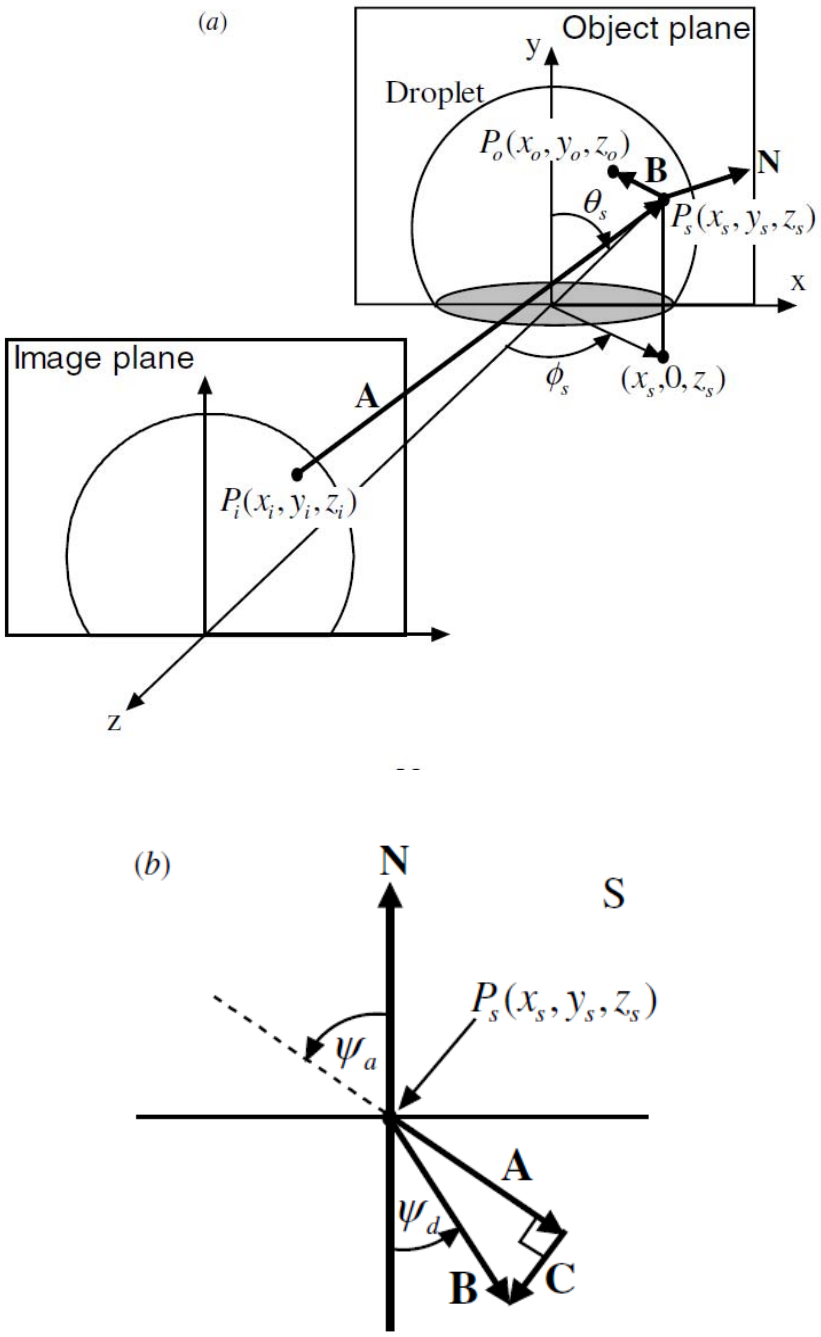

Figure A-3. Coordinate system and the vector relationship at the surface of the droplet

The shape of an axisymmetric droplet can be represented by the function *F(r, θ)* defined as

$$F(r,\theta) = r - \varsigma(\theta) = 0 \qquad (2)$$

The shape function $\varsigma(\theta)$ is represented by a sum of the cosine series as shown below

$$\varsigma(\theta) = R + \sum_{k=1}^{N} b_k \cos k\theta \cong R + b\cos\theta \qquad (3)$$

The droplet surface is usually well represented by $R + b\cos\theta$, and all the higher order terms of the cosine series are neglected for simplicity of analysis. The unknown constants R and b are determined using a digitized image of the droplet.

A point $P_i^{'}$ is defined as the projected point of P_i onto the object plane. The vectors $OP_i^{'}$, $\overrightarrow{OP_s^{'}}$, $\overrightarrow{OP_o^{'}}$ are written as:

$$\overrightarrow{OP_i^{'}} = x_i\hat{i} + y_i\hat{j} \qquad (4)$$

$$\overrightarrow{OP_s^{'}} = x_s\hat{i} + y_s\hat{j} + z_s\hat{k} \qquad (5)$$

$$\overrightarrow{OP_o^{'}} = x_o\hat{i} + y_o\hat{j} \qquad (6)$$

Since $x_s = x_i$ and $y_s = y_i$ and P_s is on the droplet surface, we can obtain unknown z_s for given x_i and y_i by using equation (2) and (3)

$$r_s = R + b\cos\theta_s = R + \frac{by_s}{r_s}$$

Where $r_s = (x_s^2 + y_s^2 + z_s^2)^{1/2}$. From the above equation, it becomes

$$r_s = \frac{R + \sqrt{R^2 + 4by_s}}{2} \qquad (7)$$

And

$$z_s = \sqrt{r_s^2 - x_s^2 - y_s^2} \tag{8}$$

Let $\vec{A} \equiv \overrightarrow{P_i P_s}$ and $\vec{B} \equiv \overrightarrow{P_s P_o}$, then the vector $\vec{A}$ is represented, in both the Cartesian and the spherical coordinate systems, as

$$\vec{A} = -\hat{k} = -\sin\theta_s \cos\phi_s \hat{e}_r - \cos\theta_s \cos\phi_s \hat{e}_\theta - \sin\phi_s \hat{e}_\phi \tag{9}$$

where

$$\cos\theta_s = \frac{y_s}{r_s} \tag{10}$$

$$\sin\theta_s = \frac{\sqrt{x_s^2 + z_s^2}}{r_s} \tag{11}$$

$$\cos\phi_s = \frac{z_s}{\sqrt{x_s^2 + z_s^2}} \tag{12}$$

$$\sin\phi_s = \frac{x_s}{\sqrt{x_s^2 + z_s^2}} \tag{13}$$

The vectors $\vec{A}$, $\vec{B}$ and $\vec{N}$ exist on the same plane S, in with $\vec{N}$ denotes the outward unit normal vector on the droplet surface. From the shape function for the droplet shown in equation (3), $\vec{N}$ becomes

$$\vec{N} = \frac{\nabla F}{|\nabla F|} \tag{14}$$

where

$$\nabla F = \frac{\partial F}{\partial r}\hat{e}_r + \frac{1}{r}\frac{\partial F}{\partial \theta}\hat{e}_\theta = \hat{e}_r + \frac{b\sin\theta}{r}\hat{e}_\theta \tag{15}$$

and

$$\left|\nabla F\right| = \frac{\sqrt{r^2 + b^2 \sin^2\theta}}{r} \tag{16}$$

Thus

$$\vec{N} = \frac{r}{\sqrt{r^2 + b^2 \sin^2\theta}}\hat{e}_r + \frac{b\sin\theta}{\sqrt{r^2 + b^2 \sin^2\theta}}\hat{e}_\theta \tag{17}$$

A unit vector normal to the plane S becomes $\vec{D} = \vec{N} \times \vec{A}$. If we define a vector $\vec{C}$ which is parallel to the plane S and normal to the vector $\vec{A}$, it becomes (see figure 4)

$$\vec{B} = \vec{A} + \vec{C}$$

$$= \vec{A} + \tan(\psi_a - \psi_d)\frac{(\vec{N} \times \vec{A}) \times \vec{A}}{\left|(\vec{N} \times \vec{A}) \times \vec{A}\right|}$$

$$= \frac{-\tan(\psi_a - \psi_d)N_i}{\sqrt{N_i^2 + N_j^2}}\hat{i} + \frac{-\tan(\psi_a - \psi_d)N_j}{\sqrt{N_i^2 + N_j^2}}\hat{j} + \hat{k} \tag{18}$$

The common factor between the $\hat{i}$ and $\hat{j}$ terms of equation (18), after substitution of N_i, N_j and N_k and some simplification, will be defined as

$$f_M = \frac{1}{\sqrt{\sin^2\theta \sin^2\phi (r + b\cos\theta)^2 + (r\cos\theta - b^2 \sin^2\theta)^2}} \tag{19}$$

Thus we have

$$\vec{B} = -f_M \tan(\psi_a - \psi_d)(r + b\cos\theta)\sin\theta \sin\phi \hat{i}$$

$$- f_M \tan(\psi_a - \psi_d)(r\cos\theta - b\sin^2\theta)\hat{j} + \hat{k} \tag{20}$$

The line passing through the points P_s and P_o having the direction vector $\vec{B}$ is written as

$$\frac{x - x_s}{B_x} = \frac{y - y_s}{B_y} = \frac{z - z_s}{B_z} \tag{21}$$

where B_x, B_y and B_k are the vector components of $\vec{B}$ in the Cartesian coordinate system. The coordinate of the intersecting point between the line and the plane z=0 (i.e., P_o becomes

$$x_0 = x_i - z_s \frac{B_x}{B_z}$$

$$= x_i + z_s f_M \tan(\psi_a - \psi_d)(r + b\cos\theta)\sin\theta\sin\phi \tag{22}$$

$$y_0 = y_s - z_s \frac{B_y}{B_z}$$

$$= x_i + z_s f_M \tan(\psi_a - \psi_d)(r\cos\theta - b\sin^2\theta) \tag{23}$$

APPENDIX B: LASER AND CAMERA SYCHRONIZATION SETUP FOR PIV

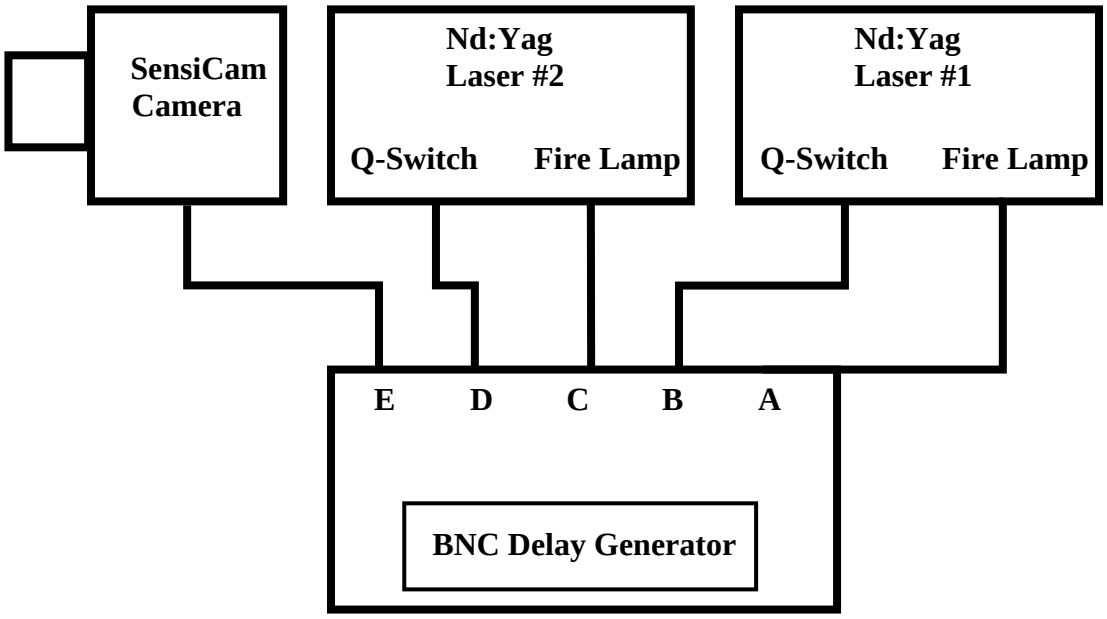

Note: A, B, C, D and E are output channels of the Delay Generator

Figure B-1. The synchronization setup for laser and camera

The following timing settings are default values used for general PIV measurements:

Pulse Output Channel	Time Delay	Pulse Width
Channel A (to flash lamp #1)	0	100 μs
Channel B (to Q-switch #1)	200 μs	2 ms
Channel C (to flash lamp #2)	Δt for PIV measurement	100 μs
Channel D (to Q-switch #2)	Δt +200 μs	2 ms
Channel E* (to Sensicam Camera)	103 μs (t_{ed})	100μs (t_{ew})

Table B-1. The timing setting for PIV measurement

* Note: following requirement should be met for the timing setting of the Channel E (time delay, t_{ed} and pulse width, t_{ew}) in order to make sure that the two laser pulses can be imaged at two PIV image frames:

$$200\ \mu s + 130\ \text{ns} < (<1\ \mu s \text{ delay of camera}) + t_{ed} + t_{ew} < \Delta t + 200\ \mu s - 70\text{ns}$$

APPENDIX C: CALIBRATION FOR MTT SOLUTION

Figure C-1 shows the schematic setup of the calibration procedure employed to quantify the relative phosphorescence signal R, defined in Eq. 7.3, for 1-BrNp•Mb-CD•ROH. A Nd-Yag laser (wavelength k=266nm) with appropriate optics was used to generate a laser sheet (thickness about 1 mm) to illuminate a cube-shaped test cell (about 2 l in volume) containing an aqueous solution of 1-BrNp•Mb-CD•ROH complex. The apparatus was placed on a heating plate and a stirring rod was used to achieve thermal equilibrium in the test cell. An RTD probe (Hart Scientific Model 1502A, temperature accuracy±0.01°C) was placed in one corner of the apparatus to measure the actual temperature in the test cell. During the experiment, the temperature uniformity inside the test cell was checked and was found to be within 0.1°C.

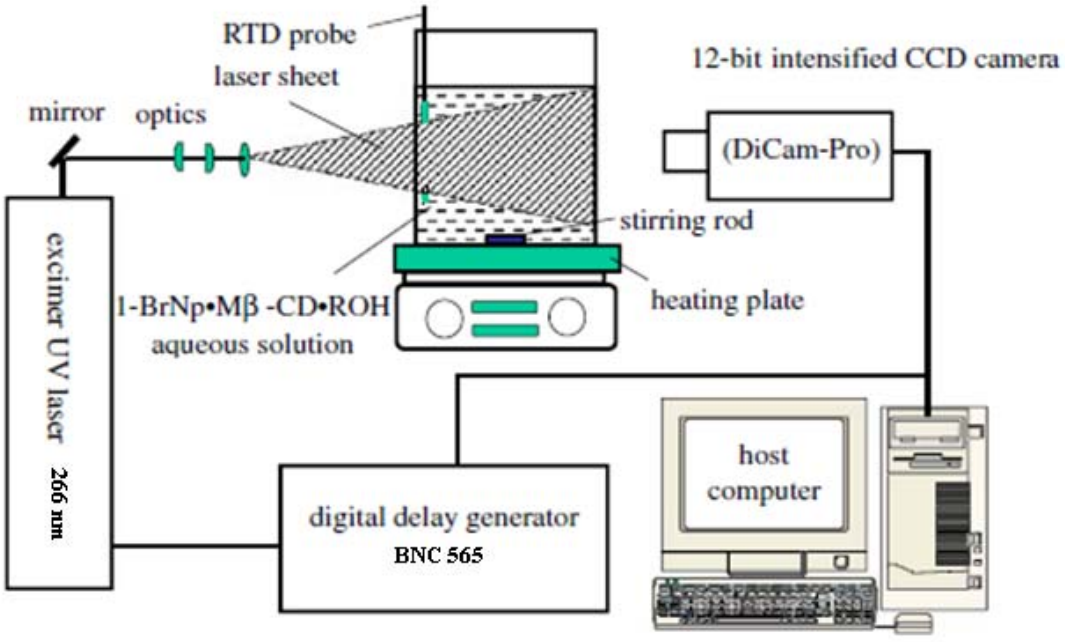

Figure C-1. The setup for MTT solution calibration

A 12-bit, 1,280×1,024 pixels, an intensified CCD camera (PCO DiCam-Pro) was used to capture the phosphorescence emission. The laser and the camera were synchronized using a digital delay generator (BNC Model565), which controlled the delay time to between the laser pulse and the start of image capture, and the integration period Δt. The phosphorescence images were subsequently transferred to a host computer for analysis. In the present study, the exposure time was set to a fixed value of Δt = 1.5 ms. To acquire the calibration data, the aqueous solution of 1-BrNp•Mb-CD•ROH was first heated to a predetermined temperature level. After thermal equilibrium was established, the phosphorescence images were acquired as a function of time delay to. The process was repeated for different solution temperatures.

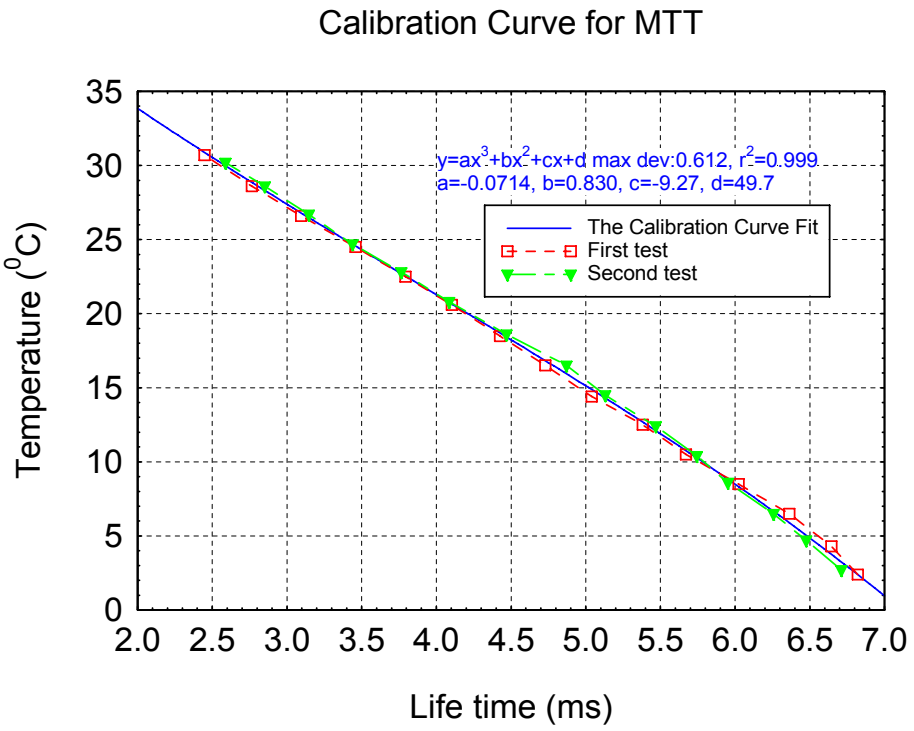

Figure C-2. Variation of phosphorescence lifetime vs temperature

Figure C-2 depicts the measured phosphorescence life time curves at several temperature levels. It can be seen that the life time of the 1-BrNp•Mb-CD•ROH complex increases as the drop of the solution temperature.

APPENDIX D: PERFORMANCE OF DICAM PRO INTENSIFIED CAMERA

An intensified camera has an added intensifier to the CCD and typically exhibits a non-linear gain response. This is especially a concern for the MTT technique where the intensity decay of the image is used to infer temperature information. Thus, characterization of the intensifier is important.

In the present work, to fully understand Dicam Pro intensified camera performances, both single shot mode and double shot mode were studied. During the experiments, an electric bubble was used to do illumination. A paper sheet with different grey level was used as object for image recording (see figure D-1). 128 images were averaged for each case in order to reduce the noisy level.

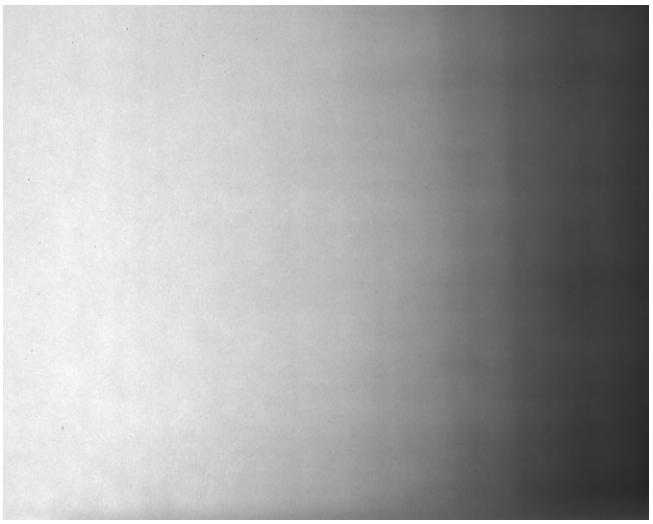

Figure D-1. The image of paper sheet with different grey level

D.1. Single Shot Mode

D.1a. exposure effect

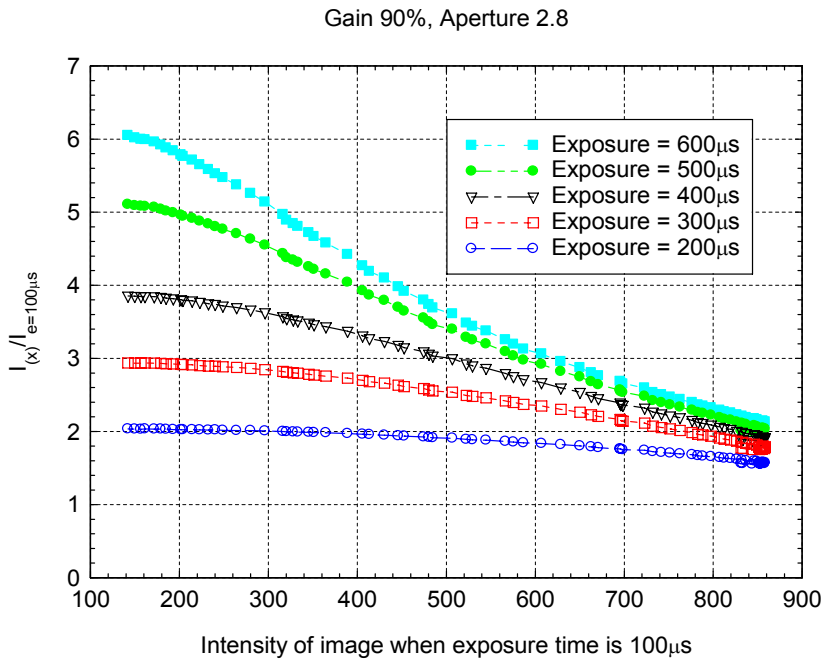

Figure D-2. The intensity ratio curves (exposure time effect)

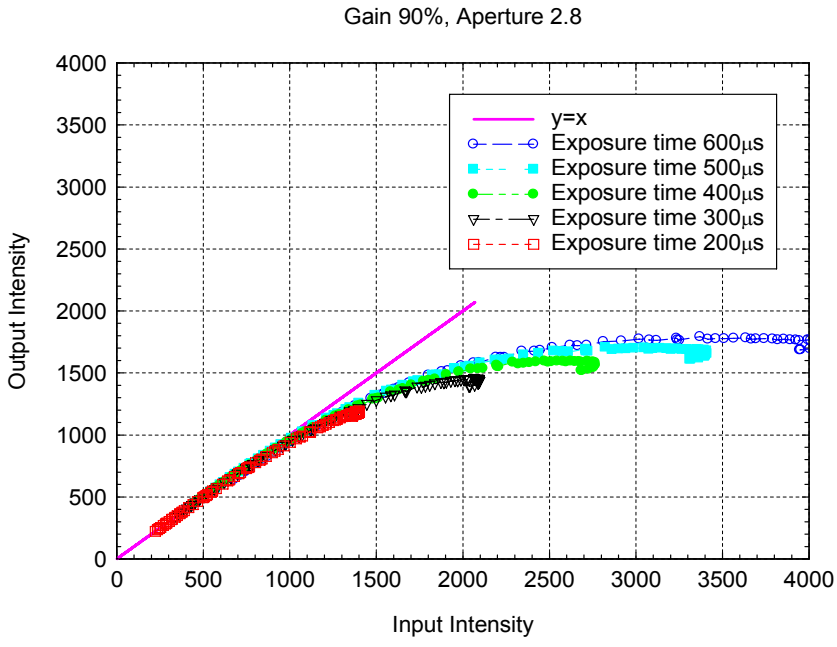

Figure D-3. Response of Dicam-Pro Camera (exposure time effect)

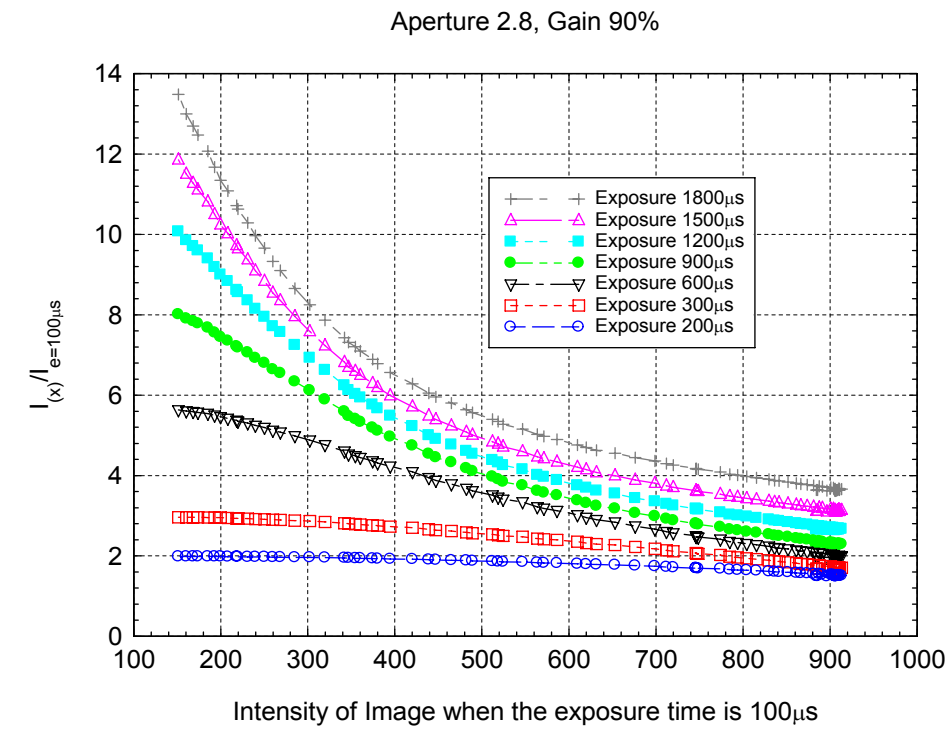

Figure D-4. The intensity ratio curves (exposure time effect)

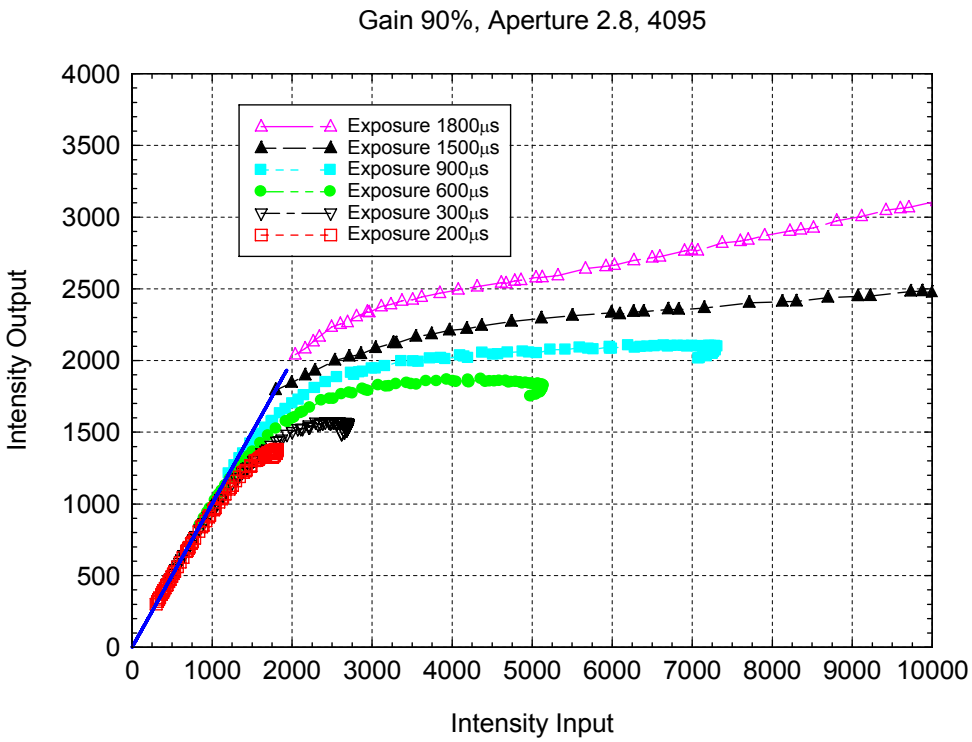

Figure D-5. Response of the Dicam-Pro Camera (exposure time effect)

D.1b. Gain level effect

During the experiment, the exposure time (400us) and aperture (f=2.8) were fixed. The Gain level changes from 60% us to 100%.The intensity ratio along the X-axisfor each case and response curves are given in Fig. D-6 and Figure D-7.

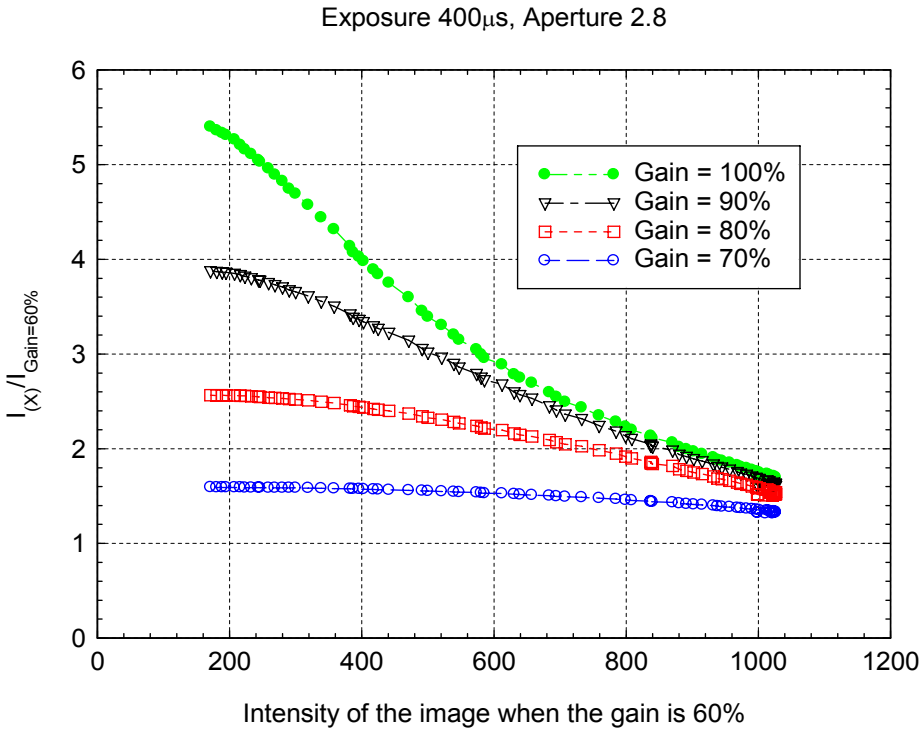

Figure D-6. The intensity ratio curves (Gain level effect)

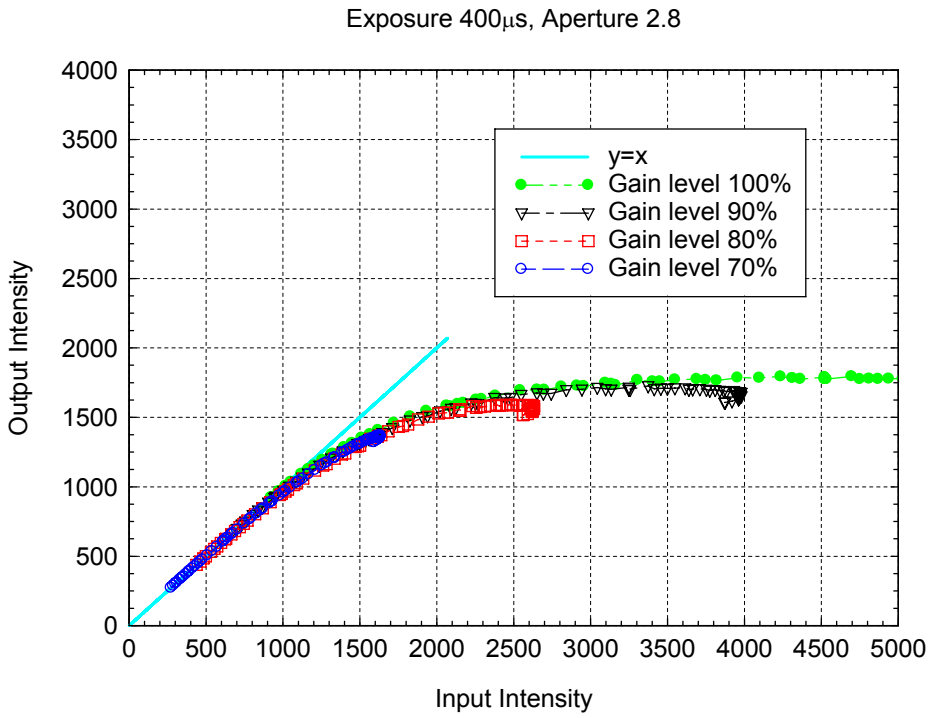

Figure D-7. Response of the Dicam-Pro Camera (Gain level effect)

D.1c. Aperture effect

During the experiment, the exposure time (500us) and Gain level (gain level =90%) were fixed. The aperture changes from 16 us to 4.The intensity ratio along the X-axisfor each case and response curves are given in Fig. D-8 and Figure D-9.

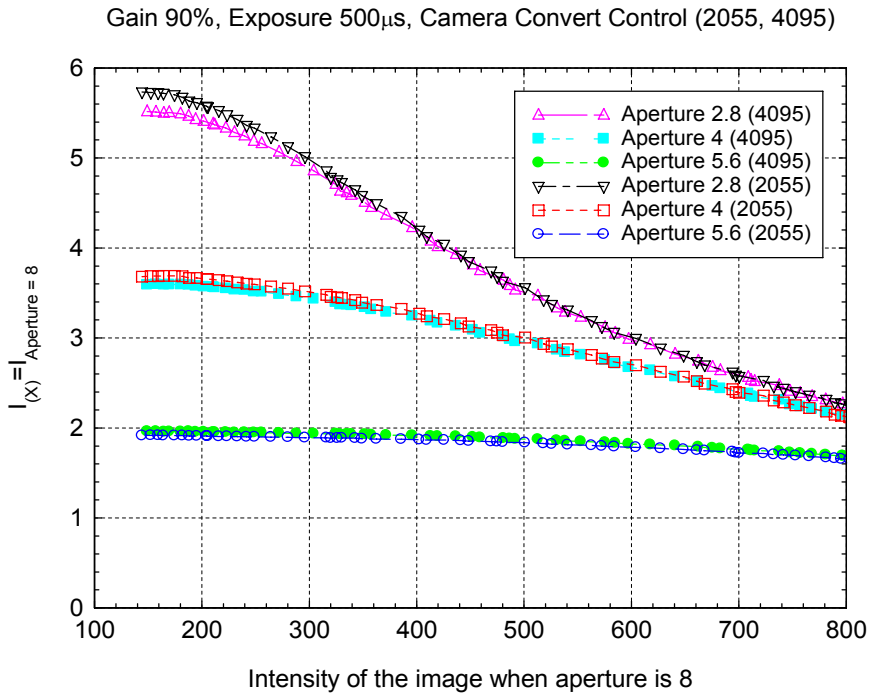

Figure D-8. The intensity ratio curves (aperture effect)

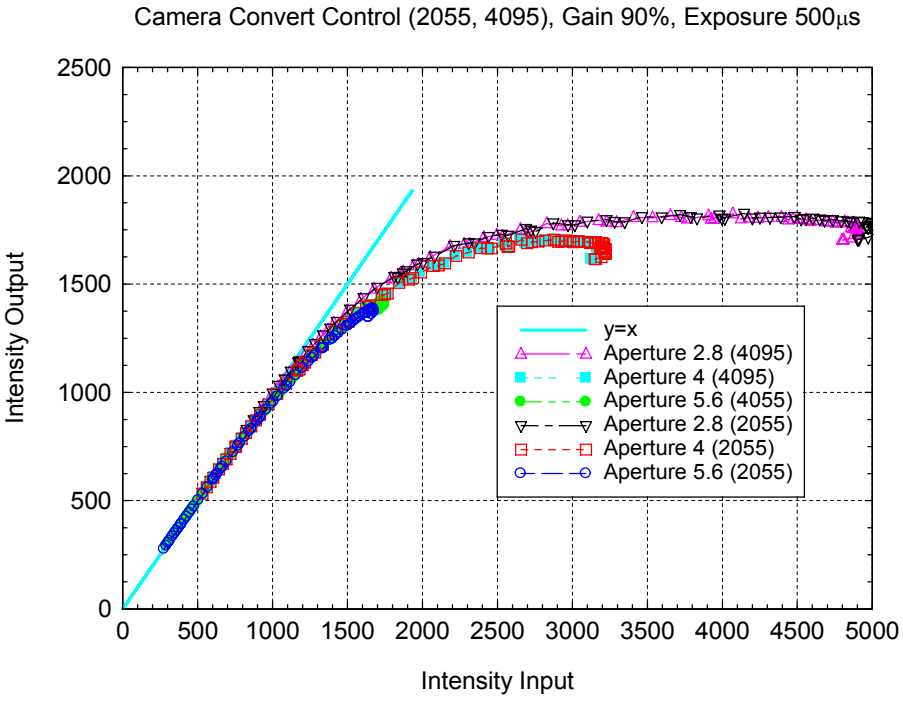

Figure D-9. Response of the Dicam-Pro Camera (aperture effect)

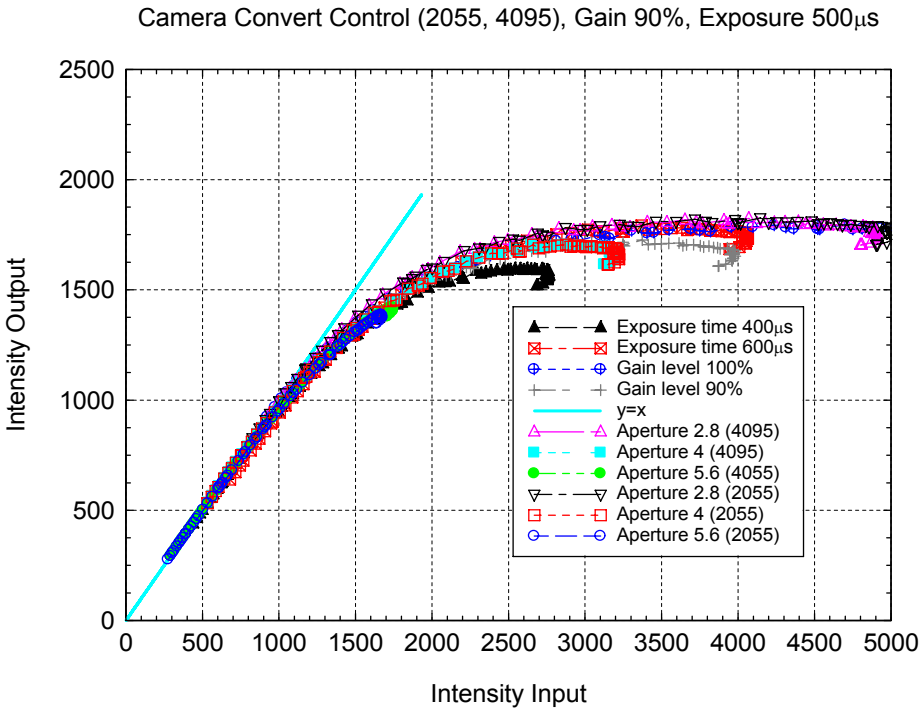

Figure D-10. Response of the Dicam-Pro Camera

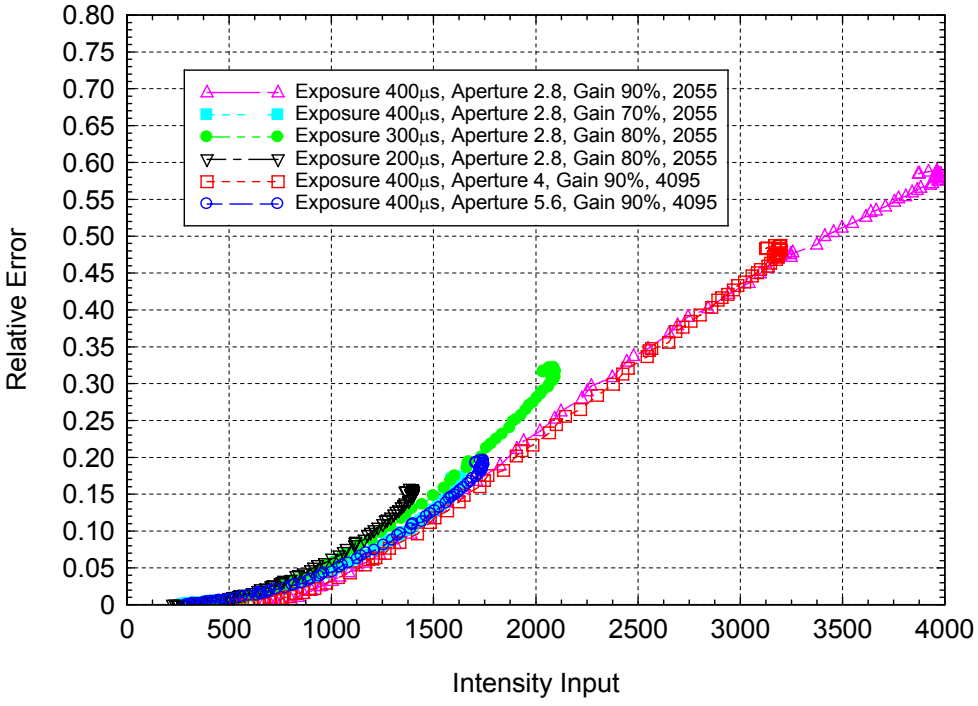

Figure D-11. Response of the Dicam-Pro Camera

D.2. Double shot mode

When the Dicam Pro camera works in double shot mode, there two kind of things need to be considered: one is the “afterglow” (Ghost image) and the other is fast gain charge capacity. Since the Dicam Pro used p46 phosphor, the “ghost image” intensity will be less than 1% when the time delay between the two shot is bigger than 2us. In the present test, the time delay between the two shot is or the order of ms, therefore, the effect of “ghost image” intensity is negligible.

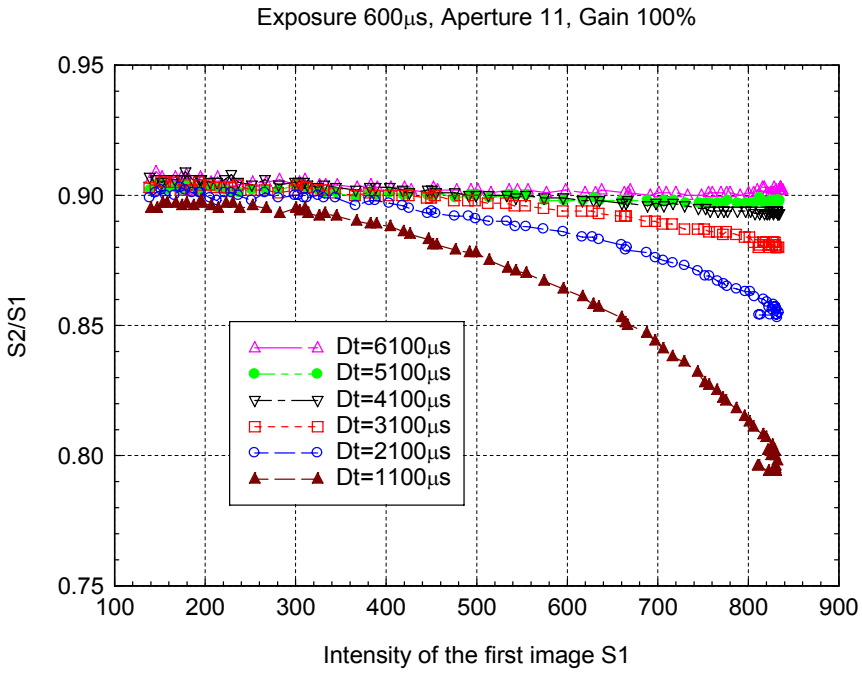

Figure D-12. Performance Dicam-Pro Camera at double shot mode.

REFERENCE

[1] J.P. Kutter, Current developments in electrophoretic and chromatographic separation methods on microfabricated devices. *Trac-Trends in Analyt. Chem.* Vol.19, (2000), pp. 352–363.

[2] J. Yang, C.W. Li and M.S. Yang, Lab-on-a-chip (microfluidics) technology. *Acta Bioch. Biop. Sin.* Vol. 34, (2002), pp.117–123.

[3] E. Verpoorte, Microfluidic chips for clinical and forensic analysis. *Electrophoresis,* Vol. 23, (2002), pp. 677–712.

[4] H. Cui, H. Keisuke, P. Dutta and C.F. Ivory, Isoelectric focusing in a poly(dimethylsiloxane) microfluidic chip. *Analytical Chemistr,* Vol. 77 , (2005), pp.1303–1309.

[5] Nguyan, N.T. and Wu, Z., Micromixers – a review, *Journal of Micromechnics and Microengineering*. Vol. 15, (2005), pp. r1-r16.

[6] Mao, H., Yang, T. and Cremer, P. S. A microfluidic device with a linear temperature gradient for parallel and combinatorial measurements, *J. Am. Chem. Soc.* Vol. 124, (2002), pp.4432–4435.

[7] Deshmukh, A. A., Liepmann, D. and Pisano, A. P., Characterization of a micro-mixing, pumping, and valving system, *Proc. Transducers'01, 11th Int. Conf. on Solid-State Sensors and Actuators* (Munich, Germany), (2001), pp.779–782.

[8] Glasgow, I. and Aubry, N. Enhancement of microfluidic mixing using time pulsing. *Lab on a Chip*, Vol. 3, (2003), pp. 114–20.

[9] El Moctar, A. O., Aubry, N. and Batton, J., Electro–hydrodynamic micro-fluidic mixer, *Lab on a Chip*, Vol. 3, (2003), pp. 273–280

[10] Deval, J., Tabeling, P. and Ho, C. M., A dielectrophoretic chaotic mixer, *Proc. MEMS'02, 15th IEEE Int. Workshop Micro Electromechanical System* (Las Vegas, Nevada), (2000), pp. 36–39.

[11] Bau, H. H., Zhong, J. and Yi, M., A minute magneto hydrodynamic (MHD) mixer*, Sensors Actuators B*, Vol.79, (2001), pp.207–15.

[12] Liu, R. H., Yang, J., Pindera, M., Z., Athavale M., and Grodzinski, P., Bubble-induced acoustic micromixing, *Lab on a Chip,* Vol. 2, (2002), pp.151–157.

[13] Chen, C. H. and Santiago, J. G., Electrokinetic flowinstability in high concentration gradient microflows", *Proc.2002 Int. Mech. Eng. Cong. and Exp.* (New Orleans LA) vol. 1, (2002), paper no 33563.

[14] Chen, C. H., Lin, H., Lele, S.K. and Santiago, J.G., Convective and absolute electrokinetic instability with conductivity gradients, *J. Fluid Mech*. Vol.524, (2005), pp.263-303.

[15] Hoberg, J. F., and Melcher, J. R., Internal electrohydrodynamic instability and mixing of fluids with orthogonal field and conductivity gradients", *J. Fluid. Mech.* Vol. 73, (1976), pp.333-351.

[16] Baygents, J. C. and Baldessari, F., Electrohydrodynamic instability in a thin fluid layer with an electrical conductivity gradient. *Phys. Fluids,* Vol. 10, (1998), pp. 301–311.

[17] Oddy, M. H., Santiago, J. G. and Mikkelsen, J. C., Electrokinetic instability micromixing", *Anal. Chem.*, Vol. 73, (2001), pp. 5822-5832.

[18] Posner, J. D., and Santiago, J. D., Convective instability of electrokinetic flows in a cross-shaped microchannel, *J. Fluid Mech.*, Vol. 555, (2006), pp.1-42.

[19] Shin, S.M., Kang, I.S. and Cho, Y.K., Mixing enhancement by using electrokinetic instability under time-periodic electric field, *J. Micromech. Microeng*. Vol 15, (2005), pp.445-462.

[20] Park, Jaewan, Shin, S.M., Kang I.S. and Cho, Y.K., Application of electrokinetic instability for enhanced mixing in various micro–T-channel geometries, *Physics of Fluids*. Vol. 17, (2005), 118101.

[21] Huang, Min-Zhong, Yang, Ruey-Jen ,Tai, Chang-Hsien, Tsai, Chien-Hsiung, Fu, Lung-Ming, Application of electrokinetic instability flow for enhanced micromixing in cross-shaped microchannel, Biomed Microdevices., Vol. 8, (2006), pp.309-315.

[22] Tai, Chang-Hsien , Yang, Ruey-Jen, Huang, Min-Zhong, Liu, Chia-Wei, Tsai, Chien-Hsiung, Fu, Lung-Ming, Micromixer utilizing electrokinetic instability-induced shedding effect,

Electrophoresis. Vol. 27, (2006), pp. 4982-4990.

[23] Jing J *et al,* Automated high resolution optical mapping using arrayed, fluid-fixed DNA molecules *Proc. Natl Acad. Sci. USA* 95, (1998), pp.8046–8051.

[24] Abramchuk S S, Khokhlov A R, Iwataki T, Oana H and Yoshikawa K, Direct observation of DNA molecules in a convection flow of a drying droplet, *Europhys. Lett.* Vol. 55, (2001), pp. 294–300.

[25] Uno K, Hayashi K, Hayashi T, Ito K and Kitano H, Particle adsorption in evaporating droplets of polymer latex dispersions on hydrophilic and hydrophobic surfaces *Colloid Polym. Sci.* Vol. 276, (1998), pp.810–815.

[26] Erbil H Y, McHale G, Rowan S M and Newton M I, Analysis of evaporating droplets using ellipsoidal cap geometry *J. Adhes. Sci. Technol.* Vol. 13, (1999), pp.1375–1391.

[27] Erbil H Y, McHale G and Newton M I, Drop evaporation on solid surfaces: constant contact angle mode, *Langmuir,* Vol. 18, (2002), pp.2636–2641.

[28] Rowan S M, McHale G, Newton M I and Toorneman M Evaporation of microdroplets of three alcohols *J. Phys. Chem.* B, Vol. 101, (1997), pp.1265–1267.

[29] McHale G, Rowan S M, Newton M I and Banerjee M K, Evaporation and the wetting of a low-energy solid surface *J. Phys. Chem.* B, Vol. 102, (1998), pp. 1964–1967.

[30] Ball J C, Marken F, Fulian Q, Wadhawan J D, Blythe A N, Schr¨oder U, Compton R G, Bull S D and Davies S G, Voltammetry of electroactive oil droplets: Part II. comparison of experimental and simulation data for coupled ion and electron insertion processes and evidence for microscale convection, *Electroanalysis,* Vol. 12, (2000), pp.1017–1025.

[31] Bard A J and Faulkner L R, 2001, *Electrochemical Methods* 2nd edn (New York: Wiley)

[32] Chung S K and Trinh E H, Containerless protein crystal growth in rotating levitated drops *J. Cryst. Growth,* Vol. 194, (1998), pp.384–397.

[33] Zhang N and Yang W J, Natural convection in evaporating minute drops *J. Heat Transfer*

Vol. 104, (1982), pp.656–662.

[34] Savino R and Monti R, Buoyancy and surface-tensiondriven convection in hanging-drop protein crystallizer, *J. Cryst. Growth,* Vol. 165, (1996), pp.308–318.

[35] K. H. Kang, S. J. Lee, C. M. Lee, 5th International Symposium on Particle Image Velocimetry, Busan, Korea, September 22-24, 2003.

[36] Kwan Hyoung Kang, Sang Joon Lee, Choung Mook Lee and In Seok Kang, Quantitative visualization of flow inside an evaporating droplet using the ray tracing method, *Measurement Science and Technology*, Vol. 15, (2004), pp.1104–1112.

[37] Prostein, R. F.., Physicochemical Hydrodynamics: A Introduction, John Wiely & Sons, Inc, New York, (1993), pp.190-203.

[38] Cummings, E. B.., Griffiths, S. K., Nilson, R. H., Irrotationality of Uniform Electroosmosis, Proc. *SPIE Microfluidics devices and system II*, (1999), pp.180-189.

[39] Cynthia Stowell and Brian A. Korgel, Self-Assembled Honeycomb Networks of Gold Nanocrystals, *Nano Letters*, Vol. 1, (2001), pp.595-600.

[40] R. Savino, D. Paterna and N. Favaloro, Buoyancy and Marangoni Effects in an Evaporating Drop, *Journal of thermophysics and heat transfer*, Vol. 16, (2002), pp.562-574.

[41] W.D.Ristenpart, P.G.Kim, C. Domingues, J.Wan, and H.A.Stone, Influence of Substrate Conductivity on Circulation Reversal in Evaporating Drops, *Physical Review Letters*, Vol. 99, (2007), pp.234502.

[42] Pfahler J; Harley J; Bau H, Liquid transport in micron and submicron channels. *Sensors and Actuators*, Vol. 21, (1990), pp.431– 434.

[43] Harley JC; Huang YF; Bau HH; Zemel JN, Gas flow in microchannels, *J Fluid Mech*, Vol. 284, (1995), pp.257–274.

[44] Tjerkstra RW; de Boer M; Berenschot E; Gardeniers JGE; van den Berg A; Elwenspoek MC, Etching technology for chromatography microchannels, *Electrochimica Acta,* Vol. 42, (1997),

pp.3399–3406.

[45] Harrison DJ; Fluri K; Seiler K; Fan Z; Effenhauser CS; Manz A, Micromachining a miniaturized capillary electrophoresis- based chemical analysis system on a chip. *Science* Vol. 261, (1993), pp. 895–896.

[46] Rocklin R D, Ramsey R S and Ramsey J M, A microfabricated fluidic device for performing two-dimensional liquid-phase separations. *Analytical Chemistry*, Vol. 72, (2000), pp. 5244–5249.

[47] Byung-Ho J; Linda MVL; Kathleen MM; David JBThree-dimensional microchannel fabrication in PDMS elastomer. *J MEMS,* Vol. 9, (2000), pp.76–102.

[48] Spring KR, Davidson MW. Introduction to Fluorescence Microscopy. *Nikon MicroscopyU*.

[49] Xia, Y., and Whitesides, G. M, Soft Lithography, *Angew. Chem. Int. Ed.*, Vol. 37, (1998), pp.550-575.

[50] Schrum, K. F., Lancaster, J. M., Johnston, S. E. and Gilman, S. D., Monitoring electroosmotic flow by periodic photobleaching of a dilute, neutral fluorophore. *Analyt. Chem.* Vol. 72, (2000), pp.4317–4321.

[51] Inoue, S. and Spring, K., *Video Microscopy: The Fundamentals* . Plenum (1997).

[52] Johnson T. J., Ross D., and Locascio, L. E., Rapid microfluidic mixing, *Anal. Chem.* Vol. 74, No. 45 (2002), pp.45-51.

[53] Bryden, M. D. and Brenner, E., "Effect of laminar chaos on reaction and dispersion in eccentric annular flow", *J. Fluid Mech.* Vol. 325, (1996), pp.219–237.

[54] Manuel G. Velarde and Radyadour Kh. Zeytounian, Interfacial Phenomena and the Marangoni Effect, *Spring Wien New York,* (2002), pp.11-15.

[55] Raffel, M., Willert, C., and Kompenhans, J., *Particle Image Velocimetry; A Practical Guide*, Springer – Verlag, (1998), 3rd edition.

[56] Adrian, R. J., Particle – imaging techniques for experimental fluid mechanics, *Annu. Rev. Fluid Mech*., Vol. 23, (1991), pp. 261-304.

[57] K. Uno, K. Hayashi, T. Hayashi, K. Ito and H. Kitano, Hayashi, Particle adsorption in evaporating droplets of polymer latex dispersions on hydrophilic and hydrophobic surfaces, *Colloid Polym Science,* Vol. 276, (1998), pp.810-815.

[58] Pringsheim, P., 1949, *Fluorescence and Phosphorescence* (New York: Interscience).

[59] Lu, Q. and Melton, A., "Measurement of transient tempeture field within a falling droplet", AIAA Journal, Vol.38, (2000), pp.95-101.

[60] Lavielle, P., Lemoine, F., Lavergne, G. and Lebouche, M., "Evaporating and combusting droplet temperature measurements using two-color laser-induced fluorescence," *Exp. Fluids*, Vol. 31, No. 1, (2001), pp.45-55.

[61] Coppeta, J. and Rogers, C., "Dual emission laser induced fluorescence for direct planar scalar behavior measurements", *Exp. Fluids*, Vol. 25, No. 1, (1998), pp.1-15.

[62] Sakakibara, J. and Adrian, R. J. , "Whole field measurement of temperature in water using two-color laser induced fluorescence," *Exp. Fluids*, Vol. 26. No. 1, (1999), pp.7-15.

[63] Escobar, S., Gonzalez, J. E. and Rivera, L. A., "Laser-induced fluorescence temperature sensor for in-flight droplet", *Exp. Heat Transfer*, Vol.14, (2001), pp.119-134.

[64] Wolff, M., Delconte, A., Schmidt, F., Gucher P. and Lemoine, F., "High-pressure diesel spray temperature measurements using two-color laser induced fluorescence", *Meas. Sci. Technol*., Vol.18, (2007), pp.697-706.

[65] Omrane, A., Juhlin, G., Ossler, F. and Alden, M., "Temperature measurements of single droplets by use of laser-induced phosphorescence", *Applied Optics*, Vol. 43, (2004), pp.3523-3529.

[66] Omrane, A., Santesson, S., Alden M. and Nilsson, S., "Laser techniques in acoustically levitated micro droplets", *Lab-on-a-Chip*, Vol. 4, (2004), pp.287-291.

[67] Hu, H., Koochesfahani, M., A novel technique for quantitative temperature mapping inliquid

by measuring lifetime of laser induced phosphorescence, *Journal of Visualization*, 6(2), (2003), pp. 143-153.

[68] Ponce, A., Wong, P. A., Way, J. J. and Nocera, D. G.,"Intense phosphorescence trigged by alcohol upon formation of a cyclodextrin ternary complex," *J. Phys. Chem.*, Vol. 97, (1993), pp.11137-11142.

[69] Hartmann, W. K., Gray, M. H. B., Ponce, A. and Nocera, D. G., "Substrate induced phosphorescence from cyclodextrin-lumophore host-guest complex," *Inorg. Chim. Acta*., Vol. 243, (1996), pp. 239-248.

[70] Gendrich, C. P. and Koochesfahani, M. M., "A spatial correlation technique for estimating velocity fields using Molecular Tagging Velocimetry (MTV)", *Exp. Fluids*, Vol. 22, No. 1, (1996), pp. 67-77.

[71] Koochesfahani, M. M. and Nocera, D. G., "Molecular Tagging Velocimetry," Handbook of Experimental Fluid Dynamics, Chapter 5.4, editors: J. Foss, C. Tropea and A. Yarin, *Springer-Verlag,* 2007.

ACKNOWLEGEMENTS

This work would not have been possible without the help and support of many people. I would like to thank my advisor Dr. Hui Hu first for his guidance, patience, and encouragement throughout this research. His preeminent ability to predict the upcoming results and thorough understanding of fluid dynamics helped me overcome lots of obstacles during this study.

I would also like to thank my thesis committee members for their efforts and contributions to this work: Dr. Michael G. Olsen, Dr. R. Ganesh Rajagopalan, Dr. Partha P. Sarkar, and Dr. Zhijian Wang.

I would like to specially thank Dr. Maosheng Ren (for sending his Ph.D. thesis to me from Europe), Dr. Deguang Yan (for suggestions on how to make high-frequency power switch), Dr. Kwan Hyoung Kang (for comments on analysis of droplet PIV data), Mr. Lucas A. Clemons (for checking the grammar errors in this thesis), Dr. Abdulilah Dawoud (for instructions on producing PDMS-Glass hybrid microchannels), Dr. Gary Tuttle and Dr. Dan Stieler (for their discussions on manufacturing glass microchannels), Ms. Li Li and Ms. Wenjun Xie (for their constant help on answering my questions regarding the usage of chemicals), and Mr. De Huang (for discussions on temperature measurement of droplets).

I would also like to thank Mr. Thomas J. Elliott, Mr. Bill Rickard, and Mr. Kevin Brownfield for their help on building experimental setups during this study.